

13 Physical Properties of Multiwall Nanotubes

Laszlo Forró,¹ Christian Schönenberger²

¹ Department of Physics
I.G.A. Ecole Polytechnique de Lausanne
CH-1015 Lausanne, Switzerland

² Department of Physics and Astronomy
CH-4056 Basel, Switzerland

Abstract. After a short presentation on the preparation and structural properties of multiwall carbon nanotubes (MWNTs), their outstanding electronic, magnetic, mechanical and field emitting properties are reviewed. The manifestation of mesoscopic transport properties in MWNT is illustrated through the Aharonov–Bohm effect, universal conductance fluctuations, the weak localization effect and its power-law temperature/field dependences. Measurements of the Young’s modulus of individual nanotubes show the high strength of tubes having well-graphitized walls. Electron spin resonance (ESR) measurements indicate the low-dimensional character of the electronic states even for relatively large diameter tubes. The conducting nature of the tubes, together with their large curvature tip structure, make them excellent electron and light emitters suitable for applications.

1 Introduction

With the discovery of multiwall carbon nanotubes (MWNTs) by Iijima in 1991, a new era has started in the physics and chemistry of carbon nanostructures [1]. After the synthesis of single wall carbon nanotubes (SWNTs) in 1993 by Bethune and coworkers [2] and by Iijima et al. [3], the main stream of carbon research shifted towards the SWNTs, especially through the development of an efficient synthesis method for their large scale production by Smalley and colleagues [4]. Nevertheless, multiwall carbon nanotubes present several complementary attractive features with respect to SWNTs, both for basic science and for applications. For example, one advantage of MWNTs is that they can be grown without magnetic catalytic particles, which are certainly disturbing for magnetic, and probably for transport measurements, as well. The larger diameter of the MWNTs enables us to study quantum interference phenomena, such as the Aharonov–Bohm effect, in magnetic fields accessible in the laboratory, while study of the same phenomenon would require 600 T fields in the case of SWNTs. The Russian-doll structure allows better mechanical stability and higher rigidity for the MWNTs which is needed for scanning probe tip applications. Even for making nanotube composites, for which the first step is the chemical functionalization of the tube walls, the multiwall configuration is more advantageous, since efficient load transfer can be achieved without damaging the stiffness of the internal tubes.

The chapter is organized as follows. First we will briefly review the production methods for MWNTs. Since the control of sample quality is a condition *sine qua non* for all studies, we present the purification and the structural characterization of the nanotubes. Different methods for filling the hollow interior of the nanotubes with a variety of elements is described. The longest section of the chapter is devoted to the transport properties of MWNTs, since these properties are really spectacular, and most of the mesoscopic transport phenomena can be studied on this system. The magnetic properties are investigated with the electron spin resonance (ESR) technique and the fingerprints of low-dimensionality are investigated. The field emission properties of MWNTs, which allowed the first application of these structures in flat panel displays, are studied for individual nanotubes. Light emission follows the discussion on electron emission. This phenomenon is presented not only in the field emission configuration, but also by using an STM tip for electron injection. The mechanical properties of MWNTs (as compared to SWNT ropes) are also discussed. A review of the role of the defects, deformations, and mechanical manipulation of MWNTs is also presented.

2 Production methods and purification

Carbon nanotubes are produced in several different ways. One method relies on a carbon arc where a current on the order of 70 to 100 A passes through a

graphite rod (which serves as the anode) to a graphite cathode in a He atmosphere [1,5,6]. In the arc process, a rod-shaped deposit forms on the cathode as shown in Fig. 1. This deposit has a hard grayish outer shell, which houses a soft deep black material. This material consists of fine fibers (typically 1 mm in length and a fraction of a mm in diameter), which under high resolution transmission electron microscopy (HRTEM) are revealed to be dense bundles of MWNTs [6]. Production rates are reasonably high: several hundred mg of raw material is produced in about 10 min. The material is quite heterogeneous and consists of MWNTs with a rather large dispersion in their outer and inner diameters. The MWNTs are typically 10 nm in diameter and are on the order of 1 m long. The tubes tend to be very straight (when not stressed, of course). Besides MWNTs, this method also produces rather large amounts of graphitic material in the form of multilayered fullerenes (or carbon onions) and amorphous carbon which covers the nanotubes. Purification steps are often employed [7,8] with varying degrees of success.

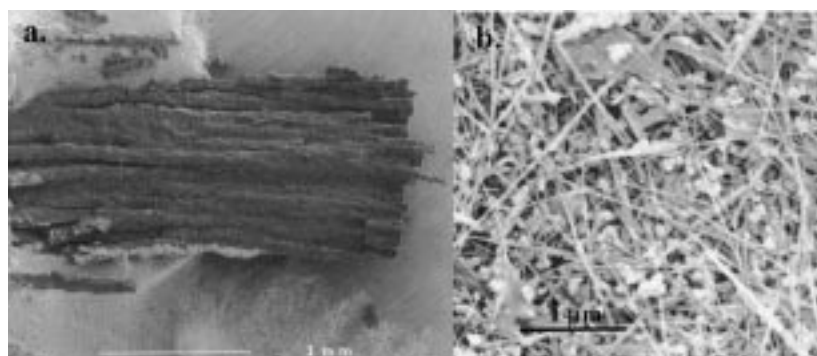


Fig. 1. Scanning Electron Microscope image of the (a) rod-shaped deposit on the cathode and of (b) a zoomed part of a deposit, which shows the heterogeneous character of the as-grown nanotube soot [8]

For the sake of completeness, we mention that a variation of this synthesis method can be used to produce SWNTs (with diameters of the order of 1 nm), by replacing the graphite anode with a hollow graphite tube which is filled with graphite powder containing powdered transition metal (i.e., Fe, Co, Ni,) and/or rare earth metal (Y, Lu, Gd) catalysts, and other metals as well (i.e., Li, B, Si, Sn, Te, Pb,...) [2,12]. This method was originally discovered by Bethune and co-workers [2] and by Iijima and co-workers [3]. A method which holds much promise was subsequently introduced by Smalley and coworkers [4], and involves the laser ablation in a He atmosphere of a graphite target which is impregnated with a transition metal catalyst. The material which is produced by this process is very rich in long bundles of SWNTs. Subsequent purification steps allow this material to be refined (through the elimination

of other graphitic particles) to “bucky paper”, which is a dense mat of purified SWNTs, and this bucky paper is used for many physical properties measurements.

Other, less exotic, nanotube production methods are based on the thermal decomposition of hydrocarbons in the presence of a catalyst (for a review, see Fonseca et al. [13]). These methods [14] are most closely related to traditional carbon fiber production schemes, which have been known for a long time [15,16]. There have been several adaptations to nanotube production, involving a hydrocarbon (i.e., acetylene, methane) and very small catalyst particles (i.e., Co, Cu, Fe) supported on a substrate (silica, zeolite) [17–19]. At elevated temperatures, the hydrocarbon decomposes on the catalyst, whereby long nanotubes are spun from the particle (Fig. 2). These methods produce an impressive variety of nanotubes [20], many of which are regularly coiled, forming long helices [21]. This helix-forming feature indicates the presence of defects (non-hexagonal units) in the graphitic structure [22]. The method is relatively simple to apply and produces nanotubes in large quantities. Thus, vapor phase growth is of interest, since large quantities of nanotubes are necessary for many applications, such as making composite materials.

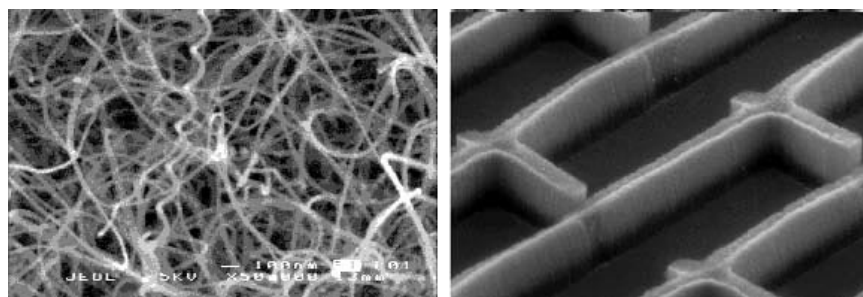


Fig. 2. On the left, a scanning electron (SEM) micrograph of MWNTs prepared by catalytic decomposition of acetylene, and, on the right, an ordered array of nanotubes deposited on pre-designed lithographic structures [23]

A further advantage of the gas phase growth method is that it enables the deposition of carbon nanotubes on pre-designed lithographic structures [23], producing ordered arrays, a dense forests of aligned nanotube films on surfaces (Fig. 2) which can be used in applications such as thin-screen technology, electron guns, etc.

No matter which type of carbon nanotubes we are dealing with, the first step in the study of carbon nanotubes is technological: their purification. Purification steps, that are commonly performed, may consist of controlled oxidation, chemical treatment, filtration and other procedures, each with their advantages and disadvantages. The very first purification method consisted

of burning the raw soot in air. Since the non-nanotube graphitic structures are less resistive to oxidation, they will burn first. This method resulted in a relatively pure nanotube soot, but nevertheless with damaged tube walls and tips, and resulted in losing about 99 wt% of the material [24]. It is possible to save a much larger percentage of tubes by using surfactants and then successive filtrations [25]. A liquid-phase separation of nanotubes and nanoparticles was performed by filtering a kinetically stable colloidal dispersion consisting of the carbon material in a water/surfactant solution, thus allowing extraction of the nanotubes from the suspension, while leaving the nanoparticles in the filtrate. Further purification was accomplished by size-selection through controlled flocculation of the dispersion. Final separation yields as high as 90% in weight were obtained without any damage to the tube tips or tube walls following the flocculation separation process. The result of this separation is seen in Fig. 3. An interesting side-product of this purification method is a large quantity of polyhedral, onion-like carbon particles, which are interesting nanostructures in their own right.

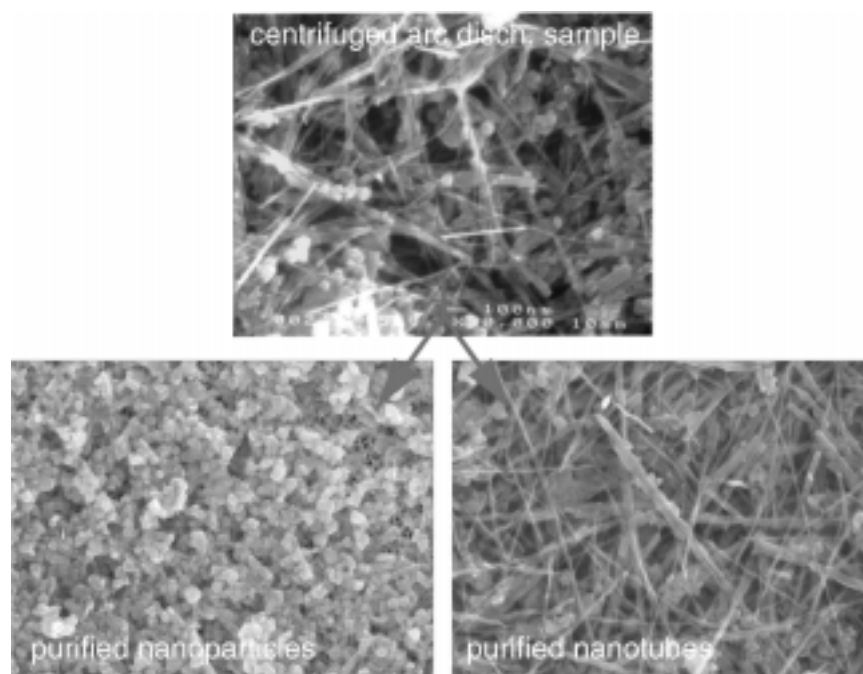


Fig. 3. Scanning electron (SEM) micrographs of a MWNT deposit (top) and MWNTs after purification (bottom right) and as a 'side-product' of onion-like carbon nanoparticles (bottom left) [7,8]

3 Crystallographic Structure

3.1 Crystallographic structure as seen by HRTEM

For fundamental studies and for some applications, one is looking for “perfect” nanotube structures, which means well-graphitized nanotube walls, with a level of defects as low as possible. High resolution transmission electron microscopy (HRTEM) provides valuable information about the nanotube quality prepared by different synthesis methods. The MWNTs grown by the arc discharge method have generally the best structures, presumably due to the high temperature of the synthesis process. It is likely that during the growth process, most of the defects are annealed. In the HRTEM image these rolled-up graphene sheets appear as straight lines (see Fig. 4). Each nested graphite cylinder has a diameter which is given by two integers m and n , the coefficients of the lattice vectors \mathbf{a}_1 and \mathbf{a}_2 in the chiral vector $C_h = n\mathbf{a}_1 + m\mathbf{a}_2$ which describes the way the graphene sheet is rolled-up, and relates to the helicity of the nanotube [26,27], and is described elsewhere in this volume [28,29]. The diameter d_t of the (n, m) nanotube is given by

$$d_t = a(m^2 + mn + n^2)^{1/2} / \pi. \quad (1)$$

The interlayer spacing in MWNTs (0.34 nm) is close to that of turbostratic graphite [16,30]. Since nanotubes are composed of nearly coaxial cylindrical layers, each with different helicities, the adjacent layers are generally non-commensurate, i.e., the stacking cannot be classified as AA or AB as in graphite [16,30]. The consequence of this interplanar stacking disorder is a decreased electronic coupling between the layers relative to graphite. MWNTs also have structural features which are different from the well-ordered graphitic side-walls: the tip, the internal closures, and the internal tips within the central part of the tube, called the “bamboo” structures (Fig. 4). The structure of the tips is closely related to that of the icosahedral fullerenes [31], where the curvature is mediated by introducing pentagons (and higher polygons) into the structure, while maintaining essentially the sp^2 electronic structure (i.e., 3 bonds) at each carbon atom site. A variety of tip structures are commonly observed [32], and an usual feature is that the tubules within the MWNT often close in pairs at their tips. The tips play an especially important role in the electronic and field emission properties of nanotubes. There has been considerable debate concerning the structure of MWNTs, i.e., whether in fact the tubules close on themselves or if nanotubes sometimes are scrolled [21] (i.e., whether one or more of the sheets of graphite that are rolled have two edges). This interpretation followed analysis of HRTEM and electron diffraction studies of nanotubes which revealed that the number of different chiral angles which are observed in a MWNT are usually less than the number of tubules. Anomalous layer spacings are also observed (at least for catalytically grown tubes). This would be the case if one

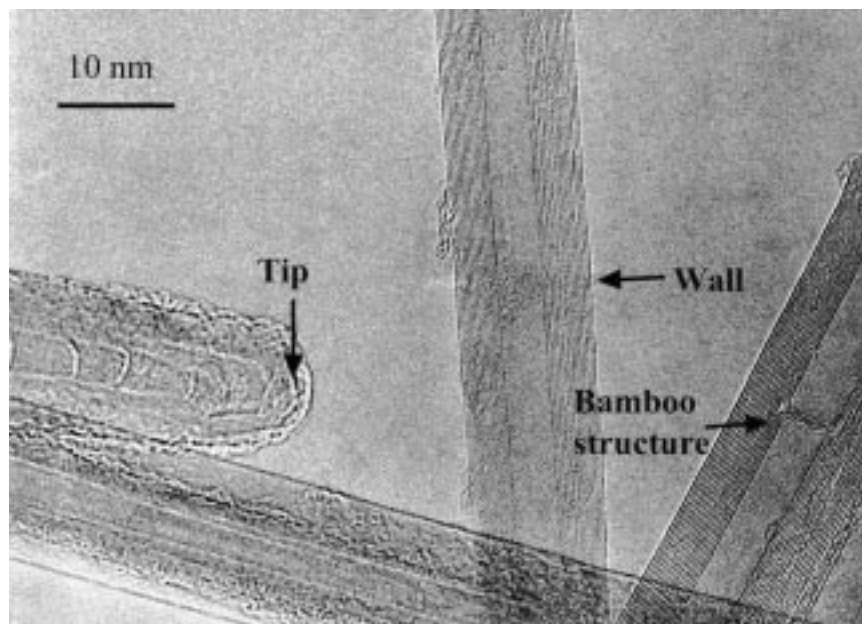


Fig. 4. HRTEM images of MWNTs grown by the arc-discharge method, showing the well graphitized wall, the tip and the “bamboo” structure [9–11]

sheet produced several cylindrical layers in the tube. However, the consensus viewpoint from many HRTEM studies appears to favor the Russian doll model, since there has been little evidence for the edges which should result from graphene scrolls. However, nanotubes morphologies may vary considerably with the production method. This is especially true for catalytically grown nanotubes. If the growth conditions are not adjusted properly, then poorly graphitized walls result, and tubes with so-called coffee-cup structures form (see Fig. 5).

There can be other types of defects which are more difficult to visualize like point defects in planar graphite, consisting of vacant sites (Schottky defects) and displacements of atoms to interstitial positions (Frenkel defects). These are quite costly in energy due to the strength of the broken bonds, but these defects can be introduced by high energy electron irradiation [33]. Ultrasonic treatment may also produce defects in MWNTs [34] and SWNTs [35], which become more susceptible to chemical attack after being subjected to high intensity ultrasound treatment. Defective structures also result after severe chemical attack (i.e., in hot nitric acid and oxidation at elevated temperature) which has the effect of destroying the tips and hence provides a method to open the tubes.

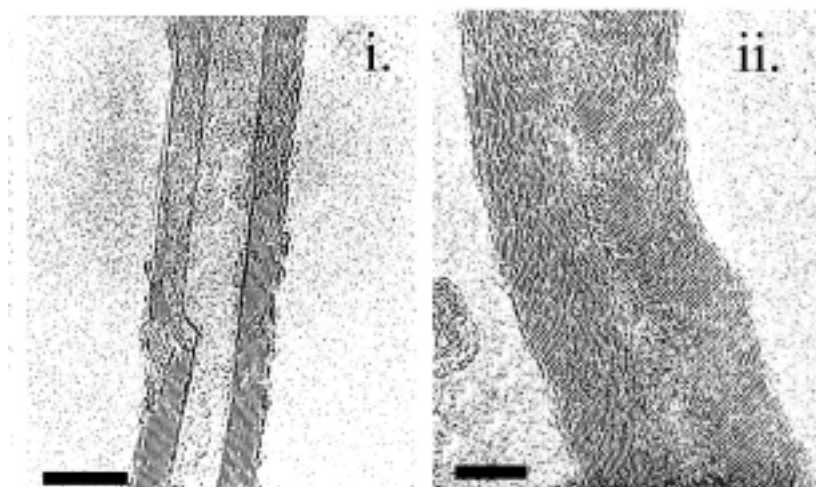


Fig. 5. HRTEM images of MWNTs produced by the decomposition of acetylene using a Co/silica catalyst, (i) at 720°C and (ii) at 900°C. All scale bars are 10 nm [7]

3.2 Filling of carbon nanotubes

The hollow interior of carbon nanotubes naturally presents us with an opportunity to fill the nanotube core with atoms, molecules, or metallic wires, thereby forming nanocomposites with new electronic or magnetic properties. In early approaches, electrodes composed of carbon impregnated with the filling material were used [36,37]. This resulted in a large variety of filled graphitic structures, metallic carbides, but with relatively low yield. Loiseau and collaborators [38] realized that a minute quantity of sulfur present in the graphite/metal mixture helps to wet the surface of the cavity, so that the tubes fill up over micron distances with a high yield [20]. Nanowires of various elements (or their sulfides) were formed by this method, including transition metals (Cr, Ni, Co, Fe), rare earth metals (Gd, Sm, Dy) and covalent elements (Ge, Se, Sb). Figure 6 displays a nanotube with a crystalline wire of Ge inside the core [38,20].

Other approaches to filling the hollow core involved the exploitation of nanotube capillarity [39]. This procedure for filling nanotubes may involve a chemical method, using wet chemistry [40]; or (b) a physical method, where capillarity forces induce the filling by a molten material [41–43]. In the wet-chemistry method, the nanotubes are refluxed in a nitric acid bath in order to open their tips. When a metal salt is simultaneously used in the bath, it is possible to obtain oxide or pure metal particles by a subsequent annealing process. Also, the metal/salt solvent bath can also be used on previously opened tubes. However, the drawback of this method is that it requires chem-

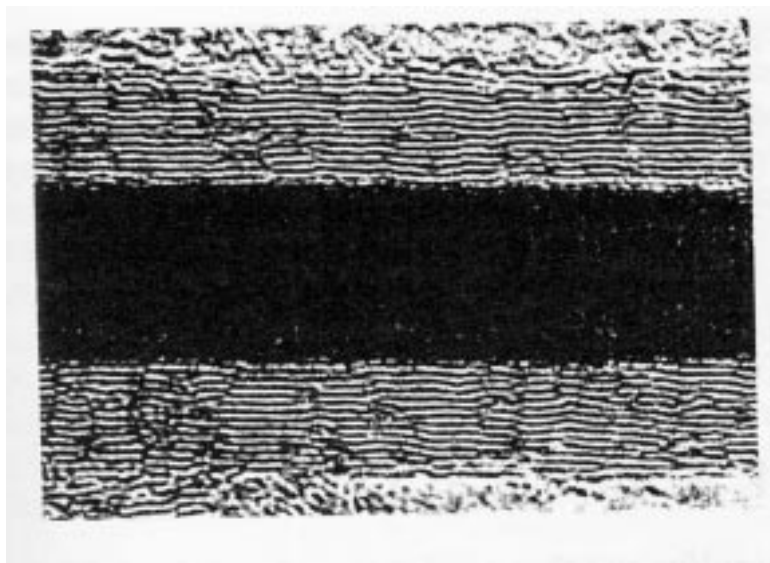


Fig. 6. HRTEM image of a MWNT filled with crystalline Ge. Waiting for Loiseau [38,20]

ical manipulation over a long time to open nanotubes containing various tip structures, “bamboo” closures and various numbers of SWNT constituent layers. Furthermore, the reduction of the metal salts inside the tubes does not give a continuous wire, but rather yields metallic blobs. This can be observed in Fig. 7 in the case of a nanotube filled with silver [43].

In the physical method, the nanotubes are filled by first opening them, for example, by heating them in air to oxidize the nanotube tips preferentially, and the opened tubes are then submerged in molten material [41–43]. Studies of filling nanotubes with liquid metals have shown that only certain metals will enter the nanotubes and that the metal surface tension is the determining factor [37,43]. Further studies along these lines have demonstrated that the capillary action is related to the diameter of the inner cavity of the nanotube. This was explained in terms of the polarizability of the cavity wall, which is related to the radius of curvature, through the pyramidalization angle (bond-bending angle) and the polarizability of the filling material [43]. The filled nanotubes with different metals offer exciting structures for future electronic studies. In the following sections, we focus on a review of electrical and magnetic measurements that have been performed on arc-discharge grown MWNTs, which show good structural order and their purity is well controlled.

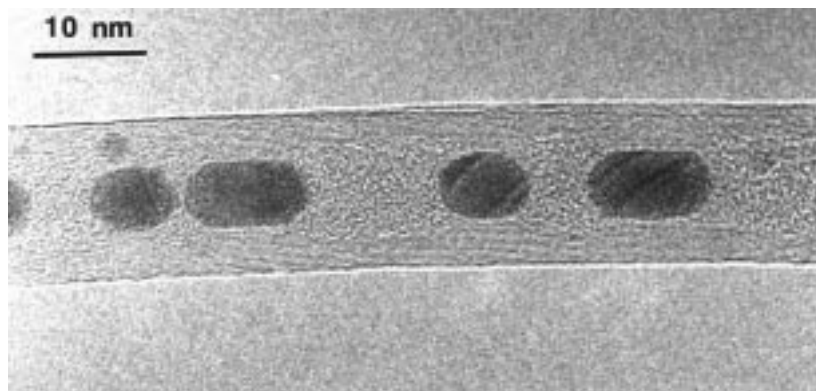


Fig. 7. HRTEM of a carbon nanotube whose inner cavity is filled with silver particles (lattice fringes correspond to [111] planes of Ag, with a lattice spacing of 0.23 nm). The tube cavity is first filled with molten silver nitrate that is subsequently reduced to metal by electron irradiation, *in situ*, in the electron microscope [43]

4 Electronic Properties of Multiwall Carbon Nanotubes

The electronic and electrical properties of low-dimensional conductors are an exciting area of research. Very rich phase diagrams have been predicted. Since a small set of 1-D modes is sufficient to describe the low-energy electronic properties of carbon nanotubes, they are considered prototype 1-D molecular conductors. This is particularly true for single-wall nanotubes (SWNTs). Many interactions are especially strong in 1-D. The Coulomb interaction, for example, cannot efficiently be screened, leading to a strongly correlated electron gas, called a Luttinger liquid, whose low-energy excitations are long-range density waves. In Luttinger liquids a pseudo-gap develops for the conventional quasi-particles. Because multi-wall nanotubes (MWNTs) consist of several coaxially arranged SWNTs, one may expect that MWNTs do not qualify as 1-D conductors. However, there is now convincing evidence that Luttinger-liquid-like features are present in MWNTs too [44]. Moreover, the electric current introduced into a MWNT from the outside is confined to a large extent to the outermost SWNT [45,46]. In this respect, studying MWNTs is somewhat similar to studying transport in large diameter SWNTs. This is interesting because SWNTs of diameters similar to the outer diameter of a typical MWNT (20 nm) have not yet been observed. Large diameter nanotubes have specific advantages: they favor low-ohmic contact and allow investigation of quantum-interference phenomena in a magnetic field, such as the Aharonov–Bohm effect. This is not possible in SWNTs, because a huge magnetic field of order 1000 T would then be required. This section focuses on the electrical and electronic properties of MWNTs with an emphasis on

electrical measurements. Though quite a variety of experimental results are available today, very fundamental questions remain unanswered, partly because of conflicting results. For example, at present we do not know with certainty the electronic ground state of carbon nanotubes. Do quasi-particles in the sense of Fermi liquid theory exist or is the ground state a correlated many-body state (charge-density wave)? May it be possible that superconducting or ferromagnetic fluctuations are present, and affect the ground state? To what extent are carbon nanotubes (SWNTs and MWNTs) ballistic quantum wires? Because it is impossible to discuss all available data in depth, we focus on a few representative measurements by which the present picture of the electronic properties of MWNTs can be illustrated. The selections made by the authors is biased by their own research. The presentation is therefore neither complete, nor balanced.

This section is structured as follows. Section 4.1, written in a form accessible to any scientist with a basic background in condensed matter physics, provides additional introductory material to help the reader understand the chapter, and more detailed reviews can be found in Refs. [47,48]. Section 4.2 briefly reviews recent work regarding electrical transport in MWNTs (see also Ref. [44]). This section has been added for those interested in entering this field of research. Next, we mention in Sect. 4.3 important results regarding transport in films, assemblies and ropes of MWNTs. We emphasize the measured positive Hall coefficient and briefly mention recent results on the thermopower. Most of the text is concerned with measurements on single MWNTs (Sect. 4.4). This section is further divided into parts on: 1) electrical transport in zero magnetic field (temperature and gate-dependence of the resistance), 2) magnetotransport (magnetic-field-dependence), and finally, 3) spectroscopy, highlighting density-of-state features in carbon nanotubes. The chapter ends in Sect. 4.9 with a discussion of the most pressing issues.

4.1 Multiwall Nanotubes in Relation to Graphene Sheets

A multi-wall carbon nanotube (MWNT) is composed of a set of coaxially arranged single-wall carbon nanotubes (SWNTs) of different radii [1]. The distance between nearest-neighbor shells corresponds, within a good approximation, to the van-der-Waals distance between adjacent carbon sheets in graphite (3.4 Å) [16]. The outer diameter of MWNTs depends on the growth process. It is typically of order 20 nm for arc-discharge grown tubes, but can attain values exceeding 100 nm for some CVD-grown MWNTs. (The term nanofiber is reserved for multiwall nanotubes in the diameter range 10–100 nm [16].) Transmission electron microscopy has shown that these large diameter tubes contain a considerable amount of defects (see Fig. 5), though examples of MWNTs with lower defect densities have been demonstrated [16]. Carbon shells are often not continuous throughout the tube. For this reason, we will focus only on electrical measurements obtained from arc-discharge grown MWNTs which have been demonstrated to be highly graphitized [7,9].

Nanotubes are a special class of fullerene molecules, namely those that are quantum wires with 1 -dimensional (1-D) translation symmetry. SWNTs are the simplest of these objects. A SWNT can be constructed from a slice of graphene (a single planar sheet of the honeycomb lattice of graphite) rolled into a seamless cylinder, i.e., with all carbon atoms covalently bound to three neighbor carbons. A large number of such foldings are possible. In fact, each graphene lattice vector (called a wrapping or chiral vector) defines a unique nanotube [47]. Regarding electronic properties, SWNTs can be further classified as being either semiconductors or metals [49–51]. If all wrapping vectors would be realized with equal probability, 1/3 of the SWNTs would be metallic and 2/3 semiconducting. Assuming that neighboring shells do not interact, the electronic properties of MWNTs would be similar to a set of independent SWNTs with radii in the range of a few nanometers to ≈ 10 nm. Though the coupling strength between adjacent shells might be low, it possibly cannot be neglected altogether [52]. For this reason, a much richer band structure might be expected. Graphite is, in fact, an excellent example for demonstrating the importance of the weak inter-plane coupling for ground-state properties. Graphite is a semimetal, and the finite density-of-states (DOS) at the Fermi energy can be traced back to the three-dimensional crystal structure with finite interplanar coupling which leads to a small band overlap of 40 meV [16,47]. MWNTs are interesting because they allow us to study the transition from the SWNT single molecule to the behavior of the macroscopic crystal (graphite). MWNTs are mesoscopic, in-between the single-wall nanotube molecules and planar graphite. In this respect, MWNTs play the same role as carbon onions play to fullerene research [16,29,53]. An immediate question arises now: are the electronic properties of MWNTs closer to graphite or do MWNTs rather behave as a set of independent SWNTs? In order to be able to discuss the electrical measurements of MWNTs, it is useful to briefly highlight the important electronic properties of the two reference systems: graphite and ideal SWNTs.

Starting with graphite, we will first review the band structure of a single layer of graphite, called a graphene sheet. The carbon atoms in a graphene sheet form a planar hexagonal lattice, the honeycomb lattice. Each carbon atom is covalently bound to three neighbor carbons by sp^2 molecular orbitals. The fourth valence electron, an atomic p_z state, hybridizes with all other p_z orbitals to form a delocalized π -band. It is important to recognize that the unit-cell of graphene contains two carbon atoms. Hence, the π -band has to accommodate two electrons per unit cell. In the case of an even number of valence electrons, a material can in general be either a metal or a semiconductor. The system that is realized depends on the specific form of the overlap integral. Figure 8 shows the result of a simple tight binding calculation [54]. It is seen that the bonding π -band is always energetically below the antibonding π^* band for all wavevectors, except at the corner points of the Brillouin zone boundary (the K points), where the band splitting is zero

by the symmetry of the honeycomb lattice [47]. With regard to band overlap, graphene is very unusual. Theoretically, all bonding states will be filled up to the corner points, which coincide with the Fermi energy E_F . Since the density-of-states (DOS) is zero at E_F , graphene is not a true metal. However, it also not a true semiconductor, because there is no excitation gap at the K points. Graphene can thus be characterized as a zero-gap semiconductor or as a zero-DOS metal.

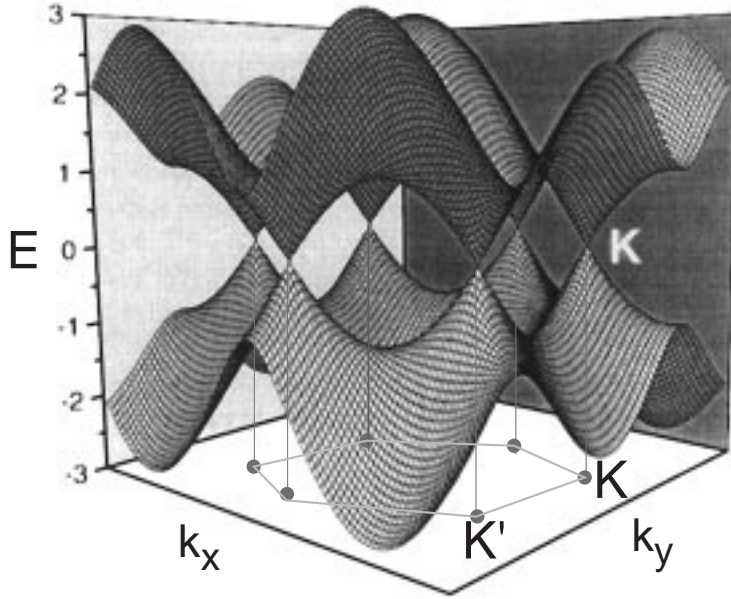


Fig. 8. Tight-binding dispersion relations of the π - (lower half) and π^* (upper half) bands of graphene. The energy is expressed in units of the nearest-neighbor C-C overlap integral $\gamma_0 \simeq 3.0$ eV and measured relative to the Fermi energy E_F for neutral (undoped) graphene [55]

The insight into the band structure of graphene allows us to calculate the Drude resistivity. In the vicinity of E_F , the electron states can be approximated by $E = \pm \hbar v_F |\mathbf{k}|$, where \mathbf{k} is the 2-D-wavevector measured with respect to the two independent Brillouin corner points [56]. Energies are measured relative to the charge neutrality level, and the Fermi velocity is taken to be $v_F = 10^6$ m/s [54,57–59]. For the electron density-of-states (DOS), we obtain $n_{2D}(E) = 2E/\pi(\hbar v_F)^2$. Using the Einstein equation $\sigma_{2D} = e^2 n_{2D} D$, which relates the conductivity σ_{2D} to the diffusion coefficient $D = v_F l_e / 2$ and the

electron density, we obtain for the energy-dependent conductivity $\sigma_{2D}(E)$

$$\sigma_{2D}(E) = \left(\frac{2e^2}{h} \right) \frac{E}{\hbar v_F} l_e, \quad (2)$$

where l_e is the carrier scattering length. In order to be able to calculate the equilibrium sheet conductivity σ_{2D} at a finite temperature (T), the exact position of the Fermi level needs to be known. Without any doping, $E_F = 0$. For a real graphene surface a finite doping is unavoidable due to adsorbates causing partial charge transfer. In this more realistic situation, the Fermi level will be either below (hole doping) or above (electron doping) the neutrality point. Two cases have to be distinguished: the high- and low-temperature limits, defined by $kT \gg |E_F|$ and $kT \ll |E_F|$, respectively. For the latter (either strongly doped, or sufficient low temperature) σ_{2D} is given by Eq. 2 with E replaced by $|E_F|$. Note, that the mean-free path is in general T -dependent, due to electron-phonon scattering, for example, thus l_e increases with decreasing T and approaches a finite zero-temperature value, only determined by static disorder. The equation therefore predicts true metallic behavior for the temperature-dependent resistance, i.e., the electric resistance should decrease with decreasing temperature due to the gradual suppression of electron-phonon scattering. In the high-temperature limit ($kT \gg |E_F|$, i.e., low doping or ideal graphene) σ_{2D} is given (up to a numerical factor of order 1) by Eq. 2 with E replaced by kT . That $\sigma_{2D} \propto T$ reflects the fact that the carrier density is proportional to T . Also this equation predicts a metallic temperature-dependence of the resistance provided that $l_e \propto T^{-p}$ with $p \geq 1$. This condition is always met, except for highly disordered samples for which l_e is a constant over a substantial temperature range. The resistance of such ‘dirty’ samples should display a $R(T) \propto T^{-1}$ dependence. Unfortunately, there are no measurements for the electric sheet resistance of graphene, since graphene is a theoretical object. In contrast, there is an extensive source of literature for graphite (including graphitic fibers and turbostratic graphite) [15,16]. Graphite consists of a regular A-B-A-B stacking of graphene planes. There is a weak interplane coupling of order $\Delta \sim 10$ meV, which results in semimetallic behavior and a band overlap of 40 meV. Most importantly, graphite develops a finite DOS at E_F and is therefore a metal. The sheet conductivity is approximately given by Eq. 2 with E replaced by Δ (if $kT \ll \Delta$). We therefore expect a metallic temperature-dependent resistivity for crystalline graphite in the temperature range $kT \ll \Delta$. Figure 9 shows the measured temperature-dependence of the electric resistivity $\rho(T)$ for different forms of carbon fibers [15]. The upper curves correspond to disordered pregraphitic carbons while the ones with lower ρ correspond to highly graphitized samples. Because we will be discussing arc-discharge grown MWNTs in this chapter, arc-grown graphitic fibers (graphite whiskers [16,60]) provide a good reference material. Both arc-grown and single crystalline graphite display a metallic $\rho(T)$, i.e., the resistivity decreases with decreasing temperature T . From the typical value of $5 \times 10^{-6} \Omega\text{m}$ (100 K) for the resistivity, a

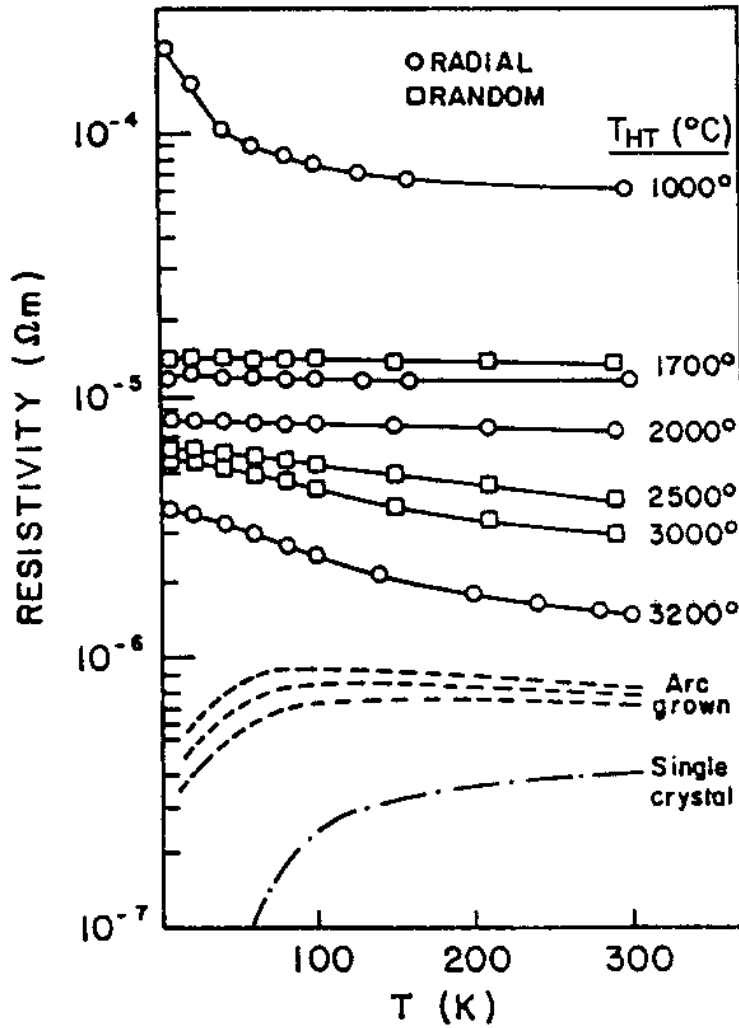


Fig. 9. Electrical resistivity ρ as a function of temperature T for different form of graphitic fibers taken from Ref. [15]. The higher up the curves, the larger the disorder. The curve with the lowest resistivity corresponds to crystalline graphite.

sheet resistance R_{\square} of $R_{\square} = 1.5 \text{ k}\Omega$ is deduced. Taking Eq. 2 with E replaced by $\Delta \sim 10 \text{ meV}$, we obtain a scattering length of $l_e = 600 \text{ nm}$. Because the zero-temperature resistivity of single-crystalline graphite can be more than an order of magnitude lower, large mean-free paths for scattering $l_e > 1 \mu\text{m}$ are possible. Based on this consideration we can expect that carbon nanotubes may be 1-D ballistic conductors, provided that nanotubes of structural quality similar to single-crystalline graphite can be obtained. For the uppermost

curve in Fig. 9, corresponding to highly disordered carbon fibers, the mean-free path is only of order 1.5 nm. In such disordered materials the graphene planes have a high density of structural defects as well as random stacking (turbostratic graphite) [16], and the interplane coupling is reduced to $\Delta \approx 0$. The properties of disordered carbon fibers are therefore very well approximated by a set of independent sheets of ‘dirty’ graphene. For the comparison with MWNTs we should memorize the following two observations: 1) disordered graphite is characterized by a resistance upturn at low temperatures (localized behavior) with a typical sheet resistance of $R_{\square} \approx 100 \text{ k}\Omega$, and 2) crystalline graphite is characterized by a metallic $R(T)$ with $R_{\square} \approx 1 \text{ k}\Omega$ [61].

Next, we will briefly discuss the electronic properties of the other reference compound, that is of a perfect single-wall carbon nanotube. A SWNT is obtained from a slice of graphene wrapped into a seamless cylinder. The periodic boundary condition around the nanotube circumference causes quantization of the transverse wavevector component. Let us denote the wavevector along the tube direction by k and the transverse component by k_{\perp} . The allowed k_{\perp} are spaced by $2/d_t$, where d_t is the tube diameter. The 1-D band structure can now easily be constructed using for example the 2-D tight-binding band structure $E(k_x, k_y)$ of graphene, shown in Fig. 8. Each k_{\perp} within the first Brillouin zone gives rise to a 1-D subband (1-D dispersion relation) by expressing E as a function of k for the given k_{\perp} . Hence, a set of subbands $E_{k_{\perp}}(k)$ is obtained. A large diameter tube will have many such subbands, while a small diameter tube has only a few. It turns out that both metallic and semiconducting nanotubes are possible. A nanotube is metallic if and only if the K points belong to the set of allowed k -vectors. In the $\mathbf{k} \cdot \mathbf{p}$ scheme, the eigenfunctions in the vicinity of the K points are approximated by a product of one of two fast oscillating graphene wavefunctions $\Psi_K(\mathbf{r})$, changing sign on the scale of interatomic distances, and a slowly varying envelope function $F(\mathbf{r})$ [58]. The periodic boundary condition leads to the following condition for Ψ_K [62]:

$$\Psi_K(\mathbf{r} + \mathbf{L}) = \Psi_K(\mathbf{r}) \exp(i2\pi\nu/3), \quad (3)$$

where \mathbf{L} measures the length around the tube circumference and $\nu = 0, \pm 1$, depending on the wrapping or chiral vector [55]. Taking for the slowly varying function F a plane wave (free electrons) and noting that F should cancel the phase factor in Eq. 3, we obtain the condition

$$k_{\perp} = \frac{2}{d_t} (n - \nu/3) \quad n = 0, \pm 1, \pm 2, \dots \quad (4)$$

for the allowed transverse wavevectors. The approximate 1-D dispersion relations, valid in the vicinity of E_F , can now be derived using $E(\mathbf{k}) = \pm \hbar v_F |\mathbf{k}|$. Explicitly:

$$E_n(k) = \pm E_0 \sqrt{(n - \nu/3)^2 + (kd_t/\pi)^2} \quad (5)$$

with $E_0 = 2\hbar v_F/d_t$. These approximate dispersion relations are shown in Fig. 10. As can be seen, there are metallic ($\nu = 0$) and semiconducting ($\nu =$

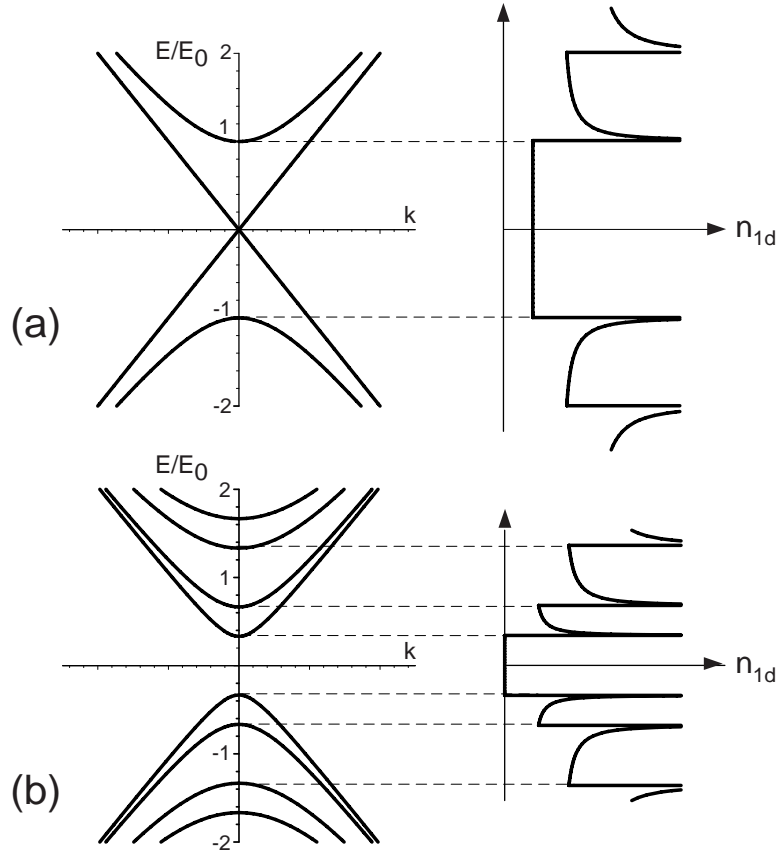


Fig. 10. Approximate dispersion relations (left) for the 1-dimensional electronic energy bands and the corresponding density-of-state (right) of metallic (a), and semiconducting (b), single-wall carbon nanotubes close to the Fermi energy. The energy scale is in units of $E_0 = 2\hbar v_F/d_t$

± 1) nanotubes. The bandgap of a semiconducting tube is $E_g(d_t) = 2E_0/3$, which is inversely proportional to the tube diameter. We obtain 0.68 eV for a tube with $d = 1.3$ nm. Since MWNTs have rather larger diameters of order 20 nm, the corresponding bandgaps are only $E_g \approx 44$ meV. We mention, that the set of 1-D subbands in Fig. 10 needs to be duplicated because the K and K' points which are equivalent in the absence of a magnetic field are both in the first Brillouin zone [47,55]. Furthermore, the crossing at the Fermi energy between the bonding and antibonding states need not necessarily be at $k = 0$ [47]. The Fermi level crossing for zig-zag $(n, 0)$ tubes, which can be metallic

or semiconducting, is at $k = 0$. In contrast, the level crossings are found at $k = \pm 2\pi/(3a_0)$ for armchair (n, n) tubes. Armchair tubes are always metallic. For all metallic nanotubes, the Fermi energy intersects two 1-D branches with positive velocity (right-movers) and two with negative velocity (left-movers) [47]. This corresponds to two 1-D modes (not counting spin) leading to a quantized conductance of $G = 4e^2/h$ for an ideal nanotube. Figure 10 also shows the corresponding density-of-states (DOS), which are characterized by sharp features (van Hove singularities) at the onset of subbands. The observations of these singularities in, for example, tunneling spectroscopy, is a direct proof for the presence of a 1-D band structure. This has indeed been observed in SWNTs using scanning-tunneling spectroscopy at low temperatures [63,64]. Since MWNTs consist of tubes with larger diameters (d_t), we need to understand how the van Hove singularities develop if d_t approaches values comparable to the mean-free path l_e . The picture sketched above is valid if $l_e \gg d_t$ (1-D-ballistic transport). In contrast, if $l_e \ll d_t$ transport is 2-D-diffusive and the density-of-states should closely resemble that for graphene without any singularities. If, on the other hand, l_e is of the same order as d_t , transport is neither fully 2-D-diffusive, nor 1-D-ballistic. In this regime, the characteristic subband features in the DOS are still present, albeit considerably broadened. One expects to see broadened peaks in the DOS with a mean level spacing of the 1-D subbands given by

$$\overline{\Delta E_{sb}} = E_0/2 = \frac{\hbar v_F}{d_t} \sim 33 \text{ meV} \quad (d_t = 20 \text{ nm}), \quad (6)$$

where $E_0 = 2\hbar v_F/d_t$.

For a metallic nanotube, two subbands are occupied at E_F . Consequently, the electric conductance G is predicted to be $G = 4e^2/h$, provided the complete wire is ballistic. We not only require $l_e \gg d_t$, but in addition ballistic transport requires that $l_e \gg L$, where L is the length of the electrically contacted nanotube segment. More precisely, ballistic transport requires that backscattering must be absent altogether, taking into account both the nanotube *together* with the electric contacts. This condition is very hard to satisfy in the laboratory [44]. Important for MWNTs is the question of how the band structure might change due to inter-tube coupling. This question has only recently been addressed [65–67]. However, the main consequence of the low-energy properties can simply be guessed. It is convenient to consider only two tubes which couple only weakly to each other. If one is semiconducting and the other is metallic, it is obvious that the low-energy properties are just determined by the metallic one, with no modifications in the DOS around zero energy. If the two tubes are metallic, the situation is expected to be more complicated. However, in practice it is most likely that the two tubes have different chiralities. For example, one tube could be of the armchair type and the other a zig-zag one, to mention an extreme case. Because the zero-energy bands cross at different k points for the two tubes, hybridization is very weak around E_F and the total DOS is just the sum of the two. Strong band

structure modifications are only expected for tubes of similar chiralities [66]. We should keep in mind, however, that this picture is not valid, if the tubes are relatively strongly doped such that E_F is shifted either into the valence or conduction bands. For a comparison of results obtained for SWNTs with MWNT studies, the following three aspects of SWNTs should be emphasized: 1) an *ideal* SWNT is either a metal or a semiconductor with a considerable band gap, 2) the band structure consists of a set of 1-D-subbands, leading to van Hove singularities in the density-of-states, and 3), the electrical conductance G is quantized in units of $4e^2/h$, provided that backscattering is absent altogether.

4.2 Electrical Transport in MWNTs: A Brief Review

A remarkable variety of physical phenomena have been observed in electrical transport. The first signature of quantum effects was found in the magnetoresistance (MR) of MWNTs. Song *et al.* studied bundles of MWNTs [68], while Langer *et al.* was able to measure the MR of a single MWNT for the first time [69]. In both cases a negative MR was observed at low temperatures indicative of weak localization [70–73]. From these MR experiments, the phase-coherence length l_ϕ was found to be small, amounting to < 20 nm at 0.3 K, in strong contrast with the ballistic transport theoretically expected for a perfect nanotube. However, evidence for much larger coherence lengths in SWNTs was provided by the observation of zero-dimensional states in single-electron tunneling experiments [74,75], and in other experiments discussed below.

Recently, a pronounced Aharonov–Bohm resistance oscillation has been observed in MWNTs [46]. This experiment has provided compelling evidence that l_ϕ can exceed the circumference of the tube, so that large coherence lengths are possible for MWNTs too (see also [76]). Since the magnetic-flux modulated resistance is in agreement with an Aharonov–Bohm flux of $h/2e$, this oscillatory effect is supposed to be caused by conventional weak-localization for which the backscattering of electrons is essential. In essence, as in the work of Langer *et al.* [69], 2-D-diffusive transport could explain the main observation reasonably well.

The Aharonov–Bohm experiment provides a convincing proof that the electric current flows in the outermost (metallic) graphene tube, at least at low temperatures $T < 70$ K. Presumably, this is a consequence of the way in which the nanotubes are contacted. In general, electrodes are evaporated over a MWNT, and the electrodes therefore contact the outermost tube preferentially. Since it is essentially only the outermost tube that carries the current, large diameter single graphene cylinders can now be investigated. Recently, proximity-induced superconductivity was found in weak links formed by a bundle of SWNTs in contact with two superconducting banks [77]. Furthermore, spin transport also has been considered. Here, a MWNT was contacted

by two bulk ferromagnets (e.g., Co) and the electrical resistance was measured as a function of the relative orientation of the bulk magnetization in the two ferromagnetic contacts [78]. A resistance change of order 10% was found, from which the authors estimate the spin-flip scattering length to be > 130 nm. All the striking results mentioned above were obtained by contacting a single nanotube with the aid of micro- and nano-structured technologies.

Alternative approaches for contacting nanotubes have been developed as well. For example, Dai *et al.* [79] and Thess *et al.* [80] have measured the voltage drop along nanotubes using movable tips, and Kasumov *et al.* have developed a pulsed-laser deposition method [81]. Furthermore, scanning-probe manipulation schemes were developed [82–84], and recently it has been shown that SWNTs can directly be synthesized to bridge pre-patterned structures [85]. Still another elegant method allowing one to contact a single MWNT electrically has been used by Frank *et al.* [45], whereby a single nanotube extending out of a MWNT fiber (a macro-bundle) is contacted by gently immersing the fiber into a liquid metal (e.g., mercury). Immersing and pulling out the nanotube repeatedly is claimed to have a cleaning effect. In particular, graphitic particles are removed from the tubes. After some repeated immersions, an almost universal conductance step behavior is observed, with steps close to the quantized value $G_0 = 2e^2/h$. From these experiments, the researchers conclude that transport in MWNTs is ballistic over distances on the order of > 1 μm . This is a very striking result because the experiments were conducted at room temperature. At present, it is not clear why the conductance is close to G_0 instead of the theoretically expected value of $2G_0$.

4.3 Hall-Effect and Thermopower in assembled Nanotubes

Already in 1994, Song *et al.* studied the electronic transport properties of macro-bundles of MWNTs with diameters tens of μm [68]. The authors measured the temperature-dependence of the resistance R , its change in magnetic field B and the Hall effect. Above 60 K, the magnetoresistance (MR) is positive, i.e., R increases with magnetic field; they however also found that a pronounced negative MR peak develops at low temperatures. This negative MR-dependence is suggestive of weak localization (WL). WL is an interference correction to the Drude resistance of a metal. WL primarily lowers the diffusion coefficient D due to constructive interference of mutually time-reversed quasiclassical electron trajectories in zero magnetic field. Because only trajectories of lengths shorter than the phase-coherence length l_ϕ can participate, sufficiently low temperatures are usually required. For $T < 10$ K, the conductivity σ was found to show a $\ln(T)$ dependence. This is in agreement with 2-D-WL theory, so that $l_\phi < d_t$, where d_t is the diameter of a typical MWNT within the bundle. This relatively short coherence length suggests a small mean-free path for scattering from static disorder, implying that the MWNTs are fairly disordered. This is further supported by the

temperature dependence of the measured conductance $G = R^{-1}$. This temperature dependence of the conductance, as well as of the Hall coefficient, are shown in Fig. 11, where G is shown to be proportional to T over a remark-

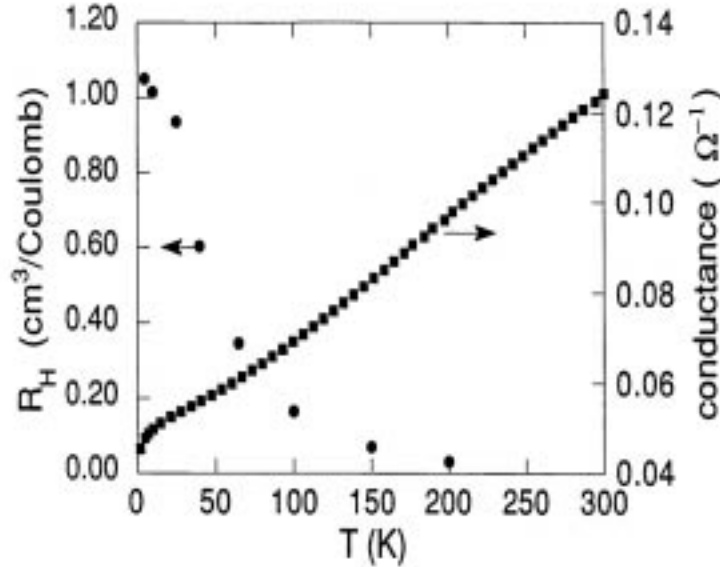


Fig. 11. The Hall coefficient R_H (left scale) and the conductance (right scale) vs temperature T taken from Song *et al.* [68]

ably large temperature range of 50 – 300 K. Below ≈ 50 K the T -dependence weakens to finally turn into a logarithmic dependence, characteristic of 2-D-WL. From the theoretical models, which have been developed for graphite in Sect. 4.1, a linear $G(T)$ is predicted for the conductance of disordered graphene. In this case, l_e is mostly determined by scattering from static disorder, and therefore l_e is only weakly T -dependent. This yields $G \propto T$ because of the energy dependent density-of-states (DOS) of graphene. The cross-over at 50 K suggests metallic behavior which can be either due to intertube coupling (like in graphite) or due to doping, thus shifting E_F away from the neutrality point. Because the change of the Hall coefficient R_H from ≈ 0 (high T) to a pronounced positive value (low T) coincides with the ‘flattening’ in $G(T)$, the nanotubes in Fig. 11 are most likely slightly (hole) doped. From the cross-over temperature (≈ 50 K), the Fermi energy is estimated to be ≈ -4 meV. Using the theoretical DOS for graphene, the sheet doping level is found to be $n_{2D} = 1.5 \times 10^9 \text{ cm}^{-2}$, which has to be compared to the bulk doping level of $n_{3D} = 6 \times 10^{18} \text{ cm}^{-3}$ obtained from R_H . If the material would be homogeneous and densely packed then $n_{2D} = n_{3D} d_{I_p}$, where $d_{I_p} = 3.4 \text{ \AA}$

is the interplane distance of graphite. Under these assumptions, we obtain $n_{2D} = 2 \times 10^{11} \text{ cm}^{-3}$ from R_H , which is more than two orders of magnitude larger than the previous estimate. Though appearing to be inconsistent, this disagreement can easily be resolved. The apparent inconsistency is caused by the assumption of complete filling. Moreover, we know today that most of the electric current in transport measurements is confined to the outermost metallic SWNT at low temperature [45,46]. Hence, the volume fraction cannot exceed $d_{I_p}/d_t \approx 50$, thus resolving this apparent inconsistency.

From fits of the low- T conductance to WL theory, Song et al. could give estimates for several important parameters. For example, they obtained $R_{\square} \approx 6 \text{ k}\Omega$ for the sheet resistance, $D \approx 50 \text{ cm}^2/\text{s}$ for the diffusion coefficient and $l_e \approx 5 \text{ nm}$ for the mean-free path. The main results of this work, a positive R_H suggesting hole doping and interference corrections at low T , have both been confirmed later by Baumgartner *et al.* with measurements on oriented MWNT films [86].

We have added the following discussion, to emphasize the question of doping in carbon nanotubes. This has recently received quite some attention, in particular, regarding research on SWNTs. The Hall coefficient clearly suggests hole doping (of unknown origin). Much more evidence for hole doping is emerging now from other work. The thermoelectric power S has been found to be positive and approximately linear in T at low T , both for SWNT and MWNT ropes [87–89]. The linear temperature dependence of the thermopower suggest metallic behavior. The substantial positive value of S of order $40 - 60 \mu\text{V}/\text{K}$ at 300 K initially posed a serious problem, since S should vanish, if E_F lies at the charge neutrality-point, as theoretically expected (for graphite $S \approx -4 \mu\text{V}/\text{K}$). However, these findings of a substantial positive S are in agreement with the above-mentioned positive Hall coefficient, suggesting unintentional hole doping. If we assume that E_F is considerably shifted into the valence band, then the large magnitude of S can easily be understood. Assuming, for simplicity, an energy-independent scattering length, but taking the DOS to be that of graphene, then S is interestingly exactly given by the standard textbook formula for free electrons, i.e., $S = -\pi^2 k^2 T / (3eE_F)$. From the measured value of S one derives -0.14 eV which amounts to a doping level of $n_{2D} = 5 \times 10^{10} \text{ cm}^{-2}$. This level may appear to be large, but if we express the doping in terms of the elementary charge (e) per unit tube-length, there is on average only one e per 300 nm (assuming a SWNT with $d = 2 \text{ nm}$). Most recently, it has been shown that the magnitude and even the sign of S can be changed by annealing the nanotubes in vacuum. It is believed that such a treatment removes oxygen, which may act as the dopant [90–92]. Nanotubes might be more sensitive to environmental conditions than initially believed. Clearly more work is needed to understand the nature of the doping and of the doping level.

4.4 Electrical Transport Measurement Techniques for Single MWNTs

Electric measurements on single multi-wall carbon nanotubes (MWNTs) have been performed in three ways: (1) metallic leads are attached to a single tube supported on a piece of Si wafer with the aid of microfabrication technology [46,69,81,93]; (2) the end of a macrobundle of MWNTs, fixed on an moveable manipulator, is steered above a beaker containing a liquid metal (e.g., mercury) and the MWNTs are then gently lowered into the liquid metal. According to this method, a single MWNT makes contact to the liquid metal first, enabling conductance measurements to be made on a single nanotube [45], as shown in Fig. 12, and (3) a scanning-tunneling microscope can be used to measure the local electronic density-of-states by measuring the bias-dependent differential conductance while the tip is positioned above a single MWNT.

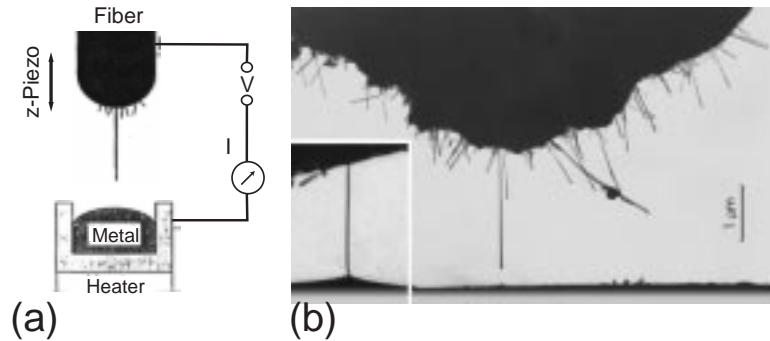


Fig. 12. (a) Schematic diagram of a contacting apparatus. The fiber is moved into the liquid metal, while the conductance G is measured. Taken from Frank *et al.* [45]. (b) Transmission electron micrograph of the end of a nanotube fiber with one single MWNT extending far out from the fiber [45]

Because lithography is now widely used for contacting nanotubes, we discuss the lithographic approach in detail in the following. A droplet of a dispersion of nanotubes (NTs) is used to spread the NTs onto a piece of thermally oxidized Si. Then, a PMMA resist layer is spun over the sample. An array of electrodes, each consisting of two or more contact fingers together with their bonding pads, is exposed by electron-beam lithography. After development, a metallic film (mostly Au) is evaporated over the structure and then lifted off. The sample is now inspected by either scanning-electron microscopy (SEM) or scanning-force microscopy (SFM) and the structures that have one single nanotube lying under the electrodes are selected for electric measurements. An example of a single MWNT contacted by four Au fingers is shown in Fig. 13. Since the success of this contacting scheme works by

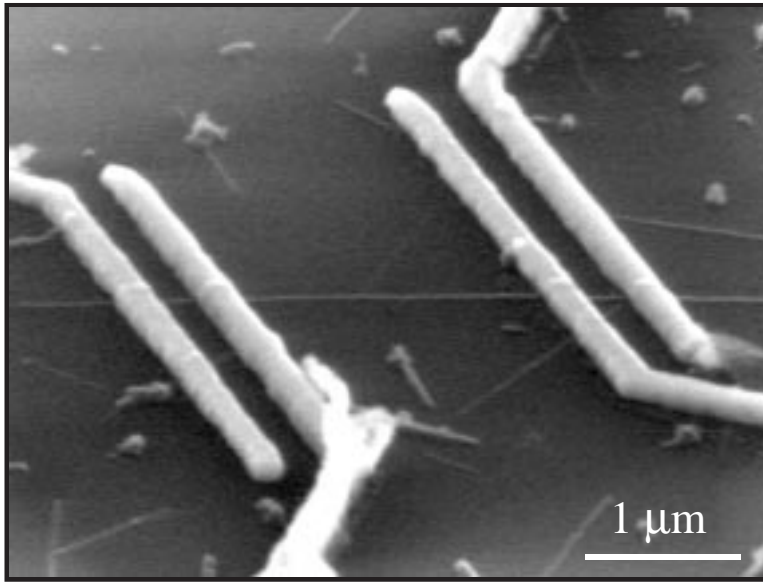


Fig. 13. Scanning-electron micrograph of a single multi-wall nanotube electrically contacted by four Au fingers from above. The separation between the inner two contacts is $2\ \mu\text{m}$ [94]

chance, it is obvious that the yield is low. There are many structures which have either no or several NTs (nanotubes) contacted in parallel. Since a large array of more than 100 structures can readily be fabricated, however, this scheme has turned out to be very convenient.

Alternatively, it is also possible to first structure a regular pattern of alignment marks on the substrate. After adsorbing the NTs, the sample is first imaged with SEM or SFM in order to locate suitable NTs. Having noted the coordinates of the designated nanotubes aided by the alignment marks, the electrodes can be structured directly onto the respective NTs with high precision. This improves the yield at the cost of an additional lithography step. Let us emphasize that the Au electrodes are evaporated directly onto the nanotubes. The reverse scheme is also possible. Here, electrode structures are made first and the NTs are adsorbed thereafter. In this scheme (nanotube over the contacts), the contact resistances are typically found to be large ($> 1\ \text{M}\Omega$). It was only with the aid of local electron exposure directly onto the NT-Au contacts that this resistance could be lowered to acceptable values [95]. In contrast, the contact resistance R_c can be surprisingly small in the former scheme (nanotube under the contacts). R_c is of order $0.1 \dots 20\ \text{k}\Omega$ with an average of $4\ \text{k}\Omega$ [44]. R_c has been determined by comparing the 2-terminal (R_{2t}) with the 4-terminal (R_{4t}) resistance according to $R_c = (R_{2t} - R_{4t})/2$.

An ‘ideal’ contact is defined to have no backscattering and to inject electrons in all modes equally. Electrons incident from the NT to a contact will then be adsorbed by the contact with unit probability. Because the contact couples to both right and left propagating modes equally, Ohm’s law should be valid in this limit. It is important to realize that for ideal contacts, R_{4t} cannot contain any nonlocal contributions, i.e., contributions to the resistance that arise from a NT segment not located in between the inner two contacts. Any sign of non-locality points to the presence of non-ideal contacts. Conceptually, it is very hard to image that the Au-electrodes provide an ideal contact to a metallic nanotube, because the electronic properties change abruptly from something which is more like a semimetal (well within the nanotube) to a high-carrier density metal well within the metal contact.

In order to confirm the ballistic 1-D nature of an ideal metallic nanotube in transport measurements, ideal contacts (no backscattering) are required. Only then, will the conductance be quantized and equal to $G = 4e^2/h$. [96]. Since the metallic electrodes are extended and it is very likely that the coupling from the metal to the tube is not uniform, metal-tube tunneling occurs at many different spots simultaneously. Unfortunately, models for such contacts are not yet available. The interpretation of the measured resistance would be much easier, if we were able to intentionally choose the strength of the coupling at the contacts. If this were possible, one could fabricate 4-terminal devices with low-ohmic contacts for the outer two contacts (placed as far apart as possible) and very weak-coupling (non-perturbing) contacts for the inner two. R_{4t} of such a device would then give the real intrinsic nanotube resistance caused by scattering in the tube. In particular, $R_{4t} = 0$ for the ballistic ideal metallic NT. Furthermore, a high-ohmic contact (a true tunneling contact) can be used for tunneling spectroscopy from which the density-of-states in the tube can be derived.

Until now, lithographically fabricated contacts are only accidentally high-ohmic. However, an elegant non-invasive measurement of the electrostatic potential is possible with scanning-probe microscopy in which a tip is used to probe the potential along a biased nanotube [97]. In addition to allowing for more than just two contacts, electrostatic gates can be added to supported NTs enabling one to tune the carrier concentration (Fermi energy). A metal electrode (not in direct contact with the NT) or the substrate itself can serve as a gate. In the later case, which is preferred by most researchers, a degenerately-doped Si substrate is used and the isolation between the gate and the NT is provided by a thin oxide layer with a thickness of $0.1 - 1 \mu\text{m}$.

4.5 Electrical Measurements on Single MWNTs

Figure 14 shows the characteristic dependence of the equilibrium electric resistance R on the temperature T for a single MWNT with low-ohmic contacts, where it is shown that $R(T)$ increases with decreasing T . This decrease

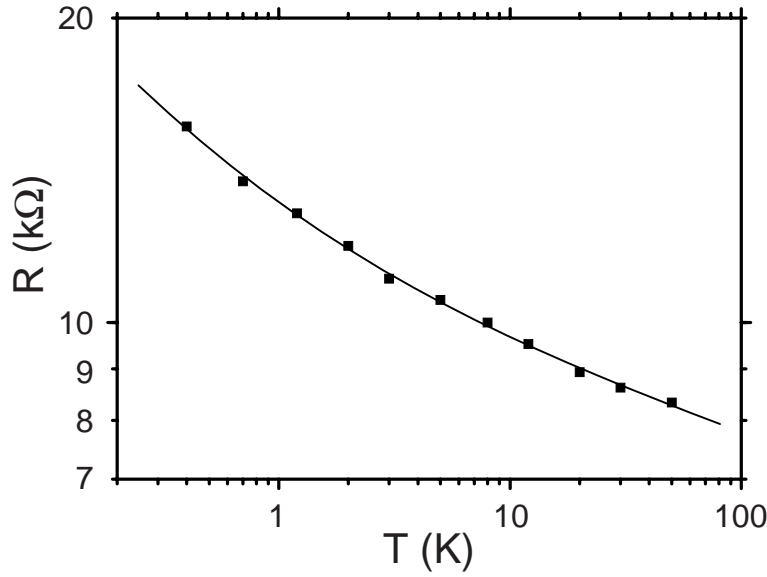


Fig. 14. Four-terminal equilibrium electric resistance R vs T of a single arc-grown MWNT with a contact separation of 300 nm [98]

is rather moderate and distinctly different to what was found in macrobundles and films, discussed in Sect. 4.3, see Fig. 11, where it was found that $R^{-1} = G(T) \propto T$. In contrast, $R(T)$ in Fig. 14 cannot be expressed as a simple power-law, so that if we would try to write $G \propto T^\alpha$, then α would range from 0.07 (100 K) to 0.19 (0.4 K). Hence, the T dependence for a single MWNT is weaker as compared to macro-bundles. According to our previous discussion (Sect. 4, Sect. 4.1), the non-metallic looking behavior of Fig. 14 could be taken as a sign that MWNTs are similar to highly disordered graphite (see Fig. 9). This is, however, not true. Taking $R(300\text{K}) = 6\text{ k}\Omega$, the sheet resistance and the resistivity are found to be $R_\square = 1.3\text{ k}\Omega$ and $\rho = 0.4\text{ }\mu\Omega\text{m}$, respectively. Here, we have used again the fact that R is determined by the outermost metallic SWNT [46]. Only arc-grown graphitic fibers or single-crystalline graphite have shown such low resistivities. But contrary to MWNTs, these ‘clean’ materials display a metallic $R(T)$ -dependence: the resistance decreases with decreasing temperature. Based on R_\square we conclude that single arc-grown MWNT are highly graphitized with a low degree of disorder, comparable to that of single-crystalline graphite, and, that the resistance increase must be a characteristic feature for this tubular one-dimensional form of graphite. The low- T resistance of MWNTs differs also from SWNTs. Measurements on SWNTs almost always display Coulomb blockade (CB) behavior below $\approx 10\text{ K}$ [74,75]. In this regime of single-electron tunneling, the whole NT acts as an island weakly coupled to the environment, i.e., with contact re-

sistances larger than the resistance quantum $R_0 = h/2e^2 = 12.9 \text{ k}\Omega$ [99]. For low applied voltages, R is exponentially suppressed once $kT \ll E_c$, where $E_c = e^2/2C$ is the single-electron charging energy of the NT with capacitance C with respect to the environment. A typical value is $E_c \approx 1 \text{ meV}$ for a $1 \mu\text{m}$ long nanotube segment. Figure 14 is representative for all measured MWNTs with low-ohmic contacts. Coulomb blockade is not observed. According to theory, 2/3 of the tubes should be semiconducting with a substantial band gap (even for MWNTs) of order $E_g \approx 40 \text{ meV}$ for a 20 nm diameter tube. This band gap should give rise to an exponential temperature-dependence, according to $R(T) \propto \exp(kT/2E_g)$ which has never been observed. MWNTs have many tubes in parallel, from which it is clear that the metallic ones will take over at low temperatures. Because the electrodes are in contact with the outermost shell, the outermost metallic NT dominates. If the outermost tube happens to have a gap, a larger contact resistance might be expected because the electrons would have to tunnel from the electrode through the semiconducting tube into the first metallic NT. This also has not been observed until now. Of all MWNTs contacted from above (i.e., with metal evaporated over the NT), appreciably high-ohmic contacts are rare (only 10 %) [44]. A possible explanation could be that the NTs are doped, either intrinsically or due to charge transfer from the metallic contact.

A metallic gate allows study of the dependence of the nanotube conductance on the carrier concentration. Gate sweeps are also important for providing a convincing proof of Coulomb blockade (CB). If $G(T)$ is determined by CB at low T , then G should be periodic in the gate voltage V_g with a period given by e/C . Figure 15 shows two such gate-sweeps for a single MWNT at 0.4 K , one for zero magnetic field, the other in a transverse field of $B = 2 \text{ T}$. Here G is strongly modulated by V_g with rms-fluctuations of order $0.3G_0$ around an average value of $0.8G_0$. Coulomb blockade would result in a periodic modulation with a period in V_g estimated to be 50 mV . But the fluctuations in Fig. 15 occur rather on a scale of 1 V . One might argue that the NT splits into a sequence of smaller islands at low T , which would give rise to a fluctuation pattern with a larger characteristic voltage scale. This picture is quite similar to strong localization for which an exponential resistance increase would be expected at low T , which is not observed. We therefore conclude that CB is not relevant for MWNTs with low-ohmic contacts down to 300 mK .

It is remarkable that $G > G_0$ for certain V_g in Fig. 15. The observed pattern reflects the quantum states in this nanotube segment approaching the 0D limit. The pattern is aperiodic because of random scattering, and the NT behaves like a chaotic cavity. The fluctuation is suggestive of so-called universal-conductance fluctuations (UCF) [100–102].

The upper curve in Fig. 15 demonstrates that the pattern is completely changed in a magnetic field of 2 T . Because the two curves show no correlations, the so-called correlation field $B_c < 2 \text{ T}$. This allows us to estimate the

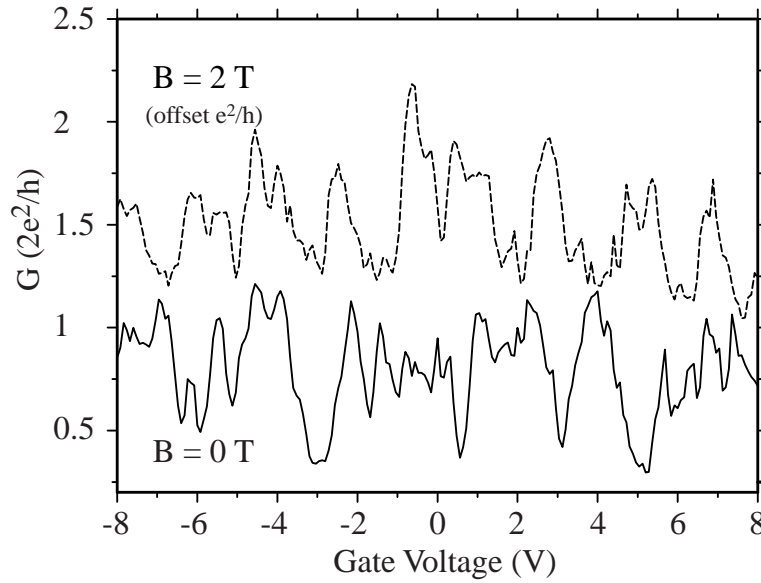


Fig. 15. Conductance of a 300 nm single MWNT segment at $T = 0.4$ K as a function of gate voltage applied to the degenerately doped Si substrate. The nanotube is spaced from the back-gate by a Si-oxide layer 400 nm in thickness. Lower (upper) curve is measured in zero (2 T) magnetic field. The upper curve is offset vertically by e^2/h for clarity [98]

phase-coherence length l_ϕ which must be > 100 nm. Hence, this 300 nm NT segment is certainly 1-D with respect to quantum coherence and even close to 0D (quantum dot). Let us estimate the expected mean level spacing ΔE_{0D} for an ideal NT quantum dot of length L . If spin-degeneracy is removed, then $\Delta E_{0D} = \hbar v_F / (4L)$, amounting to 3 meV for $L = 300$ nm. One now needs to know the leverage factor $\Delta V_g / \Delta E_F$ which we estimate to be 100. Hence, 0D features should show up in the gate-dependence on a voltage scale of order 0.3 V, which is indeed the case.

These measurements also allow us to estimate the mean-free path l_e . Because strong localization is not observed, we conclude that the localization length $l_{loc} > l_\phi$. With $l_{loc} \sim N l_e$, where $N \approx 4$ is the number of modes, we see that $l_e > 20$ nm, so that the mean-free path is of the same order as the diameter of the MWNTs. Hence, there is elastic scattering leading to the interference patterns at low temperature, but this scattering is not strong enough to localize the electron states in the MWNT. This result, that MWNTs are not free of elastic scattering (there is some disorder), has to be contrasted with work of Frank *et al.* [45]. Figure 16 shows the measured conductance G of a fiber of MWNTs while lowering this fiber continuously into a liquid metal (see also Fig. 12). In Fig. 16 we see that G increases in steps of magnitude close to the quantized conductance $G_0 = 2e^2/h$. Each step is due to an additional

MWNT coming into contact with the liquid. The nearly equal conductance of $\approx G_0$ for each MWNT, that makes contact with the liquid Ga, has been taken as evidence for quantum ballistic transport. This effect is very striking, since the experiments in Fig. 16 were done at room temperature. Why the measured G is only one-half of the expected quantized conductance for an ideal metallic NT is not understood at present [103]. The measured $G \approx G_0$ is also in disagreement with other transport measurements on nominally similar MWNTs. For example, the NT in Fig. 14 has a room temperature resistance of only $6\text{ k}\Omega$ which corresponds to $\approx 4e^2/h$. Values for the two-terminal conductance of up to $4G_0$ have been found at room temperature [44]. This is not unexpected because higher subbands contribute to the conductance at room temperature, too. Recall, that the mean-level spacing is only 33 meV for $d_t = 20\text{ nm}$. The result of Frank *et al.* can be summarized as follows: the measured resistance is a contact resistance, which is quantized and the intrinsic NT resistance, determined from the depth-dependence, is small. The latter is in contrast to recently published length-dependent intrinsic resistances of $4\text{ k}\Omega/\mu\text{m}$ [44] and $\approx 10\text{ k}\Omega/\mu\text{m}$ [97], respectively.

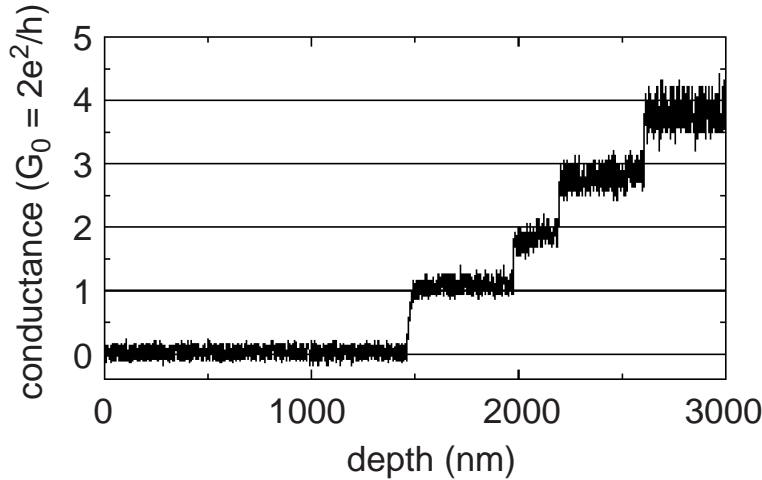


Fig. 16. Conductance G at room temperature measured in the apparatus shown in Fig. 12 as a function of depth of immersion of the nanotube fiber into liquid gallium. As the nanotube fiber is dipped into the liquid metal, the conductance increases in steps of $G_0 = 2e^2/h$. The steps correspond to different nanotubes coming successively into contact with the liquid [104]

To support ballistic transport over micrometer distances, Frank *et al.* came up with another interesting experimental observation. Large electric currents of order 1 mA can be driven through MWNTs without destroying them. Based on the electric power and bulk heat conductivity for graphite, the NT is expected to evaporate due to the large temperature rise. But no melting

is observed. This observation of large current densities may however not be taken as a proof for ballistic transport. Rather, it shows that dissipation is largely absent (which is an exciting fact by itself). In fact, large currents of the same magnitude can be passed through lithographically contacted MWNTs without destroying them, although these MWNTs have been proven not to be quantum-ballistic [44]. An interpretation of this phenomena is difficult because it occurs in the non-linear transport regime for applied voltages much larger than the subband separation [105]

4.6 Magnetotransport

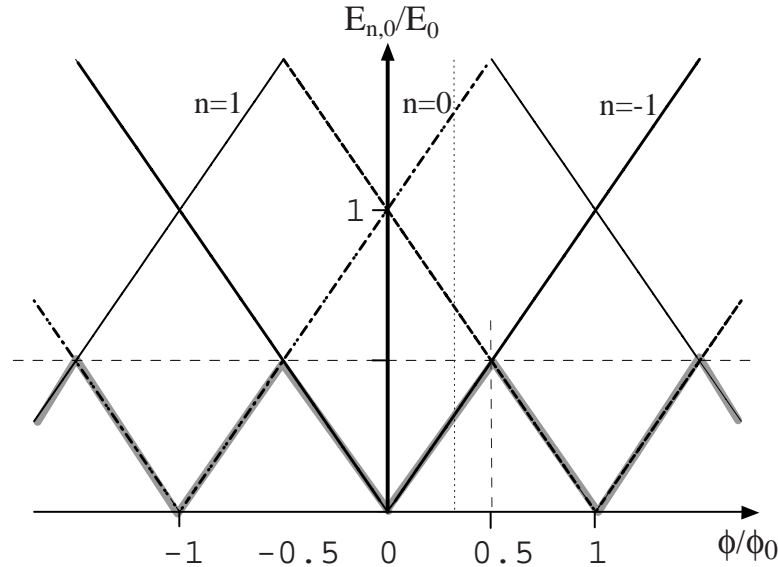


Fig. 17. Cutoff energy $E_{n,0}$ of 1-D-subbands for a (metallic) SWNT as a function of magnetic flux ϕ through the tube. The band structure is periodic in parallel magnetic field with a period given by the magnetic flux quantum $\phi_0 = h/e$. Both $E_{n,0}$ and ϕ and plotted in dimensionless units

We first discuss the magnetoresistance (MR) in a parallel magnetic field B . This case is very appealing because the effect of B on the wavefunction can easily be described. The magnetic flux ϕ through the nanotube gives rise to a Aharonov–Bohm phase modifying the boundary condition of the transverse wavevector k_{\perp} (Eq. 4) into:

$$k_{\perp} = \frac{2}{d_t} (n + \phi/\phi_0 - \nu/3) \quad n = 0, \pm 1, \pm 2, \dots \quad (7)$$

ϕ_0 is the magnetic flux quantum h/e and $\nu = 0, \pm 1$ [62,106]. Similarly, the index n in the approximate 1-D dispersion relation of Eq. 5 is changed into $n + \phi/\phi_0$. It then follows that the cut-off energy $E_{n,\nu}(\phi)$ for the subbands is:

$$E_{n,\nu}(\phi) = E_0 \left| n + \frac{\phi}{\phi_0} - \frac{\nu}{3} \right|. \quad (8)$$

This relation is shown in Fig. 17 for $\nu = 0$. The band structure is periodic in parallel magnetic field with the fundamental period given by ϕ_0 . The drawing corresponds to a metallic tube, for which the cutoff energy is zero for $\phi = 0$. Because ν and the scaled flux appear as a sum in Eq. 8, a metallic tube is turned into a semiconducting one depending on the magnetic flux ϕ/ϕ_0 and vice versa. At half a flux quantum $\phi/2\phi_0$ the band-gap reaches its maximum value of E_0 , corresponding to 65 meV for a SWNT with $d_t = 20$ nm. If, as claimed before, a single nanotube dominates transport in a MWNT, a periodic metal-insulator transition should be observed as a function of parallel field at low temperatures.

The dependence of the electric resistance of MWNTs in a parallel magnetic field has been studied by Bachtold *et al.* [46] and Fig. 18 shows results of a typical magnetoresistance (MR) measurement. If we adhere to the notion that the measured resistance in MWNTs is due to the outermost *metallic* NT, R is expected to decrease because of the appearance of a gap. However, on applying a parallel magnetic field B , the resistance rather sharply *decreases*. It is therefore clear that this effect must have another origin than the band structure modulation that we have just discussed. This decrease is associated with the phenomenon of weak localization (WL) [70–73].

Weak localization originates from the quantum-mechanical treatment of backscattering which contains interference terms, which add up constructively in zero magnetic field. Backscattering is thereby enhanced, leading to a resistance larger than the classical Drude resistance. Because the interference terms cancel in a magnetic field of sufficient strength, WL results in a negative MR. However, for the specific geometry of a cylinder (or ring), the WL contribution is periodic in the magnetic flux through the cylinder, with *half* the AB (Aharonov–Bohm) period $h/2e$ [107]. Indeed, in Fig. 18 the resistance has a second maximum at $B = 8.2$ T. From this field value, a diameter of $d_t = 18$ nm is obtained for this MWNT. As was demonstrated by Bachtold *et al.* [46], the MR agrees with the Altshuler, Aharonov and Spivak (AAS) theory [108], only if the current is assumed to flow through one of outermost cylinders with a diameter corresponding to the independently measured outer diameter of the NT. It is therefore most likely that only one cylinder actually participates in transport. The conclusion that only *one* graphene cylinder carries the current can only unambiguously be drawn from the analysis of the low-temperature MR data ($T < 20$ K). We emphasize that it is not possible to relate the resistance maxima at ± 8.2 T to a magnetic flux of h/e , because a tube diameter would then result which is larger than

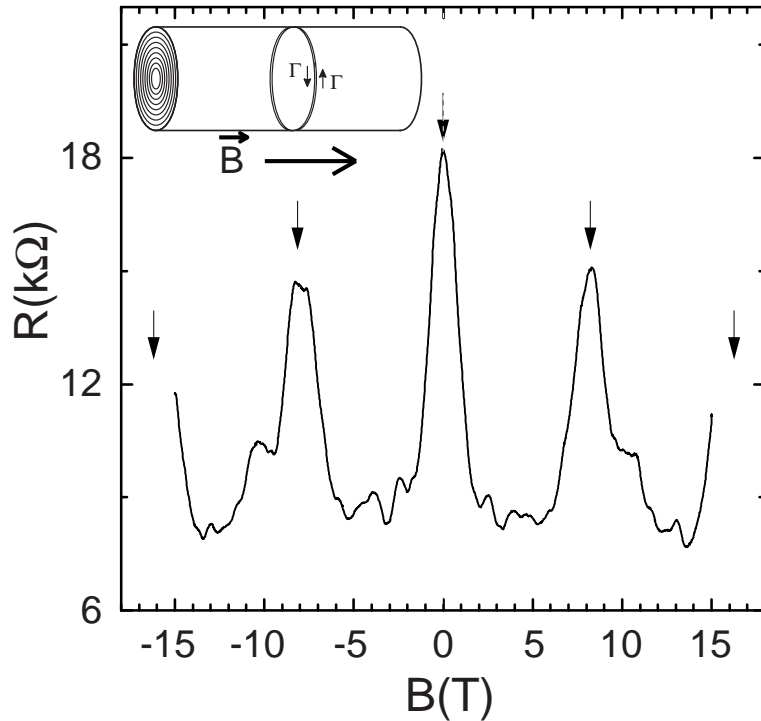


Fig. 18. Electrical resistance R as a function of parallel magnetic field B (see inset showing electron orbit). Arrows denote the resistance maxima corresponding to multiples of $h/2e$ in magnetic flux through the nanotube taking the outer diameter [44]

the actually measured outer diameter. The observation of a pronounced $h/2e$ resistance peak proves that backscattering is present. The NTs therefore do *not* exhibit ballistic transport.

In a parallel magnetic field, resistance maxima should occur periodically. The onset of the second resistance peak, which is expected at $B = 16.4$ T is clearly seen in Fig. 18. From this measurement, a phase coherence of $l_\phi \approx 200$ nm is estimated in good agreement with the estimate given before [44].

Next, we will consider the MR in a perpendicular field, for which the MR has been extensively studied [44,68,69,76,109–111]. A negative MR is found for a transverse B field, in agreement with weak-localization theory [70–73]. Further support for the importance of interference contributions to the transport properties comes from the observation of non-local effects in multi-terminal devices [44],

A typical magnetoresistance (MR) measurement is shown in Fig. 19. On applying a transverse magnetic field, the resistance decreases (negative MR), in agreement with WL theory. Aperiodic fluctuations are observed superim-

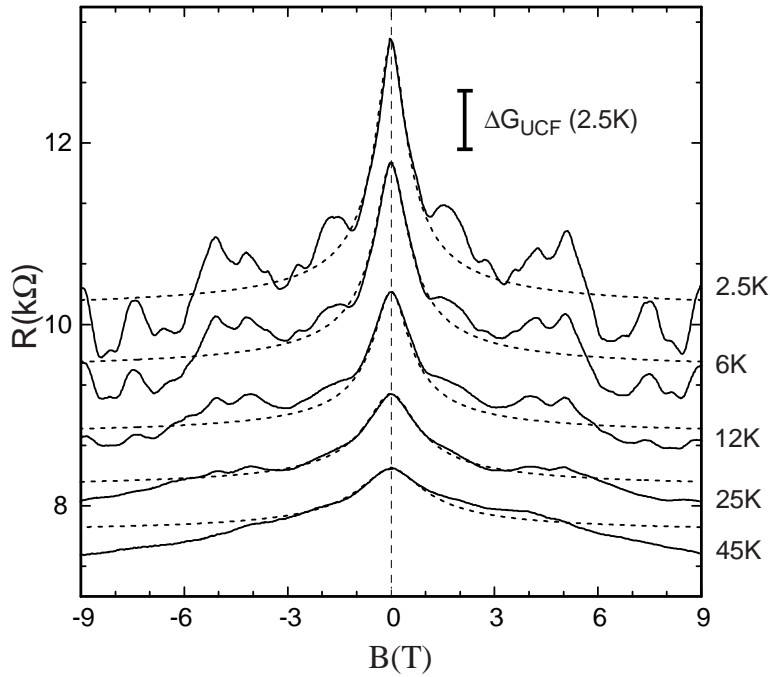


Fig. 19. Four-terminal magnetoresistance of a MWNT in a perpendicular magnetic field for different temperatures. The voltage probes are separated by $1.9 \mu\text{m}$. Dashed curves show fits using one-dimensional weak-localization (1D-WL) theory. Note, that the curves are not displaced vertically for clarity [44]

posed on the negative MR background, and these fluctuations are assigned to universal conductance fluctuations (UCFs). This MR can only be fitted with 1D-WL theory, i.e., $l_\phi > \pi d_t$ ($d_t = 23 \text{ nm}$). Best fits to theory are shown in Fig. 19 by the dashed lines, and a very good agreement is found. As a cross-check, UCF amplitudes deduced using l_ϕ agree with the observation. An example is given by the vertical bar in Fig. 19 which corresponds to the expected UCF amplitude at 2.5 K. Let us estimate the phase coherence length l_ϕ at 2.5 K. The resistance peak at zero field corresponds to a conductance change of $\Delta G = -2.2 \times 10^{-5} \text{ S}$. From $\Delta G \approx -(2e^2/h)l_\phi/L$ we obtain $l_\phi \approx 500 \text{ nm}$. This particular example shows a rather large l_ϕ and correspondingly a surprisingly large diffusion coefficient D and mean-free path l_e . These later parameters can be obtained from the l_ϕ vs T relation for dephasing by quasi-elastic electron-electron scattering (Nyquist noise dephasing [112]) which is the dominant source of phase-randomization at low temperature [44]. One obtains $D = 450 - 900 \text{ cm}^2/\text{s}$ and $l_e = 90 - 180 \text{ nm}$. Again, this mean-free path is in agreement with the condition that $l_{loc} > l_\phi$ from which $l_e > 100 \text{ nm}$ follows.

Another finding in Fig. 19 worth mentioning is that weak localization results in an increase of the electric resistance at low temperatures, but this is not the only contribution to the resistance increase. For large magnetic fields $\delta G_{WL} \rightarrow 0$ but the resistance is still seen to be strongly temperature dependent. Here we note that the curves in Fig. 19 are not displaced for clarity, but rather a temperature-dependent background resistance is observed and this effect is usually associated with electron-electron interaction. While WL primarily enters as a correction to the diffusion coefficient, the carrier-carrier interaction suppresses the single-particle DOS. For a diffusive wire for which the coherence length (the thermal length) is larger than the width but smaller than the length, theory predicts a temperature dependence for the conductance correction $\delta G_{ee} \propto T^{-1/2}$ [113–115]. Knowing $\delta G_{WL}(T)$, one can then plot $G(T) - \delta G_{WL}(T)$ as a function of \sqrt{T} .

It turns out, however, that this relation does not hold [70–73]. The interference and interaction corrections δG_{WL} and δG_{ee} are derived by WL perturbation theory and are therefore assumed to be small. But exactly this assumption is not valid here. One therefore needs to treat the interaction exactly.

This is indeed possible in 1-D, using bosonization techniques. Carbon nanotubes are predicted to become so-called Luttinger liquids (LL) in which a pseudo-gap in the quasi-particle DOS opens at low energy [116–120]. A perfect ballistic LL cannot be distinguished from the perfect Fermi liquid quantum wire in an equilibrium transport measurement whereby G is just quantized to $2e^2/h$ (for one mode). However, with backscattering, G is renormalized. In the so-called strong backscattering limit (low T limit) $G \propto T^\alpha$ with a weaker T -dependence at higher temperatures. For a SWNT $\alpha \approx 0.3 - 0.8$, while α can be reduced to lower values in MWNTs due to the enhanced screening by multiple shells [121]. Though $R(T)$ in Fig. 14 does not follow a power law, the temperature dependence of R is not inconsistent with LL theory. This dependence is expected for a LL in the weak-backscattering limit. LL theory includes the electron-electron interaction. In addition, scattering has been incorporated into the theory. However, the dependence on magnetic field has not yet been treated. It would be very interesting to see whether such a ‘complete’ theory could explain the measured MR, which can surprisingly be fitted quite well with theoretical results from WL perturbation theory based on Fermi-liquid quasi-particles [44,46,61,62]

4.7 Spectroscopy on Contacted MWNTs

Figure 20 shows a differential current-voltage characteristic (dI/dV) measured on a single MWNT, using an inner contact which by chance was high-ohmic. This particular tunneling contact had a contact resistance of $300 \text{ k}\Omega$, whereas the other contacts had resistances $\ll 10 \text{ k}\Omega$. The measured spectrum agrees surprisingly well with predicted spectra based on simple tight-binding calculations for a metallic NT [106,122,123]. Firstly, there is a substantial

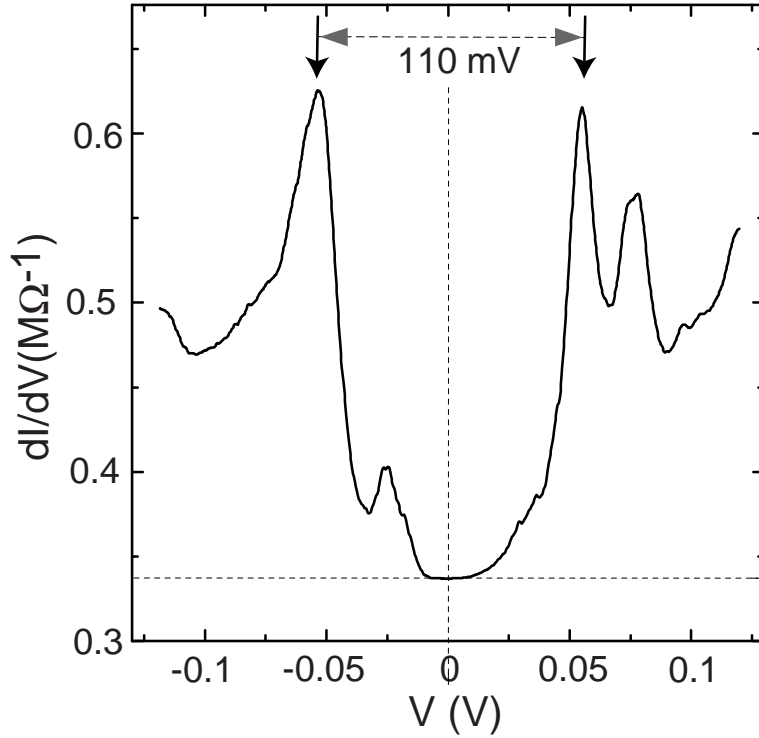


Fig. 20. Differential (tunneling) conductance dI/dV measured on a single MWNT using a high-ohmic contact ($300 \text{ k}\Omega$) at $T = 4.2 \text{ K}$ [44]. This spectrum qualitatively confirms the DOS expected for a metallic nanotube in which the wave vector is quantized around the tube circumference leading to 1D-subbands. Positive (negative) voltages correspond to empty (occupied) nanotube states

DOS at the Fermi energy, i.e., at $V = 0$, so that the NT is metallic. Secondly, the almost symmetric peak structure, appearing as a pseudo-gap is caused by the additional 1D-subbands in the valence band ($V < 0$) and conduction band ($V > 0$) with threshold energies of order $\approx 50 \text{ meV}$. At the onset of the subbands, van Hove singularities are expected. The spectrum in Fig. 20 agrees remarkably well with scanning-tunneling measurements of Wildöer *et al.* for SWNTs [63,64]. But because of the difference in tube diameter, the energy scales are quite different. These subbands should be spaced by $2E_0 = 4\hbar v_F/d_t = 150 \text{ meV}$ for the MWNT in Fig. 20 which has $d_t = 17 \text{ nm}$. The measured spacing of 110 mV is in reasonable agreement with this estimate. The observation of van Hove features in dI/dV demonstrates that the mean-free path l_e cannot be much shorter than the nanotube circumference. If $l_e < \pi d_t$, all 1-D band structure features would be expected to be washed out. The observed spectrum in Fig. 20 nicely demonstrates that the unusual

band structure effects of NTs are also found for MWNTs. In most cases, however, the measured spectral features are not as sharp.

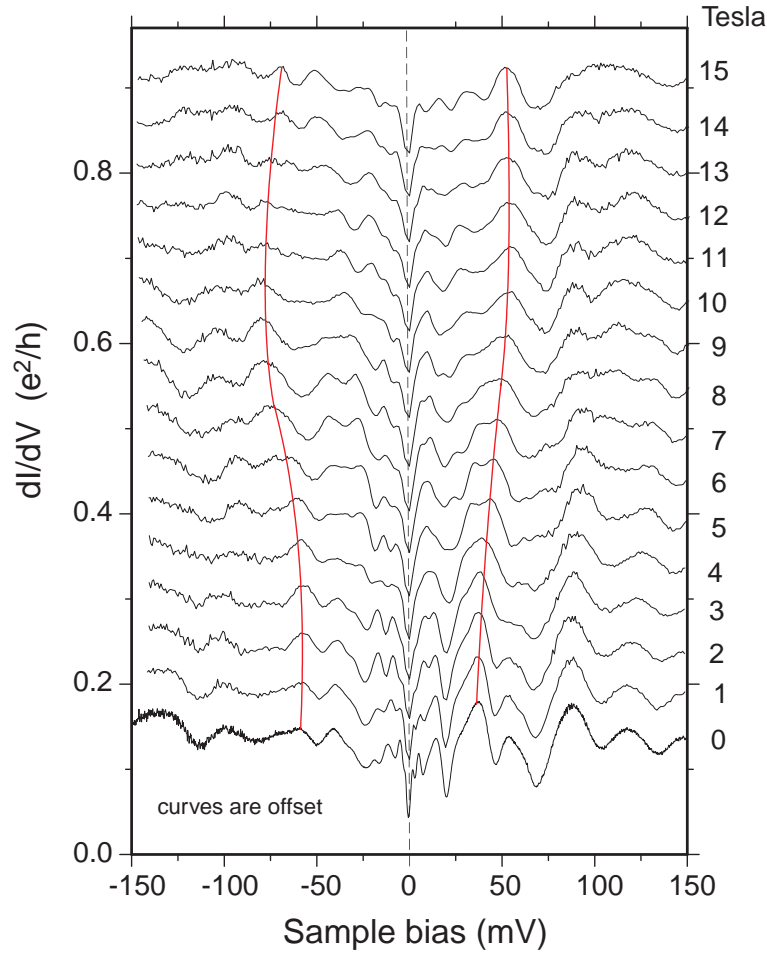


Fig. 21. Tunneling dI/dV spectra measured on a single MWNT using a high-ohmic contact for different magnetic fields B applied parallel to the tube [124]. Note, that the spectral features shift in a magnetic field (lines are a guide to the eyes for two well discernible peaks), and that there is a pronounced anomaly at $V = 0$. All curves are vertically displaced for clarity [124]

Furthermore, the prevailing dI/dV spectra display a pronounced zero-bias anomaly on a smaller energy scale of 1 – 10 meV. Such a tunneling spectra is shown in Fig. 21. These spectra are highly structured. The observed peaks are associated with broadened van Hove singularities due to the 1-D-band

structure. This assignment is strongly supported by the observed peak-shifts in a parallel magnetic field B . The peaks are seen to move up and down with B in accordance with the Aharonov–Bohm effect. According to Fig. 17, the total peak shift amounts to $E_0/2$, corresponding to 39 meV for this MWNT ($d_t = 17$ nm). The measured, shifts are somewhat smaller, ≈ 22 meV. With the exception of small voltages, i.e., for $|V| < 25$ meV, the mean peak spacing is ≈ 25 meV, in agreement with the maximum peak shift. In addition to the peaks, there is a pronounced zero-bias anomaly (ZBA). At $V = 0$ the conductance is strongly suppressed, independent of B . This suggests that a pseudo-gap opens for low-energy quasi-particles. This finding must be related to the measured resistance increase at low temperature, as shown in Figs. 14 and 19.

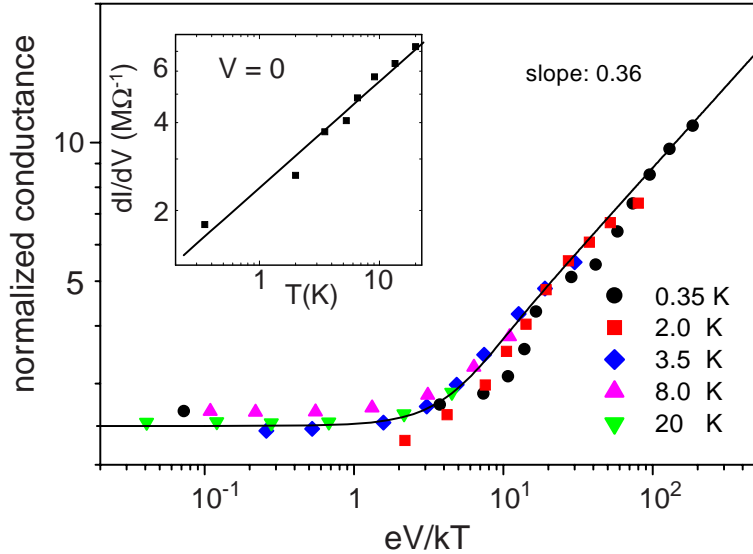


Fig. 22. Normalized differential tunneling conductance $dI/dV \cdot T^{-\alpha}$ vs scaled voltage eV/kT measured on a single MWNT using a high-ohmic contact. The inset displays the equilibrium conductance as a function of temperature T on a log-log plot. The straight line corresponds to $\alpha = 0.36$ [95]

Figure 22 shows a detailed analysis according to Bockrath *et al.* [125] of a zero-bias tunneling anomaly measured on a MWNT for different temperatures. The ZBA anomaly exhibits power-law scaling, i.e., $dI/dV \propto V^\alpha$ if $eV \gg kT$ and $dI/dV \propto T^\alpha$ if $eV \ll kT$. Such a dependence is in agreement with Luttinger liquid models [126]. Similar anomalies have recently been observed by Bockrath *et al.* for SWNTs [125]. Their measurement and analysis provide the first demonstration of Luttinger liquid (LL) behavior in carbon NTs.

The LL liquid theory describes the interaction with a single parameter g [126]. The non-interacting Fermi-liquid case corresponds to $g = 1$ and $0 < g < 1$ is valid for a LL with repulsive interaction. The parameter g is determined by the ratio of the single-electron charging energy to the single-particle level spacing and has been estimated to be $g = 0.2 - 0.3$ for SWNTs [120]. Because a MWNT consists of several shells, one might expect that the inner shells strongly screen the long-range Coulomb interaction leading to $g \rightarrow 1$, i.e., to an effectively non-interacting Fermi liquid. However, it has recently been shown that g is only weakly modified and theoretically only scales with \sqrt{N} where N is the number of shells participating in screening [121]. Although there about 20 shells, the effective N is expected to be smaller and is only of order 1. LL behavior is therefore expected for MWNTs, too. Regarding the exponent α , one distinguishes ‘bulk’ from ‘end’ tunneling. The measurement in Fig. 22 corresponds to bulk tunneling for which $\alpha = (g^{-1} + g - 2)/8$ [120]. From the experiment $\alpha \approx 0.36$, which relates to an interaction parameter of $g = 0.21$. The same value was obtained by Bockrath *et al.* for SWNTs [125]. Currently, more evidence for LL liquid behavior in nanotubes (including MWNTs) is appearing [98,127–129].

4.8 Spectroscopy using Scanning Tunneling Probes

The individual tubes in a MWNT have helicities, described by the (n, m) indexes, and the electronic structure calculations [28,47] for the SWNTs are also valid for the individual nanotubes in MWNTs. In principle, one can find metallic, or semimetallic nanotubes, if $n - m = 0$, modulo 3 is satisfied, or else the individual tubes are semiconducting, if $n - m \neq 3q$, $q = 0, 1, \dots$. There seems to be some commensurability effect in play between the different layers, since the number of chiral angles observed in HRTEM is lower than the number of cylinders forming the MWNT [21]. Theoretically it has been predicted than even in the case of metallic layers, the nested nature of the tubes of different chiralities may introduce gaps or pseudo-gaps in the density of states in a similar way, as happens in the case of SWNTs organized in a bundle [130]. This is in contrast with graphite, where the interlayer interaction between the zero-gap semiconducting graphene layers creates a finite density of states at the Fermi level, making graphite metallic.

The electronic structure can be measured very reliably by STM. This technique was used to image the chirality and to measure the local density of states for SWNT [63,64]. The lateral confinement of the electronic states due to the tubular structure causes symmetric singularities in the DOS, which also help to identify the tube chirality, since there is a reliable correspondence between the peak positions, diameter and chiral indexes. Carroll and coworkers have measured the local density of states (LDOS) of multiwall carbon nanotubes for different tube diameters scanning along the tube axis towards the tips (see Fig. 23) [131]. Scanning far from the ends, the measurements show the outer layer of the tubes indicate a conducting character consistent

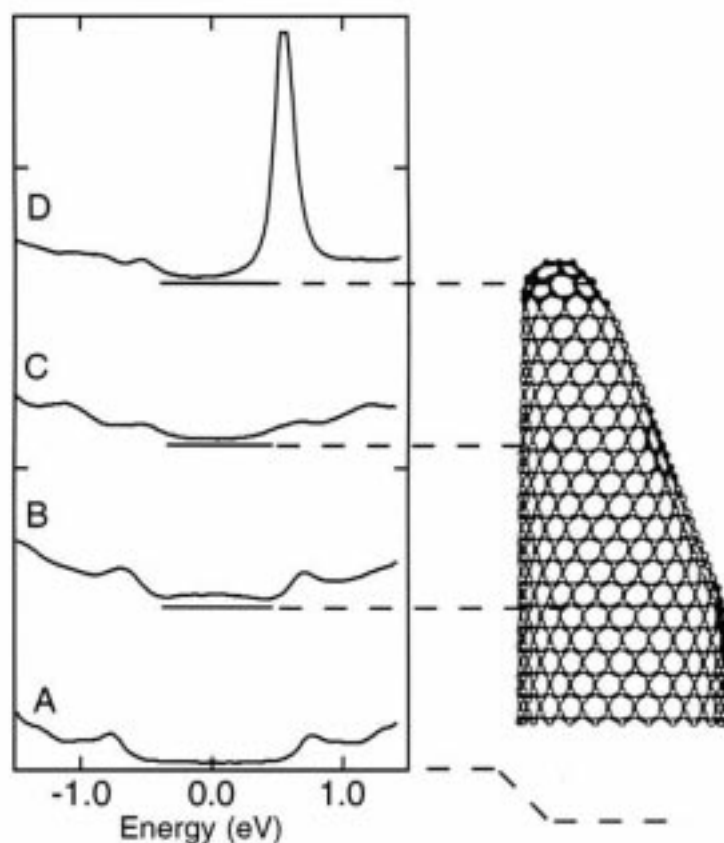


Fig. 23. Measured carbon nanotube differential conductances, proportional to the local density of states, along various positions near the tip (scans at B,C,D locations on the nanotube) and far from the tip (scan A) of a multiwalled carbon nanotube. The sharp peak near the Fermi level of the uppermost trace demonstrates the existence of a localized tip state [131]

with a graphitic-like density of states at low bias and symmetric singularities with respect to zero bias, due to 1-D quantum confinement. At the nanotube tip, the STM spectra show a localized state, whose position and width varies depending on the nanotube tip structure. Calculations have shown that the strength and the position of these states with respect to the Fermi level depend sensitively on the relative positions of the pentagons and their degree of confinement at the tube ends.

4.9 Discussion of the Main Issues

From the previous discussion, four basic issues emerge, which need further attention in the future: (1) Why does transport appear to be ballistic in one experiment and diffusive in another? (2) What is the origin of scattering? (3) What causes hole doping and what is the energy of the doping level in single MWNTs? (4) What is the ground-state of carbon nanotubes?

Let us briefly discuss these questions. Electric transport measurements on single MWNTs give conflicting results. While Frank *et al.* [45] find ballistic transport, there is convincing evidence for diffusive transport from other experiments [44,46,68,69,97]. It is important to emphasize that the estimates for the mean-free path l_e from the latter experiments vary substantially, from $l_e \approx 1$ nm to $l_e > 100$ nm. Taken this fact into account, the first question should be rephased to read: what is the reason for the *large variation* of scattering lengths that are observed in experiments on single MWNTs? This question immediately leads to the second question. What is the origin of the scattering? Are MWNTs defective, is the band structure modified by intertube hybridization, are there inclusions, or is the scattering caused by adsorbates? What is the role of the substrate on which the nanotubes resides in experiments using micro-fabrication? Arc-discharge grown MWNTs appear to be essentially defect-free in TEM micrographs. Furthermore, there is no evidence for bond defects from electron-spin resonance.

From the experiments and the discussion in this section the electronic intertube coupling is expected to be relatively weak. It is therefore believed that scattering is related (at least partly) to the issue of doping. MWNTs (and SWNTs) are found to be hole-doped in experiments on films and macro-bundles. Though the origin of the unintentional doping is not known yet, the apparent doping level can be changed in SWNTS if the nanotubes are heated to only 200 °C in high-vacuum [91]. This suggests that (part) of the doping might be caused by species present in air (for example by oxygen). Until now, the doping-level has not been specified in any experiment on a single MWNT. We need to find a way to quantify the doping level in the future.

The fourth question, finally, is a very intricate one: What is the ground-state of carbon nanotubes? A lot of measurements (e.g., magnetotransport) can be described by either non-interacting or only weakly interacting quasi-particles using theories like weak-localization based on the Fermi liquid (FL) hypothesis. On the other hand, clear deviations from FL behavior has been observed too. The suppression of the quasi-particle density of states, observed in tunneling spectroscopy on single MWNTs (and SWNTs), suggests that nanotubes may develop a Luttinger liquid (LL) state. The ground-state question has become an even more exciting issue, because signatures for intrinsic superconductivity have recently appeared [132].

5 Magnetic properties

The magnetic properties of carbon nanotubes can be effectively monitored by the electron spin resonance (ESR) technique which has been intensively used to study the electronic properties of graphitic and conjugated materials [133]. This method has several advantages: it has a very high sensitivity, it responds only to the paramagnetic signal (unless static measurements are made, which are usually dominated by the large diamagnetic response), and it can distinguish between different spin species, e.g., localized and conduction electron spins. Three different quantities are determined by ESR: (1) the g -factor, which depends on the chemical environment of the spins via spin-orbit coupling (and also the hyperfine interaction); (2) the linewidth, which is governed by the spin relaxation mechanism; and (3) the intensity of the signal, which is proportional to the static susceptibility.

For MWNTs we are mainly interested in the ESR response of the conduction electrons. The conduction electron spin g -factor is determined by the spin-orbit splitting of the energy levels in the presence of a magnetic field [134,135]. In the case of degenerate bands (as in graphite at the K point), theory predicts that spin-orbit coupling, which removes the degeneracy, induces a large g -shift which varies inversely with temperature. This is exactly what is observed in graphite when the magnetic field is perpendicular to the plane, allowing large orbital currents, thereby increasing the spin-orbit coupling. When the magnetic field is parallel to the planes, orbital currents are suppressed, and a small g -shift, nearly independent of temperature, is observed. When the Fermi level is shifted away from the K point by doping, degeneracy and the g -shift anisotropy disappear. (Despite this understanding of the variation of the g -shift, a rigorous theory is still missing in graphite due to the complicated band structure near the point of degeneracy.)

Using this qualitative description for graphite, one can speculate about the g -factor for carbon nanotubes. When the magnetic field is parallel to the tube axis, nearly the same value is obtained for the g -factor as is found in graphite when the field is in the plane, except at a field for which the cyclotron radius equals the geometrical radius of the nanotubes. Such fields (typically 1T and greater) are higher than those used in X-band spectrometers (~ 9 GHz).

When the magnetic field is perpendicular to the tube axis, orbital currents cannot completely close, as in a plane, and we can therefore expect a smaller g -shift than in graphite. A decrease of this g -shift with decreasing tube diameter is then expected. Some of these predictions are indeed realized in MWNTs [136]. The average observed g -value in MWNTs is 2.012, as compared to 2.018 in graphite, and the g -factor anisotropy is lower in MWNTs than in graphite.

Spin relaxation in metals and semimetals depends also on the spin-orbit coupling. More precisely it is the modulation of the spin-orbit coupling by lattice vibrations that causes spin relaxation. It can be shown, that in the framework of the Elliott theory [135], and when the spin relaxation time is

proportional to the momentum relaxation time, and is governed by phonon scattering, the linewidth increases with increasing temperature. Opposite to this expectation, in graphite the linewidth increases when the temperature decreases. This behavior in graphite is attributed to motional narrowing over the g value distribution. Because of the semimetallic nature of graphite, the density of states at the Fermi level is low, and hence the spin susceptibility is low, and is in the 10^{-8} emu/g range at room temperature [133]. We have seen that the g -factor in MWNTs, a local property, is very close to that of graphite. In the following subsections we will see how the spin relaxation and spin susceptibility are modified in MWNTs relative to graphite. Changing the dimensionality from 2-D to 1-D is expected to significantly modify the principal ESR characteristics. First, we have to understand what kind of ESR signal should be expected in a 1-D system.

5.1 Spin relaxation in quasi-1-D systems

Extensive studies of the conduction electron spin resonance (CESR) linewidth (ΔH) in isotropic metals have shown that the dominant process in the spin-lattice relaxation time (T_1) is the spin-flip scattering of conduction electrons by acoustic phonons. The same scattering process gives the momentum relaxation time τ_R measured by the electrical resistivity. Elliott has derived [134,135] a relation between the two relaxation times:

$$T_1 \sim \tau_R / (\Delta g)^2 \quad (9)$$

where Δg is the difference in g -factor between graphite and the free electron value, which reflects the strength of the spin-orbit coupling constant. Since $(\Delta g)^2$ is of the order of 10^{-4} – 10^{-6} , Eq. 9 indicates that one in every 10^4 – 10^6 scattering events contributing to the resistivity gives a spin-flip, and hence the CESR linewidth can be written as

$$\Delta H = 1/\gamma T_1 \sim (\Delta g)^2 / \tau_R. \quad (10)$$

For the majority of isotropic metals, T_1 is too short to give an observable CESR linewidth at room temperature. Beuneu and Monod [137] have verified the Elliott relation for most of the metals. It is well-known that the Elliott relation is violated for quasi-one-dimensional metals, such as TTF-TCNQ [138], where the linewidth does not show strong correlation with the spin-orbit coupling. Materials with similar Δg and conductivity values as TTF-TCNQ, have quite different CESR linewidths and their T_1 values lie well below the universal curve established by Beuneu and Monod [137]. It is presently believed that the source of this disagreement lies in the low-dimensionality of these compounds [139]. In a strictly 1-D system the Fermi surface consists of two points at k_F and $-k_F$. The possible scattering events are thus limited to those with $q \sim 0$ (forward) and $q \sim 2k_F$ (backward) momentum changes. The former process has a very small weight (even including

3-D phonons), while the latter process, reversing spin and momentum, is forbidden by time reversal symmetry. Hence to account for the observed finite ESR linewidth of quasi 1-D conductors, one has to include inter-chain scattering, because every process which could make the system resemble an isotropic metal, will broaden the line.

5.2 Spin relaxation in carbon nanotubes

Isolated SWNTs, without inter-chain interactions, seem to be the ultimate 1-D conductors. Application of the ideas developed in Sect. 5.1 should result in a very narrow and very saturable ESR line, since most of the spin-relaxation channels are switched off. Surprisingly, no conduction ESR signal has been observed in SWNTs until now. One reason for the absence of an ESR line for the conduction electrons in SWNTs might be the strong electron-electron correlation, giving rise to the so-called Luttinger liquid (LL) character of the 1-D electronic system. The ground state of a LL would be antiferromagnetic, which is ESR silent at resonance fields close to that expected for non-interacting electrons. However, there might be a less attractive reason for the absence of a CESR signal in SWNTs, and this is the presence of magnetic particles, which serve as catalysts for the SWNT synthesis, and afterwards remain in the actual SWNT samples as impurities. Because of the long carrier mean free path, and because of the even longer spin diffusion length, even a small concentration of magnetic particles can relax the conduction electrons very efficiently, causing the line to be unobservably broad. Although the MWNTs are less 1-D in comparison to SWNTs, (i.e., the MWNTs should rather be approximated by a quasi-1-D system, because of their multilayered structure and larger diameters), we believe that some signs of low-dimensionality are still present regarding the spin relaxation behavior.

Evidence for low dimensional behavior can be recognized in Fig. 24, where the ESR signal is plotted for MWNT soot with different MWNT densities: the upper signal is recorded for a dense thick MWNT film, while the lower one is the signal of MWNTs dispersed in paraffin. The ESR linewidth for the upper trace is 32 G, while for the lower trace, it is only 8 G. This demonstrates that when the phase space is increased by bringing the individual nanotubes into better contact with each other, the spin-relaxation increases like in a quasi-1-D conductor when hydrostatic pressure is applied [140]. This behavior is specific to nanotubes and it is contrary to what happens in graphitized carbon blacks. Indeed, with carbon black particles or fine graphite powder, increasing the contact between grains increases the motional averaging of the g -factor anisotropy which decreases the linewidth. We believe that the different behavior of the nanotubes is the fingerprint of their mesoscopic nature.

The temperature dependence of the ESR linewidth, shown in Fig. 25, is also unusual. In graphite ΔH increases with decreasing temperature, and

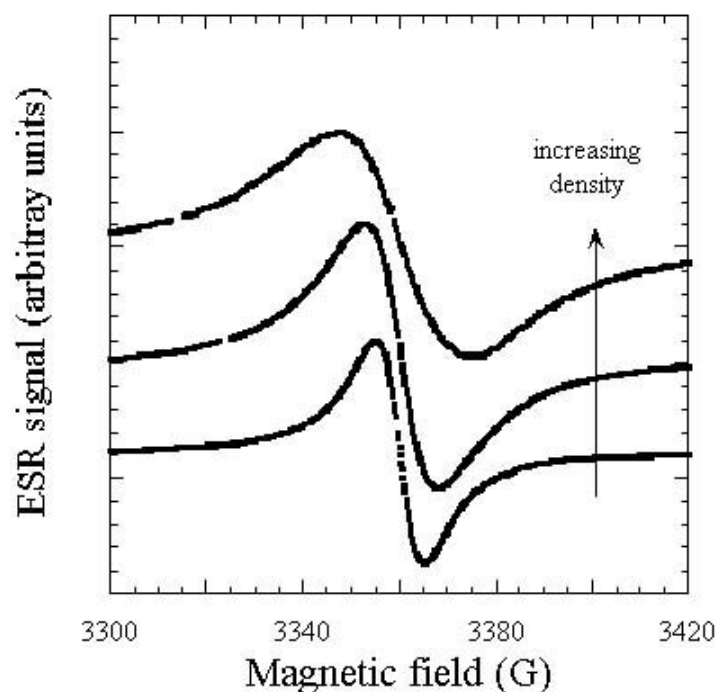


Fig. 24. The CESR signal of MWNTs for samples with different MWNT densities measured at 300 K as a function of the magnetic field. The intensities are not to scale. The upper signal is recorded for a dense MWNT thick film, while the lower one is the signal of MWNTs dispersed in paraffin. The narrowing linewidth with decreasing MWNT density is a fingerprint of low-dimensional spin-relaxation phenomena [141]

passes through a broad maximum. This “anomalous” temperature dependence of ΔH in graphite was ascribed to the same phenomena that is responsible for the observed temperature dependence of the g -factor. In the case of highly purified MWNTs, this close correspondence between the two quantities breaks down as T falls below 100 K. Whether the decoupling of the two quantities at low temperatures is once again the sign of low-dimensional effects would require that detailed calculations of the spin and momentum relaxation be carried out for MWNTs.

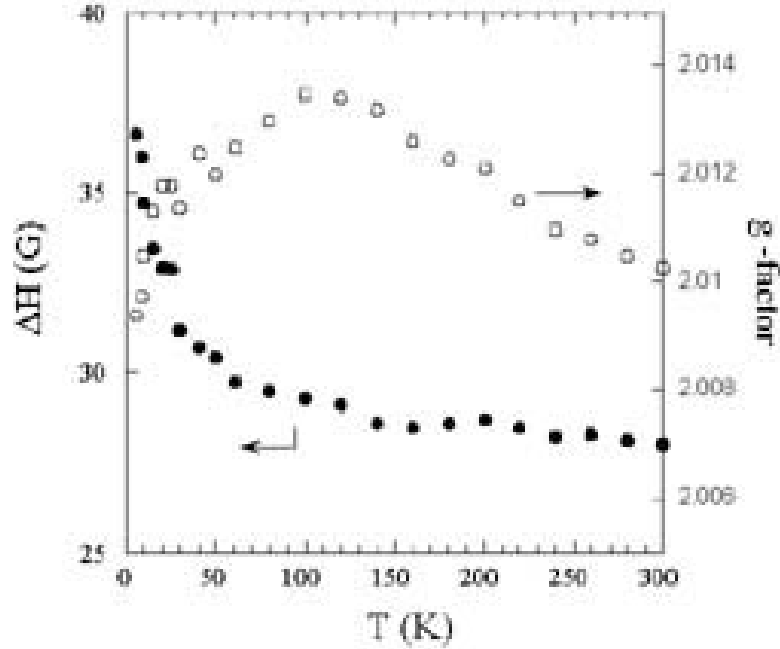


Fig. 25. The temperature dependence of the CCSR linewidth and the g -factor for a highly purified thick film of MWNTs. The distinct temperature dependence for these two quantities might be also characteristic for single wall carbon nanotubes [141]

The spin susceptibility χ_s for MWNTs is derived from the ESR signal strength by numerical integration. Above 40 K (Fig. 26), we find a temperature independent (Pauli) susceptibility $\chi_s = 7 \times 10^{-9}$ emu/g. In comparison, for powdered graphite, we find $\chi_s = 2 \times 10^{-8}$ emu/g, consistent with reported values between $1\text{--}4 \times 10^{-8}$ emu/g [133,142]. The Pauli behavior indicates that the aligned nanotubes are metallic or semi-metallic. For free electrons, the Pauli susceptibility is given by $\chi_s = \mu_B^2 N(E_F)$ where μ_B is the Bohr magneton and $N(E_F)$ is the density of states at the Fermi level. The measured susceptibility for MWNTs (Fig. 26) gives $N(E_F) = 2.5 \times 10^{-3}$ states/eV/atom. This density of states is comparable to that of graphite [142]. Estimating the carrier concentration n given by $n = E_F N(E_F)$ and taking the Fermi energy E_F for the MWNTs to be equal to that of graphite (200 K) gives

$n \sim 4 \times 10^{18} \text{ cm}^{-3}$. Although this estimate is very crude, it is, however, consistent with Hall measurements for the same sample [143], which gives an upper limit of $n = 10^{19} \text{ cm}^{-3}$. This low carrier density is consistent with the MWNTs being semimetallic.

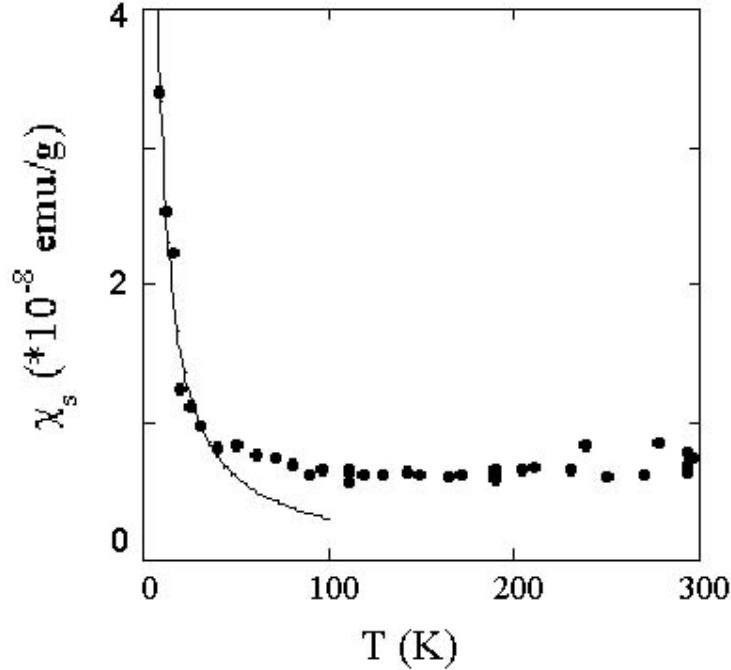


Fig. 26. The temperature dependence of the ESR susceptibility of highly purified MWNTs [141]

ESR measurements are also suitable for characterizing the defects in carbon nanotubes by their appearance in the Curie-tail (see Fig. 26). It is suspected that arc-grown MWNTs contain a high defect density that modifies their electronic properties [143]. Among these defects, vacancies and interstitials can generate paramagnetic centers that can be detected by ESR. Pentagon-heptagon pair defects can also be present in the lattice. The low temperature upturn of $\chi_s(T)$ closely follows a Curie law (solid line, Fig. 26), and is thus a signature of localized spins, arising either from the localization of the carriers or from impurities. In either case, the Curie-tail corresponds to 1.3×10^{-5} spins/C atom. This means that arc-grown MWNTs contain a very low density of paramagnetic defects. No substantial modifications were observed in the Curie-tail after annealing the sample at 2800°C .

Summarizing the magnetic properties seen by ESR, the MWNTs show a mesoscopic nature in their spin relaxation. The expected manifestation of strong electron-electron correlations by an enhanced spin susceptibility is absent. Instead, MWNTs exhibit a $\chi_s(T)$ dependence similar to that of graphite. MWNTs prepared by the arc-discharge method are very pure. This fact does not apply to catalytically grown MWNT samples, which have a higher defect density, and the observation of an ESR signal is precluded by the magnetic impurities left behind in these samples even after purification of the soot.

6 Field and light emission

It was very early realized that carbon nanotubes are efficient field emitters [37]. Field emission from individual MWNTs was demonstrated by attaching a nanotube to a conducting wire and observing the current after applying a negative potential to the wire [144]. Also high electric currents were found to produce emission electrons from carbon nanotube films above which an extracting grid was placed [145]. From the latter studies, it was concluded that carbon nanotube films could be used as field emission guns for technical applications, such as flat panel displays [145,146]. Five years after the initial concept was demonstrated, Samsung Advanced Technology Institute is already manufacturing a prototype of a color display, ready to commercialize this concept [37].

When studying the field emission properties of MWNTs, it was noticed that together with electrons [37], light is emitted as well [147]. This light emission occurred in the visible part of the spectrum, and could sometimes be seen with the naked eye. Since MWNTs are excellent scanning probe tips, their light emitting property should find application in Scanning Near-field Optical Microscopy. In our opinion the electron and light emission properties are very important features of carbon nanotubes. The electron emitting characteristics of thin films for large scales applications are treated by Ajayan and Zhou [37]. Here we present the essential characteristics of the coupled electron and light emission properties of individual MWNTs.

6.1 Field emission

Field emission results from the tunneling of electrons from a metal into vacuum under application of a strong electric field. The tunneling mechanism is described in the WKB approximation for emission from metal surfaces which leads to the well known Fowler–Nordheim equation:

$$I = \alpha E_{\text{eff}}^2 \exp(-\beta/E_{\text{eff}}) \quad (11)$$

where, α is a constant related to the geometry, E_{eff} is the effective field at the emitter tip, and β is a constant which is proportional to the work function.

The electric field at the nanotube tip depends on the applied nanotube to grid voltage, the nanotube radius, and the nanotube length. E_{eff} can be as much as 1200 times higher than E_0 , which is the grid to cathode voltage divided by the grid to cathode distance, so that field emission is readily achieved even for relatively low applied potentials.

The field emission of individual nanotubes was studied by Bonard and coworkers [7,148] in order to extract the parameters and fine details of the electron emission process. Their experimental configuration is shown in Fig. 27, which displays a typical I-V curve for a single MWNT (in this case an opened MWNT). Most single MWNT emitters, closed as well as opened MWNTs, are capable of emitting over an incredibly large current range. In this study, the maximal current that was drawn from one nanotube was 0.2 mA, and MWNTs can reach 0.1 mA routinely and repeatedly. This represents a tremendous current density for such a small object, and is actually quite close to the theoretical limit where the tube should be destroyed by resistive heating [144].

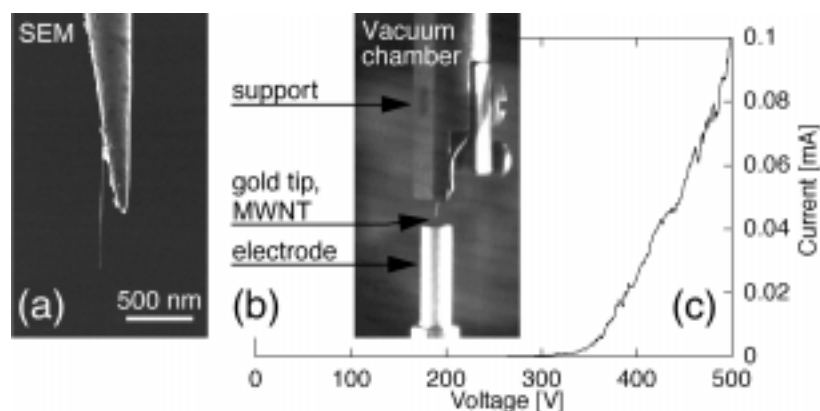


Fig. 27. (a) A single MWNT mounted on the tip of an etched gold wire. (b) Optical micrograph of the experimental set-up for field emission: the gold wire is fixed on a support, and placed 1 mm above the cylindrical counter-electrode. (c) I-V characteristics for a single opened MWNT [8,148]

The field emission study of individual tubes shows also the importance of the tip structure (Fig. 28). Keeping the same parameters for opened and closed MWNT, the turn-on voltage for the opened MWNT is considerably higher, which suggests that the localized states at the dome-structured tip play an important role in the field emission process, so that nanotubes cannot be considered as ordinary metallic emitters. This conclusion is supported by the systematic deviations from the Fowler–Nordheim model (Eq. 11) observed at high emission currents. Furthermore, the energy spread of the emission

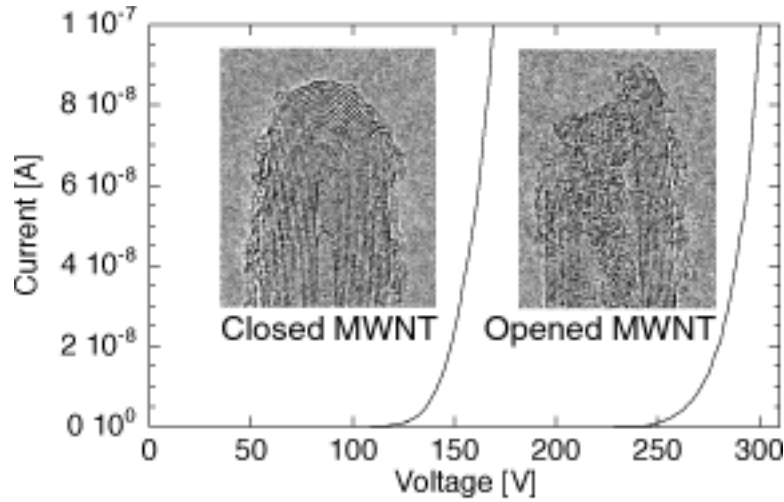


Fig. 28. I-V characteristics for a single closed and opened MWNT, and the corresponding TEM micrographs of typical NT tips[7]

from nanotubes is very narrow (about 0.2 eV). This energy spread is typically half that of metallic emitters. These observations strongly suggest that the electrons are not emitted from a metallic continuum as in usual metallic emitters, but rather from well-defined energy levels, corresponding to localized states at the tip. Actually, the fit of the energy spread profile of the emitted current gives quite a narrow band of levels rather than a discrete energy level, but the shape of the intensity profile leaves no doubt that the emission does not happen from a metallic continuum. The broadening of the localized state might be due to interaction with the continuum [145].

In fact, theoretical calculations and STM measurements on SWNTs and MWNTs show that there is a distinctive difference between the electronic properties of the tip and the cylindrical part of the tube [131]. For MWNTs, the tube body is essentially graphitic, whereas SWNTs display a characteristic DOS [63,149] that reflects their one-dimensional character. In contrast, the local density of states at the tip exhibits sharp localized states that are correlated with the presence of pentagons, and most of the emitted current comes from occupied states just below the Fermi level.

The major factors that determine the field emission properties of the tube are the tip radius and the position of these occupied levels with respect to the Fermi level, which depends primarily on the tip geometry [131,150] (i.e., the tube chirality and diameter as well as the presence of defects). Indeed, only tubes with a band state just below or just above the Fermi level are good candidates for field emission. It is worth noting that the presence of such localized states greatly influences the emission behavior. At and above

room temperature, the body of the MWNTs behave essentially as graphitic cylinders. This means that the carrier density at the Fermi level is very low, i.e., on the order of $5 \times 10^{18} \text{ cm}^{-3}$, which is 3 orders of magnitude lower than for a metal. Simulations show that the local density of states at the tip [131] reaches values at least 30 times higher than in the cylindrical part of the tube. Therefore, the field emission current would be far lower without these localized states for a geometrically identical tip, since the emission depends directly on this carrier density. The tip structure also strongly influences the energy and intensity of the localized states, which could explain the superiority of closed, well-ordered tips relative to opened or disordered MWNTs (see Fig. 28). Another complementary explanation for this observation is that the coupling of the tip states to the metallic body states is probably far better for closed MWNTs, leading to an increased electron supply and thus to higher emitted currents.

6.2 Light emission coupled to electron emission

A rather unexpected behavior linked to the electron field emission was the observation of light emission as described above [147]. This light emission occurred in the visible part of the spectrum, and could sometimes even be seen with the naked eye. This light emission is not the luminescence due to resistive heating, which was observed by Rinzler et al. on opened nanotubes [144], and was attributed to an unraveling of carbon chains at the tip of the tube.

A typical experimental configuration for the electron/field emission is shown in Figs. 29(a) and (b). The optical luminescence was induced by the electron field emission, since it was not detected without an applied potential (and thus emitted current). Furthermore, the emitted light intensity followed closely the variations in emitted current, as can be seen in Fig. 29(c), where the emitted current and emitted light intensity were simultaneously measured [147].

The results in Fig. 29(c) demonstrate that the light emission is directly coupled to the field emission. The narrowness of the luminescence line (Fig. 30) and the very small shift of the photon energy of the luminescence peak as the emission current varies show that the luminescence is not coming from black-body radiation or from current-induced heating effects, but rather that the photons are emitted following transitions between well-defined energy levels. Actually, the dependence of luminescence intensity I_p on the emitted current I_e can be reproduced by a simple two-level model [147], where the density of states at the nanotube tip is simply represented by a two level system, with the dominant emission level at energy E_1 below or just above the Fermi energy, and a deep level at $E_2 < E_1$. When an electron is emitted from the deep E_2 level, it is replaced either by an electron from the tube body, or by an electron from level E_1 dropping down to fill the empty state at E_2 thereby provoking the emission of a photon. From the Fowler–Nordheim model, the

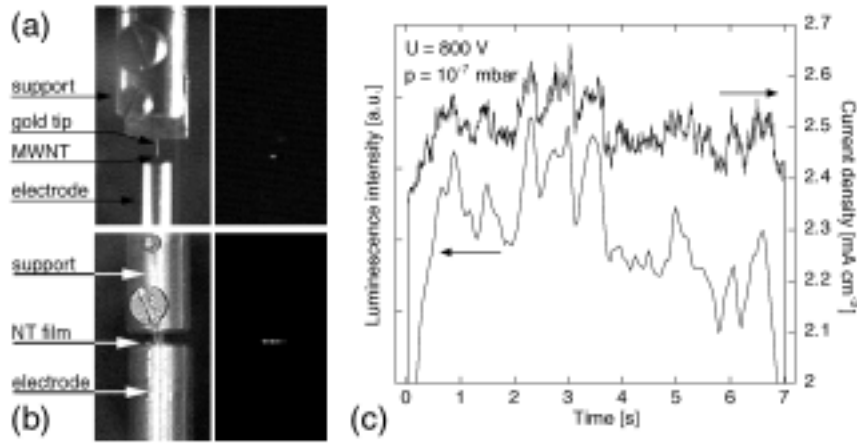


Fig. 29. Optical images of the experimental set-up for observing the field emission and the associated observed luminescence during field emission from an individual multiwall nanotube (a), and a multiwall carbon nanotube film (b). The simultaneously emitted light intensity and current density as a function of time for a MWNT film (c) [147]

transition probability $D(E)$ can be evaluated for each level, and in the framework of this two-level model, we can write $I_e \sim D(E_1)$, and $I_p \sim D(E_2)$. It appears that I_p varies as a power of I_e with an exponent that depends on the energy separation between the levels [151], and this exponent is ≈ 1.51 – 1.65 for the photon emission energies observed here (typically 1.8 eV, as seen in Fig. 30). This prediction regarding the dependence of I_p on I_e compares well with the experimental observations.

6.3 Light emission induced by STM

Another type of light emission was observed in MWNTs by Coratger et al. [152] who observed light emission by injecting electrons by Scanning Tunneling Microscopy (STM) into multiwall carbon nanotubes. The photon yield varied from tube to tube, but it was constant all along the tube. This is illustrated in Fig. 31, where a low resolution STM image shows a bundle of MWNTs, and while the STM topological image was taken, the photon map was recorded. The photon image shows that the emission yield depends probably on the diameter and chirality of the scanned tube, but not on the position of the STM tip along the tube. Simultaneous topographic STM images and photon spectroscopy scans show emitted photon wavelengths in the 600–1000 nm range (see Fig. 32), in good agreement with the field and light

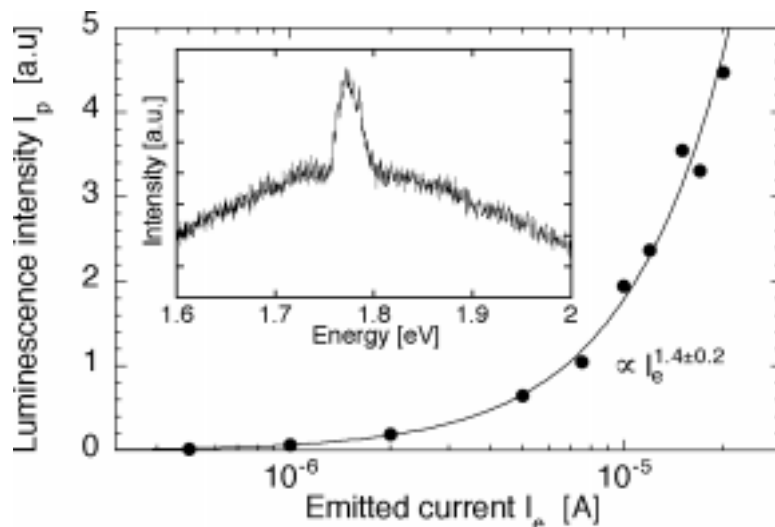


Fig. 30. Variation of the total emitted intensity as a function of emitted current. The solid line is a power law fit of the experimental data for I_p vs I_e on a semilog plot, which yields an exponent of $\alpha = 1.4 \pm 0.2$ for $I_p \sim I_e^\alpha$. Inset: Spectra of the field emission-induced luminescence for an individual MWNT at an emission current of 20 A [8]

emission data described above. The emission characteristics are independent of the substrate and of the material of the STM tip.

The STM induced-light emission in MWNTs could not be explained by models previously developed for light emission from metal and semiconductor surfaces, based on a radiative plasmon recombination mechanism, or from small fullerene molecules like C_{60} [53,153]. The origin of the experimental observation that the light wavelength and intensity are independent of the STM tip position might be explained as follows. It was suggested [152] that the large mean free path of the electrons injected into the MWNTs is associated with an efficient resonant coupling of the localized tip states to a continuum of states. The following scenario is proposed to explain this light emission behavior. Electrons are first injected into the extended states of the outer shell. Large numbers of these electrons flow towards the substrate, but a fraction of the electrons spreads all over the tube in a quasi-ballistic way, like in a large molecule. Some of these electrons are trapped for a short time in localized states at the nanotube tip, where they are resonantly coupled with extended states, and occasionally decay into a neighboring localized state situated approximately 2 eV below the Fermi energy by emitting a photon. The population difference between the two quasi-localized states comes from the V-shape band structure of the graphene layer so that states higher in energy are more populated than those situated near the Fermi energy. Indeed,

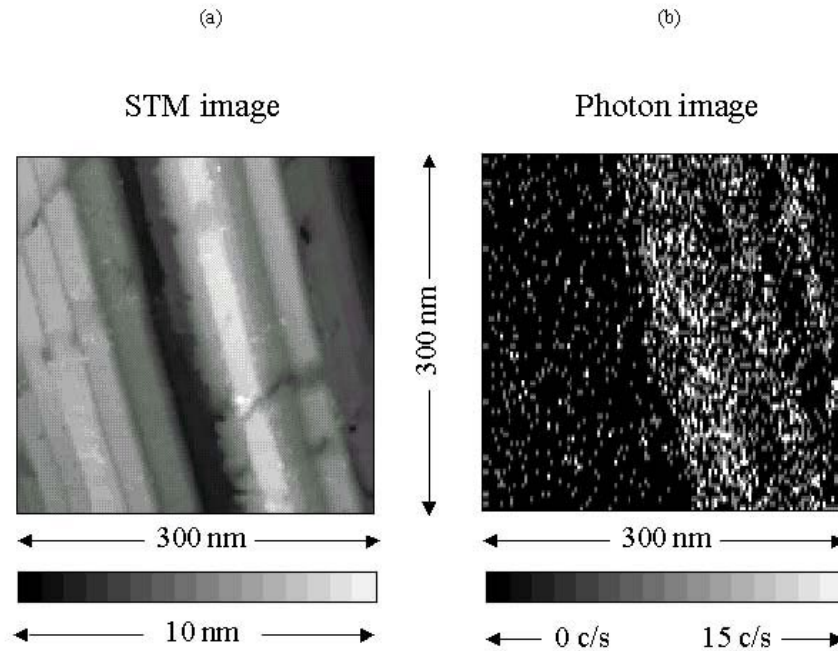


Fig. 31. (a) STM topography ($V_{\text{sample}}=2.1\text{ V}$, $I_t = 50\text{ nA}$) and (b) photon mapping of a MWNT bundle recorded simultaneously. Only three nanotubes in the MWNT bundle show significant light emission. The maximum rate of emitted photons is 15 counts per second per tube [152]

recent transport experiments show that the coherence length is exceptionally large in carbon nanotubes even at room temperature [154]. Differences in the emitted light characteristics probably reflect the large variety of possible geometric structures in the nanotube tip, and such experiments could perhaps offer a characteristic probe for the localized tip states in combination with Scanning Tunneling Spectroscopy.

7 Mechanical properties

It is becoming clear from recent experiments [154–161] that carbon nanotubes (CNTs) are fulfilling their promise to be the ultimate high strength fibers for use in materials applications. There are many outstanding problems to be overcome before composite materials, which exploit the exceptional

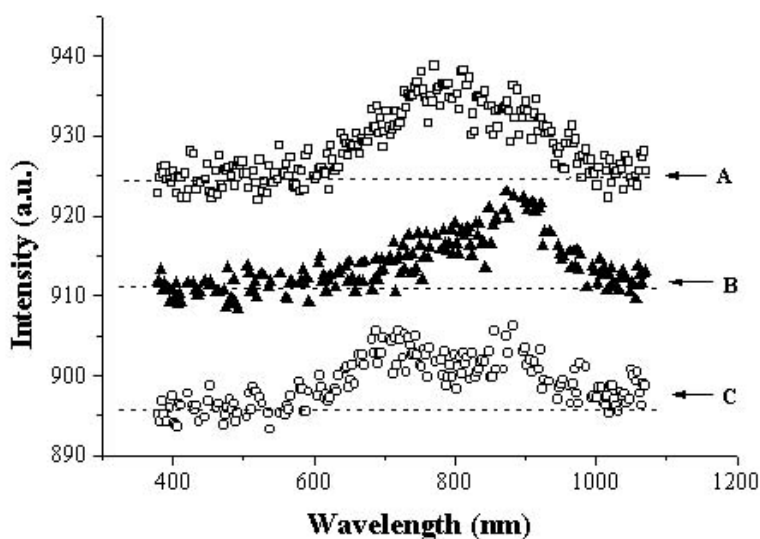


Fig. 32. Emission spectra of three different MWNTs acquired under similar experimental conditions. Dotted lines highlight position of the background. Spectrum A is one of the most recently observed and shows a peak at about 800 nm ($V_{\text{sample}}=2$ V, $I = 50$ nA). Spectra B and C were obtained on two different nanotubes with the same Pt-Ir tip during another experiment ($V_{\text{sample}}=2.05$ V, $I = 35$ nA). In spectrum B, a peak at 900 nm is found, while in spectrum C, another peak centered at about 710 nm is also revealed. For the three spectra, the exposure time is 5 minutes [152]

mechanical properties of the individual nanotubes, can be fabricated. Arc-discharge methods are unlikely to produce sufficient quantities of nanotubes for such applications. Therefore, catalytically grown tubes are preferred, but these generally contain more disorder in the graphene walls and consequently they have lower moduli than the arc-grown nanotubes. Catalytically grown nanotubes, however, have the advantage that the amount of disorder (and therefore their materials properties) can be controlled through the catalysis conditions, as mentioned before. As well as optimizing the materials properties of the individual tubes for any given application, the tubes must be bonded to a surrounding matrix in an efficient way to enable load transfer from the matrix to the tubes. In addition, efficient load bearing within the tubes themselves needs to be accomplished, since, for multi-walled nanotubes (MWNTs), experiments have indicated that only the outer graphitic shell can support stress when the tubes are dispersed in an epoxy matrix [162]. In this section, a few basic measurements are presented on individual MWNTs with different levels of disorder. The very promising SWNT ropes also present sev-

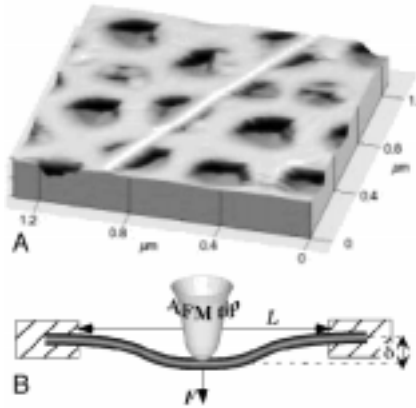


Fig. 33. (a) 3-D rendition of an AFM image of a SWNT bundle (or an individual MWNT) that adheres to an alumina ultra-filtration membrane, leading to a clamped beam configuration for mechanical testing. (b) Schematic representation of the measurement technique. The AFM applies a load, F , to the portion of nanotube with a suspended length of L and the maximum deflection δ at the center of the beam is directly measured from the topographic image, along with L and the diameter of the tube (measured as the height of the tube above the membrane) [158]

eral problems, which are reviewed by showing mechanical measurements on ropes of different diameter.

7.1 Young's modulus of MWNTs

The AFM technique for mechanical properties measurements developed by Salvétat and collaborators enabled characterization of the moduli of SWNT bundles [158] and MWNTs, both arc-grown and catalytically grown [159], to be carried out [158,159]. Briefly, the method involves depositing CNTs from a suspension in a liquid onto well-polished alumina ultra-filtration membranes with a pore size of about 200 nm (Whatman anodisc). By chance, CNTs occasionally span the pores and these can be subjected to mechanical testing on a nanometer length scale. The attractive interaction between the nanotube and the substrate acts to clamp the tubes to the substrate. Contact mode AFM measurements under ambient conditions are used to collect images of the suspended CNTs at various loading forces. Figure 33 shows an AFM image of a SWNT bundle suspended across a pore and a schematic representation of the mechanical test set-up. The maximum deflection of the CNT into the pore as a function of the loading force can be used to ascertain whether the behavior is elastic. If the expected linear behavior is observed, the Young's modulus (E) can be extracted using a continuum mechanics model for a clamped beam configuration. The suspended length of the CNT, its deflection as a function of load and its diameter can all be determined from the images, thereby enabling the modulus to be deduced. One great advantage of the AFM technique employed by Salvétat et al. [158] is its simplicity. There is no need, for example, to use complex lithographic techniques

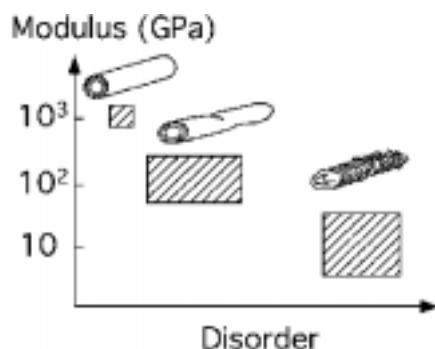


Fig. 34. Correlation between the measured Young's modulus of MWNTs with the amount of disorder present within the graphitic walls. Ranges of measured moduli for three different types of MWNTs are plotted against an arbitrary scale of increasing disorder. The sketch represents arc-discharge grown, and catalytically grown MWNTs at 720°C and at 900°C, respectively [163]

for suspending and the clamping tubes [156]. The surface forces between the CNTs and the alumina membrane are sufficiently high to maintain the clamped beam condition for the majority of MWNTs that were tested. In addition, the nanotubes are never exposed to electron radiation during the measurement, which would be the case for TEM studies [155,160]. Electron radiation will induce defects, if the energy of the electrons is high enough, and thereby alter the material properties of the CNTs. The relative ease of sample preparation for this AFM method enables a high measurement throughput, thereby allowing measurement of a variety of CNTs synthesized under different conditions and to compare the results systematically. For MWNTs grown by the arc-discharge method, it was found that the average value of the elastic modulus (or Young's modulus) E is 810 ± 410 GPa, which is consistent with the in-plane elastic constant of graphite, $c_{11} = 1.06$ TPa [15]. The authors did not find a significant correlation between the elastic modulus and the diameter of the tube [159]. Furthermore, no apparent difference was found in the elastic modulus between annealed and unannealed nanotubes. This suggests that point defects, if present at all, do not alter the mechanical properties of MWNTs.

7.2 Disorder effect

AFM measurements of the mechanical properties of arc-grown MWNTs and MWNTs catalytically grown at different temperatures have been compared, and the results show that the Young's modulus for the catalytically grown MWNTs are lower than for arc-grown MWNTs [7]. These data are summarized in Fig. 34, with a sketch correlating the elastic modulus with the amount of order/disorder within the nanotube walls. As one might expect, the Young's modulus of the MWNTs decreases as the disorder within the walls increases. Arc-grown MWNTs, which contain very few defects, have a modulus comparable with the high values that are measured for an individual SWNT [158]. The moduli of catalytic MWNTs can vary, depending

on their structure. Those, which have a highly defective kind of stacked coffee cup structure (see Fig. 5, part ii), have a very low modulus. The other catalytic MWNTs, grown at a lower temperature, showed a higher degree of order within the tubes and consequently had slightly higher moduli. The uncertainty of the measured values in this case was large. This could be due to greater uncertainties in the measurement technique, since the catalytic MWNTs were usually curved, making the continuum beam approximation less valid.

7.3 Comparison with SWNTs

Although the elastic moduli for single wall nanotube (SWNT) bundles (also known as ropes) were expected to be higher than for MWNTs, it has been demonstrated that shearing effects due to the weak intertube cohesion gives rise to significantly reduced moduli compared to individual SWNTs [158]. This is due to the fact that the SWNTs are held together in the rope by the same van der Waals forces that are acting between the 2D graphene layers, and these weak van der Waals forces make turbostratic graphite [16] a very good lubricant. The reduced bending modulus of these SWNT bundles is a function of the rope diameter because the magnitude of the shear modulus varies as the ratio of the length to the rope diameter. An individual SWNT

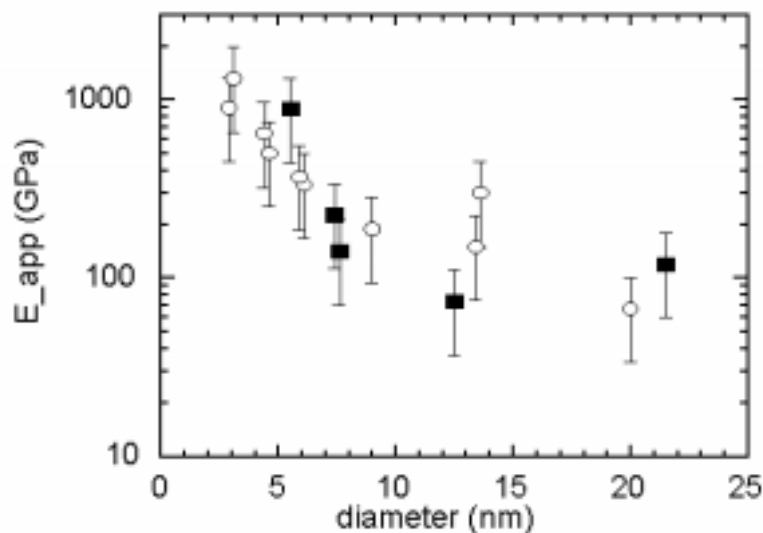


Fig. 35. Dependence of the apparent Young's modulus (E_{app}) on the diameter of SWNT bundles measured using AFM. The untreated bundles are represented by open circles and the irradiated bundles by filled squares. The diameter of the individual SWNTs is in the 1.4 nm range [163]

has an elastic modulus of about 1 TPa, but this falls to around 100 GPa for bundles 15 to 20 nm in diameter, as shown in Fig. 35.

In order to use nanotubes as a reinforcement in composites, there are two main challenges to address: (1) to establish strong bonding between the CNTs and the surrounding matrix, and (2) to create cross-links between the shells of MWNTs and also between the individual SWNTs in SWNT bundles, so that loads can be homogeneously distributed throughout the CNTs. To exploit the excellent mechanical properties of the individual SWNTs, both of these goals should be achieved without compromising the mechanical properties of the individual SWNTs too drastically. Efforts are in progress to address these problems using post production modification of CNTs via chemical means and controlled irradiation [7].

To produce cross-links between the shells in SWNTs of SWNT bundles, the sp^2 carbon bonding must be disrupted to sp^3 bonding, so that dangling bonds are available for cross-linking. Since the sp^2 bonding is the essence of the CNT strength, this must not be disrupted to such a degree that the properties of the individual SWNTs in SWNT bundles are degraded. A “gentle” way to produce cross-linking is by controlled electron irradiation. In Ref. [7] the SWNT bundles were exposed to 2.5 MeV electrons with a total radiation dose of 11 Curie/cm² after synthesis. A theoretical estimation of the number of displacements that this energetic electron dose produces suggests that the irradiation will create about 1 defect per 360 carbon atoms [164]. AFM measurements of the elastic modulus of irradiated SWNT bundles are shown in Fig. 35, along with similar measurements of non-irradiated SWNT bundles. Within the errors of the measurement technique, no increase in the elastic modulus of the bundles could be clearly identified. The Young’s modulus was still found to decrease with increasing bundle diameter in a similar way as that found for the non-irradiated bundles. However, the irradiation treatment does not appear to have compromised the strength of the individual SWNTs either, since the smaller diameter bundles have quite high elastic moduli. In addition, it was noticed that the irradiated bundles were more difficult to disperse in ethanol, and the morphology of the sample under AFM examination showed that the irradiated bundles exhibited a higher degree of aggregation. Taken together, these data suggest that the radiation treatment produced more bonding between the tubes, but this additional bonding was not sufficient to produce enough cross-links within the bundles to reduce shearing effects and produce bundles with higher Young’s moduli. Future efforts will concentrate on optimizing the chemistry and irradiation doses to improve the mechanical properties of SWNT bundles and MWNTs.

7.4 Deformation of MWNTs

There is some contention about whether the elastic modulus of MWNTs varies as a function of nanotube diameter. Poncharal et al. [160] have suggested the formation of a rippling mode on the surface of bent MWNTs with

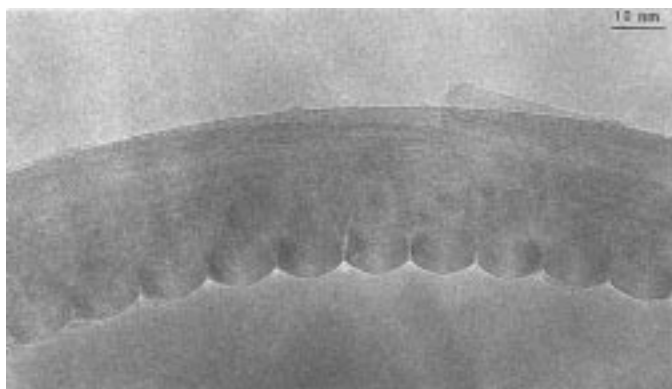


Fig. 36. High-resolution TEM image of a bent nanotube grown by the arc discharge method (radius of curvature 400 nm), showing the characteristic wave-like ripple distortion. The amplitude of the ripples increases continuously from the center of the tube to the outer layers of the inner arc of the bend [160]

diameters greater than about 15 nm, leading to a reduction in the measured modulus. However, a strong dependence of the measured modulus on the diameter was not observed in previous AFM measurements [159]. It is conceivable that the measurement of the modulus is force dependent and the transition to the rippling mode is not reached with the loading forces used in the AFM experiments. The TEM data in Fig. 36 obtained at large loading force show a rippling with a period of 15 nm on the compressed side of a statically bent MWNT, but the bent MWNTs in typical TEM experiments showing such phenomena have rather high curvatures [160] (much higher than typical curvatures seen in the AFM experiments). Interestingly, the rippling effect has also been observed on the compressed sides of catalytically grown MWNTs [7]. Figure 37 shows a high resolution AFM image of a catalytic MWNT (grown at 720°C) lying across a pore, the edge of which can be seen on the left of the image. The image clearly shows rippling only on the right-hand side of the tube, the direction in which the CNT is bent, and the ripple in this case has a period of roughly 16 nm. These ripples are not perpendicular to the tube axis but are inclined at approximately 30°, making the CNT left-handed. This rippling could arise from the surface forces, which constrain the CNTs on the membrane. However, rippling can also arise when the tubes are loaded in the AFM. Rippling on the upper, compressed side of these MWNTs has also been observed as the imaging force is increased. Non-linear behavior in the loading/unloading characteristics of the catalytic tubes was frequently noticed. This also contributes to the uncertainties in measuring moduli on these kinds of MWNTs by the AFM method. It is conceivable that the onset of rippling will occur at lower curvatures, i.e., lower forces, in tubes with a higher amount of disorder.

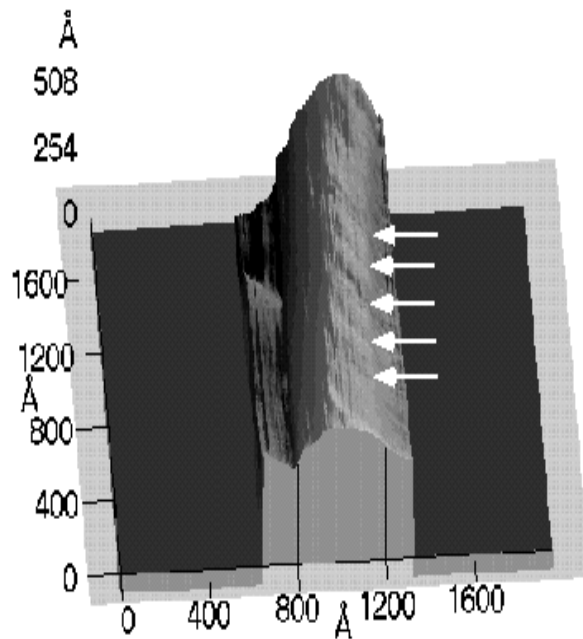


Fig. 37. 3-D rendering of a high resolution AFM image of a catalytic MWNT, grown at 720°C , and suspended on an alumina ultra-filtration membrane (the 0, 254, 508 Å refer to the z axis). Rippling is observed on the inner side of the natural curvature of the MWNT, with a periodicity of about 16 nm (shown by the white arrows), inclined at 30° to the tube axis [7]

Because of the Russian doll structure of the MWNTs and because of the high strength of the sp^2 bonds, one would think that a nanotube shell cannot be easily peeled off from a MWNT. However, it is quite possible that a single tube can be stripped off under axial stress. This has been observed in the experiments of Ruoff and coworkers [165] by fixing the ends of a MWNT to two AFM tips and measuring the elongation of the nanotube, while pulling until the tube broke. The tensile strength was found to be at least an order of magnitude lower than expected, assuming a homogeneous stress distribution over all carbon shells of the multiwall tube. But because the support only made contact to the outside of the MWNT, it is the outermost shell which is mainly stressed. Ruoff and coworkers [165] found that above the tensile limit, the outermost tubes rupture first, followed by a sudden and large elongation. From TEM images, these researchers conclude that the ruptured outer shell then slides over the inner tubes, which then in turn bear the load [16,37].

To conclude this section on the measurement of mechanical properties, it was demonstrated that the Young's modulus is very high for individual, and well graphitized carbon nanotubes. Their high strength makes them promis-

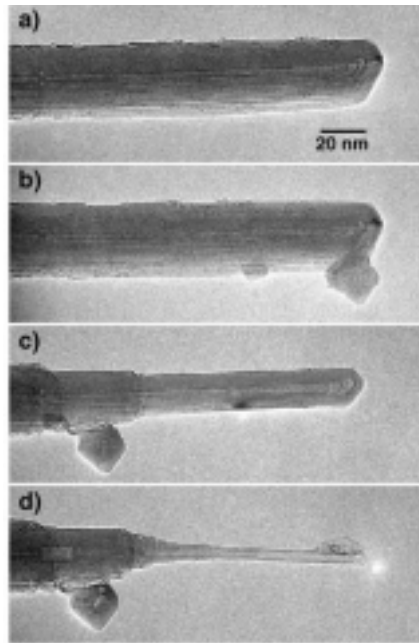


Fig. 38. Sequence of transmission electron microscope (TEM) images of a MWNT, showing the sharpening of the MWNT tip by applying current pulses with an STM tip [166]

ing candidates in reinforcement applications. There are many problems remaining to be overcome before composite materials can be fabricated, which reflect the exceptionally good mechanical properties of the individual nanotubes. As well as optimizing the material properties of the individual tubes, the tubes must be bonded to a surrounding matrix in an efficient way to enable load transfer from the matrix to the tubes. To improve their mechanical properties, the nanotube surfaces should be functionalized, and cross-linking should be generated between the SWNTs within and between the ropes.

8 Summary

In summary, we again emphasize the very rich physics encountered in the study of multiwalled carbon nanotubes. In this chapter we gave, at best, a snap-shot of the present status of this rapidly changing field. As an illustration of the enormous potential of the multiwalled carbon nanotubes in basic and applied science, we present the manipulation of MWNTs of the Zettl group at Berkeley [166] of which we have become aware during the writing of this chapter. Describing their breakthrough, best summarizes the rapid progress of this field. They managed to peel a MWNT and to sharpen its tip at ‘will’ by using Joule heating applied via an STM tip in a transmission electron microscope (Fig. 38). The outer, supporting shortened cylinders reinforce the stability of the nanotube. This gives the possibility to improve considerably

the resolution of a scanning probe tip. By attaching the STM tip to the innermost nanotube when the outer layers were peeled off, they have created an extremely low-friction nanoscale linear bearing and a constant force nanospring. We believe that in the future such manipulations of MWNTs will revolutionize nanoscale architectures and studies at the nanoscale.

Acknowledgements

The authors acknowledge the contributions to the work presented here by all their past and present collaborators, especially J.-M. Bonard, J.-P. Salvetat, K. Hernadi, S. Pekker, Walt A. de Heer, D. Ugarte, A. Bachtold, and M. Buitelaar. The work in Lausanne and Basel is supported by the Swiss National Science Foundation Program NFP36.

References

1. S. Iijima, *Nature* **354**, 56 (1991).
2. D. S. Bethune, C. H. Kiang, M. S. de Vries, G. Gorman, R. Savoy, J. Vazquez and R. Beyers, *Nature* **363**, 605 (1993).
3. S. Iijima and T. Ichihashi, *Nature* **363**, 603 (1993).
4. A. Thess, R. Lee, P. Nikolaev, H. Dai, P. Petit, J. Robert, C. Xu, Y. H. Lee, S. G. Kim, A. G. Rinzler, D. T. Colbert, G. E. Scuseria, D. Tománek, J. E. Fischer, and R. E. Smalley, *Science* **273**, 483 (1996).
5. W. Krätschmer, L. D. Lamb, K. Foristopoulos and D. R. Huffman, *Nature* **347**, 354 (1990).
6. T. W. Ebbesen and P. M. Ajayan, *Nature* **358**, 220 (1992).
7. L. Forró, J.-P. Salvetat, J.-M. Bonard, R. Bacsá, N. H. Thomson, S. Garaj, L. Thien-Nga, R. Gaál, A. J. Kulik, B. Ruzicka, L. Degiorgi, A. Bachtold, C. Schönenberger, S. Pekker, and K. Hernadi, in *Science and Application of Nanotubes*, edited by D. Tománek and R. J. Enbody, Kluwer Academic/Plenum Publishers, 1999, p. 297.
8. J.-M. Bonard, T. Stora, J.-P. Salvetat, F. Meier, T. Stöckli, C. Düscher, L. Forró, W. A. de Heer, and A. Chatelain, *Advanced Mater.* **9**, 827 (1997).
9. W. Bacsá, unpublished.
10. C. S. Tsang, Y. K. Chen, P. J. F. Harris and M. L. Green, *Nature* **372**, 159 (1994).
11. H. Hiura, T. W. Ebbesen and K. Tanigaki, *Adv. Mater.* **7**, 275 (1995).
12. C. Journet and P. Bernier, *Applied Physics A* **67**, 1 (1998).
13. A. Fonseca, K. Hernadi, P. Piedigrosso, J.-F. Colomer, K. Mukhopadhyay, R. Doome, S. Lazarescu, L. P. Biro, P. Lambin, P. A. Thiry, D. Bernaerts, and J. B. Nagy, *Applied Physics A* **67**, 11 (1998).
14. M. Endo, K. Takeuchi, K. Kobori, K. Takahashi, H. Kroto, and A. Sarkar, *Carbon* **33**, 873 (1995).
15. M. S. Dresselhaus, G. Dresselhaus, K. Sugihara, I. L. Spain, and H. A. Goldberg, in *Graphite Fibers and Filaments*. Springer Series in Materials Science, volume **5** (1988).
16. M. S. Dresselhaus and M. Endo, chapter of this volume.

17. X. B. Zhang, X. F. Zhang, D. Bernaerts, G. Van Tendeloo, S. Amelinckx, J. Van Landuyt, V. Ivanov, J. B. Nagy, Ph. Lambin and A. A. Lucas, *Europhysics Letters* **27**, 141 (1994).
18. V. Ivanov, J. B. Nagy, Ph. Lambin, A. A. Lucas, X. B. Zhang, X. F. Zhang, D. Bernaerts, G. Van Tendeloo, S. Amelinckx and J. Van Landuyt, *J. Chemical Physics Letters* **223**, 329 (1994).
19. A. Fonseca, K. Hernadi, J. B. Nagy, P. Lambin, and A. Lucas, *Synth. Met.* **77**, 235 (1996).
20. N. Demoncy, O. Stephan, N. Brun, C. Colliex, A. Loiseau, and H. Pascard, *Synthetic Metals* **103**, 2380 (1999).
21. S. Amelinckx, D. Bernaerts, G. van Tendeloo, J. van Landuyt, A. A. Lucas, M. Mathot, P. Lambin, in *Physics and Chemistry of Fullerenes and Derivatives*, Proceedings of the International Winterschool on Electronic Properties of Novel Materials, Kirchberg 1995, ed. by H. Kuzmany, J. Fink, M. Mehring, and S. Roth, (World Scientific) p. 515.
22. S. Amelinckx, D. Bernaerts, X. B. Zhang, G. Van Tendeloo and J. Van Landuyt, *Science* **267**, 1334-8 (1995).
23. H. Kind, J.-M. Bonard, C. Emmenegger, L.-O. Nilsson, K. Hernadi, E. Maillard-Schaller, L. Schlapbach, L. Forró and K. Kern, *Adv. Mater.* **11**, 1285 (1999).
24. N. Yao, V. Lordi, S. X. C. Ma, E. Dujardin, A. Krishnan, M. M. J. Treacy and T. W. Ebbesen, *J. Mater. Res.* **13**, 2432-2437 (1998).
25. J.-M. Bonard, J.-P. Salvetat, T. Stöckli, L. Forró, and A. Chatelain, *Applied Physics. A* **69**, 245 (1999).
26. M.S. Dresselhaus, G. Dresselhaus, R. Saito, *Phys. Rev. B* **45**, 6234 (1992).
27. M.S. Dresselhaus, G. Dresselhaus, R. Saito, *Carbon* **33**, 883 (1995).
28. S. Louie, chapter in this volume.
29. M. S. Dresselhaus and Ph. Avouris, chapter in this volume.
30. N. B. Brandt, and Y. G. Chudinov, *Graphite and its compounds* (North-Holland, Amsterdam-Oxford-New York-Tokyo, 1988).
31. H. W. Kroto, J. R. Heath, S. C. O'Brien, R. F. Curl and R. E. Smalley, *Nature* **318**, 162 (1985).
32. S. Iijima, *Solid State Physics* **27**, 39-45 (1992).
33. V. H. Crespi, N. G. Chopra, M. L. Cohen, A. Zettl, and S. G. Louie, *Phys. Rev. B* **54**, 5927.
34. K. L. Lu, R. M. Lago, Y. K. Chen, M. L. H. Green, P. J. F. Harris and S. C. Tsang, *Carbon* **34**, 814 (1996).
35. J. Liu, A. G. Rinzler, H. Dai, J. H. Hafner, R. K. Bradley, P. J. Boul, A. Lu, T. Iverson, K. Shelimov, C. B. Huffman, F. Rodriguex-Macia, D. T. Colbert and R. E. Smalley, *Science* **280**, 1253-1256. (1998).
36. C. Guerret-Plecourt, Y. Le Bouar, A. Loiseau, and H. Pascard, *Nature* **372**, 761 (1994).
37. P. Ajayan and O. Zhou, chapter in this volume.
38. A. Loiseau, N. Demoncy, O. Stéphan, C. Colliex and H. Pascard, page 1-16, in D. Tománek and R. J. Enbody, *Kluwer Academic/Plenum Publishers*, 1999, (Book on Conference Proceedings).
39. P. M. Ajayan, T. W. Ebbesen, T. Ichihashi, S. Iijima, K. Tanigaki and H. Hiura, *Nature* **362**, 522 (1993).
40. S. C. Tsang, P. J. F. Harris, and M. L. H. Green, *Nature*, **362**, 520 (1993).

41. E. Djuradin, T. W. Ebbesen, H. Hiura and K. Tanigaki, *Science* **265**, 1850 (1994).
42. Y. K. Chen, M. L. H. Green and S. C. Tsang, *Chem. Commun.* 2489 (1996).
43. D. Ugarte, A. Chatelain, and W. A. de Heer, *Science* **274**, 1897 (1996).
44. C. Schöenberger, A. Bachtold, C. Strunk, J.-P. Salvetat, and L. Forró, *Appl. Phys. A* **69** 283 (1999).
45. S. Frank, P. Poncharal, Z. L. Wang, and W. A. de Heer, *Science* **280**, 1744 (1998).
46. A. Bachtold, C. Strunk, J. P. Salvetat, J. M. Bonard, L. Forró, T. Nussbaumer and C. Schöenberger, *Nature* **397**, 673 (1999).
47. R. Saito, G. Dresselhaus, and M. S. Dresselhaus, *Physical Properties of Carbon Nanotubes* (Imperial College Press, London, 1998).
48. Cees Dekker, *Physics Today*, May issue, **52**, 22-28 (1999).
49. J. W. Mintmire, B. I. Dunlap, and C. T. White, *Phys. Rev. Lett.* **68**, 631-634 (1992).
50. T. Hamada, M. Furuyama, T. Tomioka, and M. Endo, *J. Mater. Res.* **7**, 1178-1188 (1992). *ibid.*, 2612-2620.
51. R. Saito, M. Fujita, G. Dresselhaus and M. S. Dresselhaus, *Appl. Phys. Lett.* **60**, 2204 (1992).
52. R. Saito, G. Dresselhaus, and M. S. Dresselhaus, *J. Appl. Phys.* **73**, 494 (1993).
53. M. S. Dresselhaus, G. Dresselhaus and P. C. Eklund, *Science of Fullerenes and Carbon Nanotubes*; Academic Press: New York, 1996.
54. P. R. Wallace, *Phys. Rev.* **71**, 622 (1947).
55. R. Saito and H. Kataura, chapter of this volume.
56. R. Saito, G. Dresselhaus, and M. S. Dresselhaus, *Phys. Rev. B* **61**, 2981 (2000).
57. G. S. Painter and D. E. Ellis, *Phys. Rev. B* **1**, 4747 (1970).
58. D. P. DiVincenzo and E. J. Mele, *Phys. Rev.* **29** 1685 (1984).
59. J. W. Mintmire, D. H. Robertson, and C. T. White, *J. Phys. Chem. Solids* **54**, 1835 (1993).
60. R. Bacon, *J. Appl. Phys.* **31**, 283-290 (1960).
61. L. Piraux, *J. Mat. Res.* **5**, 1285 (1990).
62. H. Ajiki and T. Ando, *J. Phys. Soc. Jpn.* **62**, 2470-2480 (1993). Erratum: *ibid* page 4267.
63. J. W. G. Wildöer, L. C. Venema, A. G. Rinzler, R. E. Smalley, and C. Dekker, *Nature (London)* **391**, 59-62 (1998).
64. T. W. Odom, J. L. Huang, P. Kim, and C. M. Lieber, *Nature (London)* **391**, 62-64 (1998).
65. Young-Kyun Kwon and David Tománek, *Phys. Rev. B* **58**, R16001 (1998).
66. Ph. Lambin, V. Meunier, and A. Rubio, in *Science and Application of Nanotubes*, edited by D. Tománek and R.J. Enbody, Kluwer Academic/Plenum Publishers, 1999, p. 17.
67. C.-H. Kiang, M. Endo, P. M. Ajayan, G. Dresselhaus and M. S. Dresselhaus, *Phys. Rev. Lett.* **81**, 1869 (1998).
68. S. N. Song, X. K. Wang, R. P. H. Chang, and J. B. Ketterson, *Phys. Rev. Lett.* **72**, 697 (1994).
69. L. Langer, V. Bayot, E. Grivei, J. P. Issi, J. P. Heremans, C. H. Olk, L. Stockman, C. Van Haesendonck and Y. Bruynseraede, *Phys. Rev. Lett.* **76**, 479 (1996).
70. G. Bergmann, *Phys. Rep.* **107**, 1 (1984).

71. B. L. Altshuler, A. G. Aharonov, M. E. Gershenson, and Y. V. Sharvin, in *Soviet Scientific Reviews, Section A: Physics Reviews*, I. M. Khalatnikov ed. (Harwood Academic, New York, 1987).
72. B. L. Altshuler and P. A. Lee, *Physics Today*, Dec. issue, p36 (1988).
73. A. Aharonov, *Physica Scripta* **T49**, 28 (1993).
74. S. J. Tans, M. H. Devoret, H. Dai, A. Thess, R. E. Smalley, L. J. Geerligs and C. Dekker, *Nature* **386**, 474 (1997).
75. M. Bockrath, D. H. Cobden, P. L. McEuen, N. G. Chopra, A. Zettl, A. Thess and R. E. Smalley, *Science* **275**, 1922 (1997).
76. A. Bachtold, C. Strunk, C. Schönenberger, J. P. Salvetat, and L. Forró, *Proceedings of the XIIth International Winterschool on Electronic Properties of Novel Materials* edited by H. Kuzmany, J. Fink, M. Mehring, and S. Roth, 65 (AIP New-York 1998).
77. A. Yu. Kasumov, R. Deblock, M. Kociak, B. Reulet, H. Bouchiat, I. I. Khodos, Yu. B. Gorbatov, V. T. Volkov, C. Journet, and M. Burghard, *Science* **284**, 1508 (1999).
78. K. Tsukagoshi, B. W. Alphenaar and H. Ago, *Nature* **401**, 572 (1999).
79. H. Dai, E. W. Wong, and C. M. Lieber, *Science* **272**, 523–526 (1994).
80. A. Thess, R. Lee, P. Nikolaev, H. Dai, P. Petit, J. Robert, C. Xu, Y. H. Lee, S. G. Kim, A. G. Rinzler, D. T. Colbert, G. E. Scuseria, D. Tománek, J. E. Fischer, and R. E. Smalley, *Science* **273**, 483–487 (1996).
81. A. Yu. Kasumov, H. Bouchiat, B. Reulet, O. Stephan, I. I. Khodos, Yu. B. Gorbatov, and C. Colliex, *Europhys. Lett.* **43**, 89 (1998).
82. P. J. de Pablo, E. Graugnard, B. Walsh, R. P. Andres, S. Datta, and R. Reifengerger, *Appl. Phys. Lett.* **74**, 323 (1999).
83. P. J. de Pablo, S. Howell, S. Crittenden, B. Walsh, E. Graugnard, and R. Reifengerger, *Appl. Phys. Lett.* **75**, 3941 (1999).
84. H. R. Shea, R. Martel, T. Hertel, T. Schmidt, and Ph. Avouris, *Microel.-Eng.*, **46**, 101 (1999).
85. J. Kong, H. T. Soh, A. M. Cassell, C. F. Quate, and H. Dai, *Nature* **395**, 878 (1998).
86. G. Baumgartner, M. Carrard, L. Zuppiroli, W. Basca, W. A. de Heer, and L. Forró, *Phys. Rev. B* **55**, 6704 (1997).
87. J. Hone, I. Ellwood, M. Muno, Ari Mizel, Marvin L. Cohen, A. Zettl, Andrew G. Rinzler, and R. E. Smalley, *Phys. Rev. Lett.* **80**, 1042 (1998).
88. W. Yi, L. Lu, Zhang Dian-lin, Z. W. Pan, and S. S. Xie, *Phys. Rev. B Rapid Comm.* **59**, R9015 (1999).
89. L. Grigorian, G. U. Sumanasekera, A. L. Loper, S. Fang, J. L. Allen and P. C. Eklund, *Phys. Rev. B* **59**, R11309 (1999).
90. P. G. Collins, K. Bradley, M. Ishigami, and A. Zettl, *Science* **287**, 1801 (2000).
91. G. U. Sumanasekera, C. Adu, S. Fang, and P. C. Eklund, *Phys. Rev. Lett.* (2000). submitted.
92. Li Lu, Wie Yi, Z. Pan, and S. S. Xie, *Bulletin of the APS* March **45**, 414 (2000).
93. T. W. Ebbesen, H. Hiura, M. E. Bisher, M. M. J. Treacy, J. L. Shreeve-Keyer, and R. C. Haushalter, *Advanced Materials* **8**, 155 (1996).
94. Adrian Bachtold, PhD thesis, Univ. of Basel (1999).
95. A. Bachtold, M. Henny, C. Terrier, C. Strunk, C. Schönenberger, J.-P. Salvetat, J.-M. Bonard, and L. Forró, *Appl. Phys. Lett.* **73**, 274 (1998).

96. Y. Imry 'Physics of mesoscopic systems' in *Directions in Condensed Matter Physics*, G. Grinstein and G. Mazenko, eds. (World Scientific Press, Singapore, 1986).
97. A. Bachtold, C. Terrier, M. Kruger, M. Henny, T. Hoss, C. Strunk, R. Huber, H. Birk, U. Stauffer, and C. Schönenberger, *Microelectronic engineering* **41-42**, 571 (1998).
98. M. Buitelaar, A. Bachtold, C. Schönenberger, and L. Forró, unpublished.
99. H. Grabert and M. H. Devoret *Single Charge Tunneling: Coulomb Blockade Phenomena in Nanostructures* (Plenum Press, New York, 1992).
100. B. L. Altshuler, *Pis'ma Zh. Eksp. Teor. Fiz.* **41**, 530 (1985) [*JETP Lett.* **41**, 648 (1985)].
101. P. A. Lee and A. D. Stone, *Phys. Rev. Lett.* **55**, 1622 (1985).
102. P. A. Lee, A. D. Stone, and H. Fukuyama, *Phys. Rev. B* **35**, 1039 (1987).
103. P. Delaney, M. Di Ventra, and S. T. Pantelides, *Appl. Phys. Lett.* **75**, 3787 (1999).
104. Walt de Heer et al., unpublished.
105. Z. Yao, C. L. Kane, and C. Dekker, *Phys. Rev. Lett.* **84**, 2941 (2000).
106. W. Tian and S. Datta, *Phys. Rev. B* **49**, 5097 (1994).
107. A. G. Aharonov and Yu. V. Sharvin, *Rev. Mod. Phys.* **59**, 755 (1987).
108. B. L. Altshuler, A. G. Aharonov, and B. Z. Spivak, *Pis'ma Zh. Eksp. Teor. Fiz.* **33**, 101 (1981) [*JETP Lett.* **33**, 94 (1981)].
109. M. Baxendale, V. Z. Mordkovich, S. Yoshimura, and R. P. H. Chang, *Phys. Rev. B* **56**, 2161 (1997).
110. A. Fujiwara et al., *Proceedings of the International Winterschool on Electronic Properties of Novel Materials 1997* edited by H. Kuzmany, J. Fink, M. Mehring, and S. Roth, 65 (AIP New-York 1997).
111. G. T. Kim, E. S. Choi, D. C. Kim, D. S. Suh, Y. W. Park, K. Liu, G. Duesberg, and S. Roth, *Phys. Rev. B* **58**, 16064 (1998).
112. B. L. Altshuler, A. G. Aharonov, and D. E. Khmel'nitsky, *Solid State Commun.* **39**, 619 (1981).
113. P. A. Lee and T. V. Ramakrishnan, *Rev. Mod. Phys.* **57**, 287 (1985).
114. B. L. Altshuler and A. G. Aharonov, in *Electron-Electron Interactions in Disordered Systems*, M. Pollak and A. L. Efros, eds., p 1-153, (North-Holland, Amsterdam, 1984).
115. H. Fukuyama, in *Electron-Electron Interactions in Disordered Systems*, M. Pollak and A. L. Efros, eds., p 155-230, (North-Holland, Amsterdam, 1984).
116. R. Egger and A. O. Gogolin, *Phys. Rev. Lett.* **79**, 5082 (1997).
117. C. Kane, L. Balents, and M. P. A. Fisher, *Phys. Rev. Lett.* **79**, 5086 (1997).
118. A. Komnik and R. Egger, *Phys. Rev. Lett.* **80**, 2881 (1998).
119. A. A. Odintsov and H. Yoshioka, *Phys. Rev. Lett.* **82**, 374 (1999).
120. R. Egger and A. O. Gogolin, *Eur. Phys. J. B* **3**, 281 (1998).
121. R. Egger, *Phys. Rev. Lett.* **83**, 5547 (1999).
122. C. T. White and J. W. Mintmire, *Nature* **394**, 29 (1998).
123. J. W. Mintmire and C. T. White, *Phys. Rev. Lett.* **81**, 2506 (1998).
124. A. Bachtold, C. Schönenberger and L. Forró, unpublished.
125. M. Bockrath, D. H. Cobden, J. Lu, A. G. Rinzler, R. E. Smalley, L. Balents, and P. L. McEuen, *Nature* **397**, 598 (1999).
126. For a review see: M. P. A. Fisher and L. Glazman, in *Mesoscopic Electron Transport*, L. L. Sohn, L. P. Kouwenhoven, and G. Schön, eds., NATO ASI Series E: Applied Sciences **345** (Kluwer Academic, Dordrecht 1997).

127. Z. Yao, H. W. Ch. Postma, L. Balents, and C. Dekker, *Nature* **402**, 273 (1999).
128. Adrian Bachtold, private communication.
129. E. Graugnard, B. Walsh, P. J. de Pablo, R. P. Andres, S. Datta, and R. Reifenberger, *Bulletin of the APS March* **45** 487 (2000).
130. D. Tománek and R.J. Enbody, Kluwer Academic/Plenum Publishers, 1999, (Book on Conference Proceedings).
131. D. L. Carroll, P. Redlich, P. M. Ajayan, J.-C. Charlier, X. Blase, A. De Vita, and R. Car, *Phys. Rev. Lett.* **78**, 2811 (1997).
132. M. Kociak, A. Yu Kasumov, S. Gu'eron, B. Reulet, L. Vaccarini, I. I. Khodos, Yu, B. Gorbatov, V. T. Volkov, and H. Bouchiat, unpublished.
133. G. Wagoner, *Phys. Rev.* **118**, 647 (1960).
134. Y. Yafet, *Solid State Phys.* **14**, 1 (1963).
135. R. J. Elliott, *Phys. Rev.* **96**, 266 (1954).
136. O. Chauvet, L. Forró, W. Bacsa, D Chatelain, D. Ugarte and W. De Heer, *Phys. Rev. B* **52**, R6963 (1995).
137. F. Beuneu, and P. Monod, *Phys. Rev. B* **18**, 2422 (1978).
138. Y. Tomkiewicz, E.M. Engler and T.D. Schultz, *Phys. Rev. Lett.* **35**, 456 (1975).
139. A. N. Bloch, T. F. Carruthers, T. O. Poehler and D. O. Cowan, in *Chemistry and Physics of One-Dimensional Metals*, edited by Keller H. J. (Plenum, New York, 1977) p.47.
140. L. Forró, J. R. Cooper, G. Sekretarczyk, M. Krupski and K. Kamarás, *J. Physique* **48**, 413 (1987).
141. J.-P. Salvetat, J.-M. Bonard, L. Forró, unpublished.
142. L.S. Singer and G. Wagoner, *J. Chem. Phys.* **37**, 1812 (1962).
143. G. Baumgartner, M. Carrard, L. Zuppiroli, W. Bacsa, W.A. de Heer and L. Forró, *Phys. Rev. B* **55** , 6704 (1997).
144. A. G. Rinzler, J. H. Hafner, P. Nikolaev L. Lou, S. G. Kim, D. Tománek, P. Nordlander, D. T. Colbert and R. E. Smalley, *Science* **269**, 1550 (1995).
145. W. A. de Heer, A. Chatelain and D. Ugarte, *Science* **270**, 1179 (1995).
146. W. A. de Heer, J.-M. Bonard, Kai Fauth, A. Chatelain, L. Forró, D. Ugarte, *Advanced Materials* **9**, 87-9 (1997).
147. J.-M. Bonard, T. Stöckli, F. Meier, W. A. de Heer, A. Chatelain, J.-P. Salvetat, and L. Forró, *Phys. Rev. Lett.* **81**, 1441 (1998).
148. J.-M. Bonard, F. Meier, T. Stöckli, L. Forró, A. Chatelain, W. de Heer, J.-P. Salvetat, and L. Forró, *Ultramicroscopy* **77**, 7 (1998).
149. P. Kim, T. W. Odom, J.-L. Huang, and C. M. Lieber, *Phys. Rev. Lett.* **82**, 1225 (1999).
150. A. De Vita, J.-C. Charlier, X. Blase, and R. Car: *Appl. Phys. A.* **68**, 283 (1999).
151. M. Fransen: Towards high brightness, monochromatic electron sources, PhD thesis, Technical University Delft (1999).
152. R. Coratger et al, preprint.
153. R. Berndt, R. Gaisch, J. K. Gimzewski, B. Reihl, R. R. Schittler, W. D. Schneider, and M. Tschudy, *Science* **262**, 1425 (1993).
154. S. Frank, P. Poncharal, Z. L. Wang, and W. A. de Heer, *Science* **280**, 1744 (1998).
155. M. M. J. Treacy, T. W. Ebbesen and J. M. Gibson, *Nature* **381**, 678 (1996).
156. E.W. Wong, P.E. Sheehan and C.M. Lieber. *Science* **277**, 1971 (1997).

157. A. Krishnan, E. Dujardin, T.W. Ebbesen, P.N. Yianilos and M.M.J. Treacy, *Phys. Rev. B* **58** (20) 14013 (1998).
158. J.-P. Salvetat, G.A.D. Briggs, J.-M. Bonard, R. R. Basca, A.J. Kulik, T. Stöckli, N.A. Burnham and L. Forró, *Phys. Rev. Lett.* **82** 944 (1999).
159. J.-P. Salvetat, A. J. Kulik, J.-M. Bonard, G. A. D. Briggs, T. Stöckli, K. Méténier, S. Bonnamy, F. Béguin, N. A. Burnham and L. Forró, *Adv. Mater.* **11** (2) 161 (1999).
160. P. Poncharal, Z. L. Wang, D. Ugarte and W. A. de Heer, *Science* **283**, 1513 (1999).
161. D. A. Walters, L. M. Ericson, M. J. Casavant, J. Liu, D. T. Colbert, K. A. Smith and R. E. Smalley, *Appl. Phys. Lett.* **74**, 3803 (1999).
162. L. S. Schadler, S. C. Giannaris and P. M. Ajayan, *Appl. Phys. Lett.* **73**, 3842 (1998).
163. J.-P. Salvetat, J.-M. Bonard, N. H. Thomson, A. J. Kulik, L. Forró, W. Benoit, and L. Zuppiroli, *Applied Physics A* **69**, 255 (1999).
164. F. Beuneu, C. L'Huillier, J.-P. Salvetat, J.-M. Bonnard and L. Forró, *Phys. Rev. B* **59**, 5945 (1999).
165. Min-Feng Yu, O. Lourie, M. J. Dyer, K. Moloni, T. F. Kelly and R. S. Ruoff, *Science* **287**, 637 (2000).
166. J. Cumings and A. Zettl, unpublished.

Index

- abstract, 29, 131, 133, 212
- acceptor doping
 - boron, 112
- acoustic phonon modes, 148, 205, 210, 255
- adsorption
 - gas
 - hydrogen, 296
- Aharonov–Bohm
 - effect, 215, 223, 232, 250
 - flux, 232
 - period, 244
 - phase, 243
- Al₂O₃, 71
- Al₂O₃
 - whiskers, 22
- aligned single wall carbon nanotubes, 3
- aligned tubes
 - bundles, 154
 - MWNT films, 287
 - MWNTs, 287
 - SWNT bundles, 302
- angle resolved photoemission spectroscopy (ARPES)
 - ARPES, 173
- angle resolved photoemission spectrum
 - graphite, 176
- anti-Stokes Raman , 158
 - , 158
 - spectra, 158–160, 166
- applications
 - conductors (1D), 256
 - actuator
 - electromechanical, 307
 - actuators, 307
 - battery, 26, 296, 310
 - biological, 306
 - carbon fiber, 22, 313
 - catalysis, 71, 310
 - chemistry, 306
 - commercial, 312
 - composites, 285, 286, 298, 301
 - CVD fiber, 22
 - display, 289
 - electrochemical, 292
 - electron emission, 260
 - electronic, 8, 312
 - electronic device, 283, 310, 311
 - electronic devices, 94, 285
 - EMI shielding, 303
 - energy storage, 296
 - field emission, 215, 260, 286
 - graphite, 17
 - hydrogen storage, 285, 297
 - inorganic fullerenes, 87
 - intercalated nanotubes, 26
 - light emission, 214, 260
 - lithographic techniques, 8
 - lubrication, 88
 - materials science, 286
 - mechanical, 266, 301
 - mechanical reinforcement, 274
 - medical, 305
 - medical catheter, 307
 - microelectronics, 87
 - microprobe tips, 94
 - microwave amplifiers, 289
 - nano-lithography, 305
 - nano-technology, 307
 - nanolithography, 88
 - nanoprobe, 299
 - nanotube , 311
 - nanotubes, 3, 9, 282
 - optical, 303
 - opto-electronic, 84
 - PAN fiber, 22
 - photo-voltaic, 303
 - photocatalysis, 89
 - reinforcement, 62, 311
 - scanning probe tip, 215
 - scanning probe tips, 62, 69
 - sensors, 307
 - structural, 298
 - surface properties, 283
 - thin-screen technology, 217
 - tribological, 89
 - vacuum electronics, 286
 - vapor phase growth, 217

- arc discharge, 17, 18
- arc method, 150
- arc-discharge
 - growth, 220, 222, 224, 227, 253, 269
 - method, 260, 267
- ARIPES, 173
- armchair
 - (n, n) tubes, 96
- armchair nanotubes, 4–6, 137, 189
- asymmetric-digital-signal-line (ADSL)
 - telecom network, 292
- atomic force microscope (AFM), 120
- atomic force microscope (AFM)
 - experiments, 272
 - image, 118, 268, 270, 272, 273
 - instruments, 306
 - measurements, 268, 269, 271, 272
 - method, 269, 272
 - nano-lithography, 306
 - technique, 268
 - tip, 285, 305, 306, 312, 313
 - tips, 273
- Auger peak
 - OKLL, 181
- $B_xC_yN_z$, 73, 89
- ball-milling, 294
- bamboo structure, 66, 219, 220, 222
- band
 - gap, 17, 21
 - overlap, 16, 21
- band structure
 - electron, 173, 175, 177, 178, 183, 193
 - graphene, 194
 - graphite, 176
- band-folding, 96, 98, 104
- BC_2N , 64, 73, 75, 78
- BC_3 , 64, 75
- Bernal stacking, 15, 16
- BET characterization, 294
- black body, 152
- BN, 60, 62, 64, 72, 73
- BN
 - nanotube, 64, 72, 73
 - nanotubes, 73
 - nanotubes
 - ropes, 74
 - polyhedra, 78
- BN nanotube, 103
- BN particles
 - nano-cocoons, 74
- bond polarization theory, 149
- boron, 111
- breaking strength, 20
- Breit–Wigner–Fano plot, 157
- Brillouin zone (BZ)
 - K points, 140
- buckling, 74, 299
- buckling
 - MWNT, 300
 - nanotube, 306
 - SWNT, 299
- bucky paper, 217
- bulk modulus, 19
- bundle, 8
- bundle effect, 159
- bundles, 270
- BZ
 - K -point, 16, 139, 144, 153
- C_{60} , 176, 177, 181, 183, 193
- carbon
 - sp^2 bonds, 273
 - liquid, 13, 24
 - phase diagram, 13, 24
- carbon bonding, 12
 - sp^2 bond, 14
 - π -electrons, 172
 - σ bonds, 172
 - sp^2 bond, 12, 25
 - sp^3 , 12
 - sp^3 bond, 14
 - bond length, 6
 - chemical, 173
 - covalent, 12
 - hybridization, 12, 13, 172
 - hybridization
 - sp^n , 12
- carbon fibers, 11, 12, 18, 19, 33
- carbon fibers
 - bundles, 19
 - composites, 22
 - diameter, 3
 - history, 21
 - mechanical properties, 20
 - mechanical strength, 18
 - melting, 25
 - PAN, 18, 19

- performance, 18
- pitch, 18, 19
- polymer-based, 22
- thermal conductivity, 23
- vapor grown, 2, 12, 18–24
- carbon materials
 - liquid, 12
 - whiskers, 11, 12, 17, 18, 22
 - whiskers
 - mechanical, 22
 - synthesis, 18
- carbon nanofibers, 294
- carbon nanotube
 - parameters, 7
 - production, 72
- catalyst, 150
- catalyst species, 8
- catalytic chemical vapor deposition, 22
- cathode ray lighting element, 289
- cathode ray tube (CRT)
 - thermionic, 290
- cathode stripes, 291
- CdCl_2 structure, 71
- charge transfer, 25, 227
- charge-discharge, 296
- chemical sensor, 307
- chemical vapor deposition (CVD)
 - deposition, 22
- chiral angle, 3–7, 137
- chiral nanotube, 137
- chiral nanotubes, 6
- chiral vector, 4–7
- chiral vector
 - C_h , 137
- chirality, 78, 79, 136
- collapsed tubes, 98
- concentric structure, 165
- conductance
 - intratube, 118
 - junction, 118
 - quantum, 93, 113, 119
 - tube, 94, 99, 114, 119, 120
- conductivity, 194
- configuration
 - sp^2 , 13
- conjugated polymers, 303
- core electrons, 12, 173
- Coulomb blockade, 120, 239, 240
- covalent
 - sp^2 bond, 62
- cross-links, 271, 274
- crossed-tube junctions, 94
- current density, 289
- current-voltage, 107
- dangling bond, 60, 63
- dangling bonds, 14
- DC breakdown voltage, 292
- Debye temperature, 205
- defect
 - pentagon-heptagon pair, 93, 103–108
- defect pair, 104
- density functional
 - local, 97
 - method, 110, 118
- density of rope states
 - electronic, 116, 117
- density of states
 - electron, 183
 - electronic, 107, 115, 125, 175, 177, 181, 183, 185, 186
 - joint, 117
 - local, 111, 113, 114
 - phonon, 199, 201, 204
- density of states (DOS)
 - electronic, 142
- Department of Energy
 - benchmark, 297
- depolarization effect, 143
- diameter
 - d_t , 137
- diameter distribution, 8, 150, 185, 188, 189, 192, 195
- diameter-selective formation, 149
- diamond
 - sp^3 bond, 13
- dielectric function, 153, 174, 178, 179, 188, 191, 193
- dielectric tensor, 174, 178
- dimensionality
 - one to three, 191
- Dirac
 - hamiltonian, 122
 - points, 115
- disorder potential, 123
- dispersion relations, 23
- dope, 154

- dope
 - Br, 154
 - Br₂, 159
 - Cs, 154
- doping
 - alkali metals, 310
 - BC₂N tubes, 79
 - BN tubes, 79
 - carbon materials, 296
 - external, 16, 227
 - functionalization of tubes, 303
 - halogens, 310
 - inorganic tubes, 89
 - intercalated SWNTs, 193
 - intercalation tubes, 310
 - internal, 16, 221
 - interstitial, 16
 - K, 194, 195
 - metallic tubes, 120
 - morphology, 26
 - nanotubes, 171
 - polymers with nanotubes, 304
 - ropes, 116
 - semiconducting tubes, 94, 120, 125
 - substitutional, 16
- Drude resistance, 226, 233, 244
- Drude–Lorentz model, 194
- Drude-like tail, 178

- Edison, 21
- EELS, 173
- elastic properties, 18
- electric polarizability, 99
- electrochemical intercalation, 294
- electromagnetic induction (EMI)
 - shielding, 303
- electron
 - π -electrons, 171, 188
- electron energy loss (EELS)
 - nanotube spectrum, 192
- electron energy loss spectroscopy (EELS), 72, 73, 75, 174, 177, 186, 189, 192, 193, 195, 294
- electron energy loss spectroscopy (EELS)
 - graphite, 177, 178
 - nanotubes, 186
 - theoretical, 186
- electron field emitters, 285
- electron spectroscopies, 171
- electron spin resonance, 254
- electron spin resonance (ESR)
 - technique, 215
 - g -factor, 254
 - g -shift, 254
 - signal, 256
- electronic density of states, 283
- electronic properties, 2, 3, 93, 94, 99, 103
- electronic properties
 - rope, 94
 - SWNTs, 95
 - theoretical, 95
- electronic specific heat, 202
- electronic structure, 14, 62, 96, 97, 103–105, 110, 115, 116, 122, 124, 125, 175, 183, 186
- electronic structure
 - turbostratic graphite, 16
 - E_{pp} , 144
 - carbon fibers, 21
 - graphene, 16
 - SWNT, 94, 95
 - symmetry gap, 96, 107, 117
- electrons
 - π -electrons, 181
- Elliott relation, 255
- emission site density, 289
- emission tips, 286
- energy capacity, 294
- energy contour plot, 139
- energy dispersion
 - graphite, 137, 176
- energy dispersion relations
 - phonon, 146
- energy loss spectrum, 152
- energy storage, 292

- facets, 19, 21, 86, 87
- Fermi level, 25
- Fermi liquid, 224, 247, 251, 253
- field emission, 214, 215, 260–264, 286
- field emission
 - current, 263
 - guns, 260
 - individual nanotubes, 261
 - induced luminescence, 265
- field enhancement factor, 286, 287

- filled nanotubes, 309
- filling nanotubes, 309
- filling nanotubes
 - liquid metals, 222
- flat panel display, 290
- flat-panel screen, 171
- force constants, 14
- Fourier transform infrared (FTIR), 297
- Fowler–Nordheim
 - behavior, 288
 - equation, 260, 286
 - model, 261, 263
 - plot, 287
- fracture, 299
- fuel cells, 292
- fullerene-like caps, 3, 5, 7
- fullerenes
 - discovery, 3, 14
 - isolated pentagon rule, 3, 7
- functionalization, 310
- furnace temperature, 150

- gas discharge tube (GDT)
 - nanotube-based, 292
 - nonlinear shunt, 292
 - protectors, 292
- GaSe nanotubes, 80
- gate voltage, 99
- Gaussian potential, 121
- graphene, 4, 6, 12, 199
- graphite, 61, 64, 72, 75, 77, 79, 174–178, 183, 186, 188, 189, 195, 200, 207
- graphite
 - sp^2 bond, 17, 77
 - arcing, 72
 - crystalline 3D, 12
 - honeycomb lattice, 12
 - kish, 17
 - resistivity, 228
 - single-crystal, 228
- graphite intercalation compound (GIC), 193, 194
- greatest common divisor
 - d_R , 6, 140
- growth, 31
- growth
 - catalytic growth, 44
 - close-ended mechanism, 34
 - lip-lip interaction model, 40
 - open-ended mechanism, 35
 - root growth, 51
 - ropes growth, 50
- helicity, 96, 103, 111, 189
- heterojunctions
 - semiconductor, 103, 105
- hexagons/unit cell
 - N , 139
- HfB₂, 72
- highly ordered pyrolytic graphite (HOPG), 22
- highly oriented pyrolytic graphite, 22
- highly oriented pyrolytic graphite (HOPG), 17
- history
 - carbon fibers, 3
 - carbon nanotubes, 2–4
 - fullerenes, 8
 - nanotubes, 23
- hollow core, 19, 20, 26, 221
- honeycomb lattice, 4–6
- honeycomb lattice
 - unit vectors, 4
 - unit vectors, 5
- HOPG, 15, 17
- hybridization effect, 165
- hydrogen storage, 285, 296, 297

- Iijima, 24
- impurities, 110, 256, 259
- impurities
 - boron, 111, 112, 114
 - magnetic, 260
 - substitutional, 110
- indium-tin-oxide (ITO)
 - stripes, 290
- infrared spectra, 21
- innermost nanotube, 165
- inorganic
 - fullerene, 60, 61
 - nanotube, 60, 61
- inorganic fullerene, 85, 89
- inorganic nanotube, 61, 84, 86, 88
- inter-layer interaction, 163
- intercalated nanotubes, 193
- intercalation, 89, 294
- intercalation
 - bundles of SWNTS, 194

- graphite, 179
- K, 193
- nanotubes, 170
- SWNTS, 194
- SWNTs, 179, 193
- intercalation
 - Li, 69
 - Na, 76
- interface bonding, 301
- interlayer
 - force, 25
 - separation, 15, 16
 - spacing in MWNTs, 219
- interstitial channels, 310
- IPES, 173

- junction
 - metal-metal, 94, 103, 106–108, 119, 124
 - metal-semiconductor, 94, 103–106, 108, 124
 - semiconductor-semiconductor, 119
- junctions, 93, 94, 96, 103–105, 124
- junctions
 - conductance, 119
 - crossed, 119, 120
 - crossed-tube, 117
 - metal-metal, 103, 125
 - metal-semiconductor, 125
 - semiconductor-metal, 104

- kinked nanotube, 108, 110, 114
- kinked nanotube
 - junctions, 124
 - I-V, 108
- Kramers-Kronig analysis, 174, 178

- Landauer formalism, 106
- laser vaporization method, 149
- lattice constant, 15
- light emission, 260
- Lindhardt formula, 188
- linear dispersion, 139
- lip-lip interaction, 74
- lithium battery, 294
- loss function, 174, 178, 179, 186, 192, 193
- Luttinger liquid, 181, 223, 247, 250, 253, 256

- magnetoresistance, 232, 233, 243, 244, 246, 247
- materials properties, 267
- mean free path, 110, 120, 124, 125
- mechanical deformation, 107
- mechanical properties, 103, 266, 268
- mechanical properties
 - disorder effect, 269
- mechanical stress, 107
- mechanical stress
 - axial, 273
 - compressive, 20
 - MWNTs, 267
- metal hydrides, 296
- metallic window, 155
- metallic wires, 221
- microelectrodes, 293
- modulus
 - carbon fibers, 19
- molecular probes, 306
- MoS₂, 60, 82
- MoS₂ inorganic nanotube, 64
- MoS₂ nanotube, 81
- multi-walled carbon nanotubes, 161
- multiwall carbon nanotubes, 3, 8

- nanocomposite, 310
- nanofibers, 20
- nanofibers
 - vapor grown, 23
- nanoswitch, 107
- nanotube
 - chiral angle, 6
 - chirality, 6
 - curvature, 12, 14
 - diameter, 6
 - production, 215–217, 220, 271
 - purification, 215–218, 257–260
 - zigzag, 80, 84
- nanotube hollows, 309
- nanotube indices
 - (n, m), 137
- nanotube tip, 49
- nanotubes
 - excited states, 186
 - intercalated SWNTs, 193
 - metallic, 14
 - semiconducting, 14

- unoccupied states, 186
- Nernstian behavior, 293
- nitrogen, 112
- nuclear magnetic resonance (NMR)
 - proton, 298
- nucleation, 31
- Nyquist noise, 246

- one-dimensionality, 2-4
- onion morphology, 18, 59, 71, 73, 89, 216, 218, 225
- optical, 81
- optical
 - properties, 87
 - device, 84
 - measurements, 61
 - properties, 81
 - transitions, 84
 - tuning, 80, 84
- optical absorption, 151
- optical absorption spectroscopy, 188, 189
- optical density, 155
- organic light emitting diodes (OLED), 304
- over-voltage protection, 292

- pentagon-heptagon
 - 7 pair, 55
- pentagons and heptagons, 72
- perturbations, 121
- perturbations
 - asymmetric, 117
 - external, 93, 120
 - long range, 115, 121, 125
- PES, 176, 177, 181, 183, 185, 186
- phase diagram, 13, 14, 24, 60, 63, 64, 76
- phase shifts, 111-114
- phase velocity, 148
- phonon
 - *K* point, 149
 - dispersion, 85
 - twist mode, 210
 - zone-boundary, 86
- phonon dispersion
 - SWNTs, 203
- phonon dispersion of MWNTs, 203
- phonon dispersion relations, 146
- phonon modes
 - acoustic, 199, 201
 - twist mode, 201
- phonon scattering length, 210
- phonon states, 85
- phonon thermal conductivity, 207
- phonon velocity, 201
- phonons
 - heat capacity, 101
 - twistons, 101
- phonons
 - subbands, 200
 - zone-folding, 200
- photo thermal deflection spectrum, 151, 152
- photo-thermal deflection spectrum (PDS), 152
- photoelectron spectroscopy (PES), 172
- photoemission spectroscopy (PES)
 - angle resolved (ARPES), 175
 - angle resolved inverse (ARIPES), 175
 - data, 181
 - fullerenes, 185
 - graphite, 175
 - nanotubes, 181
- photoemission spectrum
 - graphite, 175
 - MWNTs, 175
- plasma breakdown, 292
- plasmon, 152, 174, 178, 186, 188, 189, 192, 193
- plasmon
 - π -plasmon, 193
 - $\pi+\sigma$ plasmon, 179
 - π -plasmon, 179, 181, 186, 188, 189, 191, 192, 194, 195
 - $\pi + \sigma$, 181
 - $\pi + \sigma$ -plasmon, 186, 189, 192, 195
 - energy, 180
 - free electron, 180
 - MWNT, 192
- plasmon excitation spectrum, 187
- polarizability
 - static, 99, 102
 - tensor, 100
 - unscreened, 100
- polyacrylonitrile, 22
- polyacrylonitrile (PAN)

- fiber, 22
- polyhedra, 60
- polymer composite, 301
- potassium, 193, 195
- PPV, 303
- pseudo-spin, 122
- pseudopotential, 97, 110
- purification, 151

- quantum size effect, 81
- quantum conductance, 106, 231–234, 238, 241, 242
- quantum confinement, 14
- quantum confinement
 - Coulomb blockade, 99
- quantum dots, 120, 123
- quantum size effect, 62, 81, 83
- quantum wire
 - metallic tubes, 99

- radial breathing mode, 21
- radial breathing mode (RBM), 136, 149–151, 153, 156–159, 161–166
- radial breathing mode (RBM)
 - frequency, 150, 164
 - Raman intensity, 155
 - Raman spectra, 162
 - spectra, 155
- radiation dose, 271
- Raman spectra, 85
- Raman intensity
 - $\tilde{I}_{1540}^S(d_0)$, 158
- Raman peak
 - *D*-band, 149
- Raman spectra, 21, 26
- Raman spectra
 - *G*-band, 155
- rehybridization
 - σ - π , 98
- Resonance Raman, 86
- resonance Raman effect, 155
- resonant inelastic x-ray scattering (RIXS)
 - SWNTs, 183, 184
- rhombohedral phase, 15
- RIXS, 173
- rope, 15, 185, 188, 189, 195, 297, 302
- rope
 - (10,10) nanotubes, 115
 - diameter, 270
 - lattice, 193
 - MWNT, 224, 235
 - SWNT, 235, 267, 270, 274, 285, 298, 301
- ropes, 7, 8

- sample preparation, 150
- scanning probe, 67, 77
- scanning probe
 - microscopy, 88
 - tips, 62
- scanning probe microscope tip, 306
- scanning tunneling microscope, 69
- scanning tunneling microscopy (STM), 4
- scanning tunneling spectroscopy, 145
- scanning tunneling spectroscopy (STS), 231
- Schottky
 - barrier, 124
 - barriers, 103, 120
 - behavior, 125
 - diode, 119
- scroll, 17, 18, 219, 220
- selection rule, 142
- Si
 - whiskers, 22
- single-electron tunneling, 239
- SiO₂, 71
- solid lubricant, 87, 88
- solution sample, 150
- space group, 16
- specific heat, 199, 202
- specific heat
 - electronic, 200
 - graphite, 200, 204
 - SWNTs, 204
- specific heat of MWNTs, 206
- spin
 - diffusion length, 256
 - relaxation time
 - Elliott theory, 254
 - susceptibility, 258
 - susceptibility
 - Pauli, 258
- spin susceptibility, 260
- splitting of the DOS peaks, 144
- spray method, 150

- STM, 188
- STM
 - image, 99, 102
- STM tip, 264
- Stokes, 158
- Stone–Wales defect, 110, 113, 114, 284, 299
- Stone–Wales defects, 94
- strain energy, 98
- strength
 - carbon fibers, 19, 22
- strong localization, 240, 241
- STS, 99, 145, 185, 188
- subband, 205
- substrate, 118
- substrate
 - attraction, 118
 - contact force, 125
- surface sensitive, 171
- SWNT
 - diameter, 137
- SWNT films, 289
- sword-in-sheath failure, 19, 20
- symmetry, 5, 100, 107, 124
- symmetry
 - axis, 103
 - breaking, 107
 - broken, 115–117
 - group, 6
 - mirror, 116
 - rotation, 6
 - rotational, 107
 - Stone–Wales, 113
 - symmetry vector, 6
 - vector, 7
- synthesis
 - chemical vapor phase deposition, 8
 - arc method, 8
 - laser vaporization method, 7, 8
- tangential mode, 156
- telecom, 292
- temperature-programmed desorption (TPD)
 - SWNTs, 297
- tensile strength, 19, 298, 299
- thermal conductivity, 210
- thermal conductivity
 - MWNTs, 208
 - SWNTs, 209
 - carbon-based materials, 207
 - graphite, 24
 - pitch fibers, 19
- thermal gravimetric analysis, 309
- three peaks, 152
- threshold fields, 287
- tight binding molecular dynamics, 146
- tight-binding model, 107, 175, 188, 191
- time reversal symmetry, 144
- TiO₂, 60, 71
- tip radius, 262
- topological defects, 94
- transfer energy
 - γ_0 , 176, 188
 - γ_0 , 185
 - γ_0 , 138, 175, 181, 191
- transistor, 171
- translation vector, 4, 7
- translational vector
 - \mathbf{T} , 139
- transmission electron microscope (TEM), 2, 4, 7, 23, 62, 72–74, 82, 83, 87, 216, 219–223, 251, 253, 262, 269, 272–274
- transport
 - nonlinear, 107
 - properties, 113
- transport experiments, 99, 194
- transverse acoustic (TA) modes, 148
- trap states, 122
- tree ring morphology, 18, 21, 23
- triangular lattice, 15
- trigonal warping effect, 144
- triode-type, 290
- turbostratic, 24
- turbostratic
 - nanotubes, 16
- turbostratic graphite, 16
- turbostratic graphite, 16, 219
- twist mode, 203
- twisting acoustic mode (TW), 148
- Umklapp peak, 208
- Umklapp scattering, 207–209, 211
- unit vectors, 137
- universal conductance, 233
- universal conductance fluctuations (UCF), 214, 233, 246

- universal conductance fluctuations (UCF), 240
- V_2O_5 , 60
- vacuum microelectronic devices, 285
- valence orbitals, 12
- van der Waals force, 16, 270
- van der Waals interaction, 176
- van der Waals spaces, 294
- van Hove singularities, 142, 231, 232, 248, 249
- van Hove singularity, 112, 176, 183, 185, 186, 188, 189, 192, 193, 195
- weak localization, 214, 232, 233, 244–247, 253
- weak localization
 - logarithmic dependence, 234
 - low- T conductance, 235
 - magnetoresistance, 244
 - WL theory (2D), 233
- whiskers
 - carbon, 22
 - graphite, 12, 17, 18, 227
 - iron, 22
 - nonmetals, 22
- WKB approximation, 260
- work function, 287
- WS_2 , 80
- WS_2
 - nanotubes, 62
- WS_2 nanotube, 81
- x-ray absorption spectroscopy (XAS), 172, 174
- x-ray absorption spectroscopy (XAS)
 - SWNTs, 186
- x-ray electron spectroscopy (XES), 183
- x-ray emission spectroscopy (XES)
 - graphite, 177
- XES, 173
- Young's modulus, 20, 62, 87, 103, 268, 269, 273, 298
- Young's modulus
 - MWNTs, 268
- zero gap semiconductor, 16
- zigzag nanotubes, 4–6, 137
- zone folding, 23
- zone-folding, 210
- ZrO_2 , 71